NASA Contractor Report 159375

DEFORMATION CHARACTERISTICS AND FAILURE MODES OF NOTCHED GRAPHITE POLYIMIDE COMPOSITES AT ROOM AND ELEVATED TEMPERATURES

Jonathan Awerbuch, Harry E. Perkinson,
and Ihab L. Kamel

DREXEL UNIVERSITY
Philadelphia, Pennsylvania 19104

NASA Grant NSG-1606
August 1980

NASA
National Aeronautics and
Space Administration

Langley Research Center
Hampton, Virginia 23665

DEFORMATION CHARACTERISTICS AND FAILURE MODES OF NOTCHED GRAPHITE POLYIMIDE COMPOSITES AT ROOM AND ELEVATED TEMPERATURES

PROGRESS REPORT

NASA GRANT No. NSG 1606

PERIOD JUNE 1, 1979 - August 31, 1980

Jonathan Awerbuch,
Harry E. Perkinson,
Ihab L. Kamel

Drexel University
Philadelphia, Pennsylvania 19104

FOREWORD

This document is a progress report on research into the fracture behavior of graphite/polyimide laminates at room and elevated temperatures under NASA Grant No. NSG 1606. The work was conducted from June 1, 1979 to August 31, 1980. Clarence C. Poe of Langley Research Center, Hampton, Virginia was the NASA technical monitor for the grant.

A Drexel University support group participated in the program: J. Steinman and A. Seneca as technical assistants; undergraduate students G. Kushnir, H. Rostami and W. Clark in specimen preparation and data reduction; D. Weber in illustration graphics; and J. Trachtman in manuscript preparation.

The experimental program itself was conducted by Mr. Harry E. Perkinson, graduate student in the Department of Mechanical Engineering and Mechanics, and the microstructural studies were performed by Dr. Ihab L. Kamel, Department of Materials Engineering. The principal investigator was Dr. Jonathan Awerbuch, Department of Mechanical Engineering and Mechanics.

SUMMARY

This progress report describes the results of research work on the characterization of fracture behavior in graphite/polyimide (Gr/PI) Celion 6000/PMR-15 composites during the period June 1, 1979 to August 31, 1980. Emphasis has been placed on the correlation between the observed failure modes and the deformation characteristics of center-notched Gr/PI laminates, where particular attention has been given to the proper test procedure and analytical approach employed.

The purpose of this work is not merely to generate and furnish quantitative data but also to discuss the appropriate methodology to be employed in characterizing a new composite material system. The investigation focused on the deformation characteristics, crack tip damage growth, fracture strength and notch sensitivity and the associated characterization methods. Special attention has also been given to nondestructive evaluation of internal damage and damage growth, techniques such as acoustic emission, X-ray radiography, and ultrasonic C-scan. Microstructural studies using scanning electron microscopy, photomicrography, and the pulsed nuclear magnetic resonance technique were employed as well.

A description of all experimental procedures and techniques is given, e.g. mechanical and nondestructive testing, and a summary of representative results is given for four Gr/PI laminates: $[0/+45/90/-45]_{2s}$, $[\pm 45]_{2s}$, $[0]_8$, and $[90]_8$. The report includes a comparison between the experimental results and several of the existing basic analytical approaches, a correlation between the various testing techniques, together with an assessment of the effect of the experimental technique on the characterization of failure.

TABLE OF CONTENTS

		Page
SUMMARY		
I.	INTRODUCTION	1
	A. General	1
	B. Mechanical Behavior	2
	C. Objectives	3
II.	EXPERIMENTAL PROCEDURE	5
	A. Introduction	5
	B. Materials	5
	C. Laser Interferometric Displacement Gage (IDG)	7
	D. Compliance Gage	10
	E. Strain Gage	11
	F. Ultrasonic C-Scan	12
	G. X-ray Radiography	14
	H. Failure Modes	14
	I. Nuclear Magnetic Resonance (NMR) Studies	15
	J. Acoustic Emission	15
	K. Equipment Used	15
III.	ACOUSTIC EMISSION INSTRUMENTATION	17
	A. Introduction	17
	B. Instrumentation Capabilities	18
	C. Instrumentation	20
IV.	RESULTS AND ANALYSES	21
	A. Mechanical Properties	21
	B. Load-Crack Opening Displacement Curves	21
	C. Compliance Curves	23
	D. Elevated Temperature Load-COD Curves	28
	E. Fracture Strength	28
	F. Notch Sensitivity	33
	G. Axial Splitting	33
	H. Acoustic Emission (AE)	35
	I. Failure Modes and Fracture Surfaces	44
	J. Ultrasonic C-Scan	46

Page

K. Elevated Temperature Tests 47

L. Pulsed Nuclear Magnetic Resonance (NMR) Measurements. . 48

V. RESULTS AND CONCLUSIONS 50

VI. RECOMMENDATIONS 54

REFERENCES 56

ILLUSTRATIONS (1-57)

LIST OF ILLUSTRATIONS

1. A general view of the testing facilities.

2. Photomicrograph of two indentations located at the center of the crack.

3. Schematic view of the laser interferometry displacement technique. Nominal value of d is 0.5 mm and α_o is typically 42°.

4. A schematic view of data reduction from the IDG records.

5. a. Block diagram of the Dunegan/Endevco 3000 acoustic emission system.

   b. Schematics of location and amplitude distribution histograms and accumulative counts and events diagrams [920A Manual].

   c. Schematics of pulse width distribution histograms, count rate and Cumulative Event Amplitude Distribution (CEAD) diagrams [920A Manual].

6. Stress-strain curves for all four graphite/polyimide laminates.

7. Far-field load-displacement curves for Gr/PI $[0/+45/90/-45]_{2s}$ laminate for various crack lengths obtained with the compliance gage.

8. Load-COD curves for Gr/PI $[0/+45/90/-45]_{2s}$ laminate for various crack lengths obtained with the IDG.

9. Schematics of transverse strain records at the crack edges.

10. Example of three load-COD curves at initial loading for Gr/PI $[0/+45/90/-45]_{2s}$ laminate.

11. Global compliance vs. crack length for Gr/PI $[0/+45/90/-45]_{2s}$ laminate.

12. Local compliance vs. crack length for Gr/PI $[0/+45/90/-45]_{2s}$ laminate.

13. Comparison of experimental K-calibration factors with theoretical isotropic curve for Gr/PI $[0/+45/90/-45]_{2s}$ laminate.

14. Load-COD curves for Gr/PI $[0/+45/90/-45]_{2s}$ laminate at 70°F and at 450°F, obtained with the IDG.

15. Comparison of initial load-COD curves for Gr/PI $[0/+45/90/-45]_{2s}$ laminate at 70°F and at 450°F, obtained with the IDG.

16. Least squares fit for c_o for Gr/PI $[0/+45/90/-45]_{2s}$ and Gr/Ep $[0/90/+45/-45]_{2s}$ laminates.

17. Comparison of analytical (WEK model) and experimental results for notched strength for Gr/PI $[0/+45/90/-45]_{2s}$ laminate.

18. Comparison of notch sensitivity between Gr/PI $[0/+45/90/-45]_{2s}$ and Gr/Ep $[0/90/+45/-45]_{2s}$ laminates.

19. Notched strength versus crack length: comparison of ML model with experimental data for Gr/PI $[0/+45/90/-45]_{2s}$ laminate.

20. Notched strength versus crack length: comparison of WEK model with experimental data on logarithmic scale for Gr/PI $[0/+45/90/-45]_{2s}$ laminate.

21. Experimental results on length of axial splitting versus applied load for three notched Gr/PI $[0]_8$ specimens.

22. Load-COD curves for notched Gr/PI $[0]_8$ specimen obtained with the IDG (crack length = 15.37 mm).

23. Radiographs of the axial splitting of notched Gr/PI $[0]_8$ specimen (crack length = 15.37 mm) together with an ultrasonic C-scan after failure.

24. Location distribution histograms of Gr/PI $[0/+45/90/-45]_{2s}$ laminate at various load levels (with spatial discrimination).

25. Amplitude distribution histograms for Gr/PI $[0/+45/90/-45]_{2s}$ laminate at various load levels (with spatial discrimination).

26. Amplitude distribution histogram and Cumulative Event Amplitude Distribution for Gr/PI $[0/+45/90/-45]_{2s}$ laminate (with spatial discrimination).

27. Amplitude distribution histograms (in linear and logarithmic scales) and Cumulative Event Amplitude Distribution for Gr/PI $[0/+45/90/-45]_{2s}$ laminate.

28. Cumulative Event Amplitude Distribution for Gr/PI $[0/+45/90/-45]_{2s}$ laminate at various load levels.

29. Location distribution histogram (in linear and logarithmic scales) for notched Gr/PI $[0/+45/90/-45]_{2s}$ laminate (crack length = 15.54 mm).

30. Amplitude distribution histogram (in linear and logarithmic scales) and Cumulative Event Amplitude Distribution for notched Gr/PI $[0/+45/90/-45]_{2s}$ laminate (crack length = 2.10 mm).

31. Cumulative Event Amplitude Distribution for notched Gr/PI $[0/+45/90/-45]_{2s}$ laminate at various load levels (crack length = 20.5 mm).

32. Location distribution histogram for notched Gr/PI $[0/+45/90/-45]_{2s}$ laminate at 450°F (crack length = 15.38 mm).

33. Amplitude distribution histogram for notched Gr/PI $[0/+45/90/-45]_{2s}$ laminate at 450°F (crack length = 15.38 mm).

34. Amplitude distribution histogram Cumulative Event Amplitude Distribution for notched Gr/PI $[0/+45/90/-45]_{2s}$ laminate (crack length = 15.54 mm).

35. Location distribution histogram for edge notched Gr/PI $[90]_8$ specimen (crack length = 0.025 mm).

36. Amplitude distribution histogram for edge notched Gr/PI $[90]_8$ specimen (crack length = 0.025 mm).

37. Location distribution histogram (in linear and logarithmic scales) for Gr/PI $[\pm 45]_{2s}$ laminate together with the specimen's radiograph.

38. Amplitude distribution histogram (in linear and logarithmic scales) and Cumulative Event Amplitude Distribution for Gr/PI $[\pm 45]_{2s}$ laminate.

39. Location distribution histogram (in linear and logarithmic scales) for notched Gr/PI $[0]_8$ specimen (crack length = 5.08 mm) after loading to 20.2 KN (4500 lb).

40. Location distribution histogram (in linear and logarithmic scales) for notched Gr/PI $[0]_8$ specimen (crack length = 5.08 mm) after failure (53.91 KN, 12120 lb).

41. Amplitude distribution histogram (in linear and logarithmic scales) and Cumulative Event Amplitude Distribution for notched Gr/PI $[0]_8$ specimen (crack length = 5.08 mm) after loading to 33.36 KN (7500 lb).

42. Location distribution histogram (in linear and logarithmic scales) for Gr/PI $[0]_8$ specimen.

43. Amplitude distribution histogram (in linear and logarithmic scales) and Cumulative Event Amplitude Distribution for Gr/PI $[0]_8$ specimen.

44. Accumulative counts and events as a function of load during loading/unloading cycles for Gr/PI $[0/+45/90/-45]_{2s}$ laminate.

45. Amplitude distribution histogram (in logarithmic scale) and Cumulative Event Amplitude Distribution at two different load cycles.

46. Count rate as a function of load during loading/unloading cycles for Gr/PI $[0/+45/90/-45]_{2s}$ laminate.

47. The Felicity ratio as a function of percent of ultimate load for various Gr/PI $[0/+45/90/-45]_{2s}$ specimens.

48. Photomicrographs of Gr/PI $[0/+45/90/-45]_{2s}$ laminate.

49. Photomicrographs of Gr/PI $[\pm 45]_{2s}$ laminate.

50. Photomicrographs of Gr/PI $[0]_8$ specimen.

51. SEM photographs of Gr/PI $[0/+45/90/-45]_{2s}$ laminate.

52. SEM photographs of notched Gr/PI $[0/+45/90/-45]_{2s}$ laminate (crack length = 20.47 mm).

53. SEM photographs of edged notched Gr/PI $[90]_8$ specimen (crack length - 0.025 mm).

54. SEM photographs of the split area (at the crack tip) for notched Gr/PI $[0]_8$ specimen (crack length = 15.37 mm).

55. Ultrasonic C-scan results for "poor" and "good" Gr/PI $[\pm 45]_{2s}$ laminate together with a radiograph of the "poor" specimen.

56. Signal relaxation spectrum following a 90° pulse.

57. Signal relaxation spectrum following a 90° pulse for unfilled Polyimide at different temperatures.

LIST OF TABLES

Table		Page
I	List of Number of Specimens	6
II	Mechanical Properties	22
III	Experimental Values of Local (C_ℓ) and Global (C_g) Compliances for Graphite/Polyimide $[0/+45/90/-45]_{2s}$	27
IV	Notched Strength Data for Graphite/Polyimide $[0/+45/90/-45]_{2s}$	29
V	Notch Sensitivity	32

I. INTRODUCTION

A. General - In the research activity and application studies on resin matrix composites, most of the attention has been devoted to epoxy resin materials. Among the variety of polymer matrix materials, graphite/epoxy and boron/epoxy are most widely used in aeronautical, aerospace and industrial applications. In fact, considerable hardware is already in use. However, the epoxy resins are limited to applications up to 175°C (347°F) due to their relatively low thermal-stability. There is a growing need to develop light weight composite materials which will perform at higher temperatures. Graphite/polyimide (Gr/PI) is a candidate material for aerospace applications because of its good mechanical properties and its thermo-oxidative stability at elevated temperatures up to 315°C (600°F). These qualities have already been demonstrated in many studies within the required temperature range, e.g. [1-9].

The aircraft industry and NASA Langley Research Center are heavily involved in studying the applicability of various Gr/PI Composites for Advanced Space Transportation Systems, known as the CASTS program, which is now focusing on a Gr/PI "aft body flap" for the Space Shuttle orbiter vehicle. Other applications in missiles, jet engine parts, structures for an advanced fighter and for supersonic transport are also under consideration by NASA LaRC (CASTS program), NASA LeRC (SCR Program) and AFML, all of which support both in-house programs and research activities in the various aerospace industries and universities. Details of the various programs are given in Ref. [10].

B. Mechanical Behavior - Most of the research on polyimides has been performed at NASA Langley and NASA Lewis Research Centers [1-5, 7, 11-14] where the most promising polyimide resins (PMR-15 and LARC-160) have also been developed. Other types of polyimides such as P13N, P10P and NR-150 have also been investigated. A detailed description of the chemical structures of the various polyimides can be found, for example, in [1-5, 12-16).

The research activity has focused on assessing and characterizing the processing difficulties and in developing a technology to improve (and reduce cost) of the processing and fabrication of Gr/PI composite materials. A study on the effect of the processing parameters (staging, cure-pressure and heating rate) on the thermomechanical properties of Gr/PI composites is given in [11, 14, 17] for graphite and glass fibers in PMR-15 polyimide resin. Compared with other polyimide resins, PMR-15 was found to be more stable at ambient conditions and to offer excellent shelf life and excellent thermomechanical stability characteristics [1, 2]. Test results such as those of interlaminar shear strength, flexural strength and modulus as well as the effect of isothermal aging on composite weight loss show that the in-situ Polymerization of Monomer Reactant (PMR) approach is a powerful method for fabricating high performance polymer matrix composites [1, 3, 6, 17]. With some modification of the PMR-15, improved tack and drape retention characteristics could be achieved at a temperature range up to 600°F for a time duration up to 1600 hours [3]. A detailed study on the effect of thermal conditioning on the failure mechanisms in five different Gr/PI systems has been discussed in [6].

Another detailed study on the mechanical behavior of two other Gr/PI systems, Modmore I/WRD 9371 and boron/P13N, is given in [18]. This study elaborates on a variety of properties such as tensile, compressive and interlaminar shear properties and thermal and tensile load cycling, to name only a few, for unidirectional and $[0_2/\pm45]_s$ laminates.

A different polyimide system, LARC-160 and a modified version, LARC-160A3, has been developed at NASA Langley Research Center [5, 7]. The pre-pegging and laminate preparation are explained and the results of short beam shear strength and flexural strength data are given. It is shown that the modified version has better retention of mechanical properties at room and elevated temperatures after being aged for 125-500 hours at 550°F-600°F. The LARC-160A3 based composites are more thermo-oxidately stable than those made of LARC-160 [7].

C. Objectives - The bulk of research on Gr/PI composites has explored its thermo-oxidative stability, interlaminar shear strength, and flexural strength and modulus. Very little research on the fracture behavior of Gr/PI laminates has been conducted, either at room or elevated temperatures, and very limited data exists at the present time.

The objective of the current research work has been to conduct a detailed and comprehensive study on the fracture behavior of Gr/PI laminates at room and elevated temperatures with emphasis on the deformation behavior, load-time flaw growth, and the associated characterization methods. Special attention is also being given to nondestructive evaluation of damage growth, through acoustic emission, X-ray radiography, ultrasonic C-scan techniques, and microstructural studies using scanning electron microscope (SEM), photomicrography and pulse nuclear magnetic resonance (NMR) techniques.

The effect of elevated temperatures on damage progression, notch sensitivity, and deformation characteristics is being investigated through a variety of experimental techniques and the results are being compared with their associated analyses.

In this study, four laminates of Gr/PI Celion 6000/PMR-15 are being investigated: $[0/+45/90/-45]_{2s}$, $[\pm 45]_{2s}$, $[0]_8$, and $[90]_8$. Some of the experimental results obtained to date are presented here and are correlated with a

number of existing analytical approaches. The experimental techniques employed are fully described and a discussion of the results obtained is presented. Accordingly, the rationale for continuing and completing the current study will be self-explanatory.

II. EXPERIMENTAL PROCEDURE

A. Introduction - The experimental procedure employed in this program included a variety of techniques from which the material mecahnical properties, fracture behavior, deformation characteristics, and failure modes were examined. These techniques include: a laser interferometry displacement gage for obtaining local load-crack opening displacement (COD) curves at room and elevated temperatures from which local compliance curves and the K-calibration factor are obtained; a standard compliance gage for obtaining far-field load-displacement curves together with global compliance curves; and standard strain-gages for characterizing the material elastic properties at room and elevated temperatures. In addition, a variety of nondestructive inspection techniques were employed, such as ultrasonic C-scan, acoustic emission, and X-ray radiography for characterizing the internal damage prior to, during, and after failure of the composite laminates. Post-failure examination of the fracture surfaces was carried out as well using Scanning Electron Microscopy and photomicrographs, and pulsed Nuclear Magnetic Resonance (NMR) technique was used for microstructural studies.

All mechanical testing was performed on a closed-loop servo hydraulic Instron testing machine (Model 1331) at a displacement rate of 0.127 mm/min (0.005 inch/min).

Implementation of these techniques required the purchasing of a wide range of instrumentation, the details of which are given at the end of this Section. A general view of part of our testing facility is shown in Figure 1.

B. Materials - The material tested in this program is Gr/PI Celion 6000/PMR-15, prepared by NASA Langley Research Center. Two types of specimens were used: center-notched specimens with dimensions of 305 mm (12 inch) long x 51 mm (2.0 inch) wide; and unnotched specimens, from which basic mechanical properties

TABLE I: LIST OF NO. OF SPECIMENS

Material	Unnotched	Crack-Length (2a/w)							Total No. of Specimens
		0.01	0.05	0.10	0.20	0.30	0.40	0.50	
$[0/+45/90/-45]_{2s}^{(a)}$	24	18	19	19	19	21	17	17	154
$[\pm 45]_{2s}^{(b)}$	29	1	1	1	1	1	1	1	36
$[\pm 45]_{2s}^{(c)}$	29	1	1	1	1	1	1	1	36
$[0°]_{8}^{(b)}$	61	11	-	12	-	11	-	-	95
$[90°]_{8}^{(b)}$	39	8	-	-	12	-	-	-	59
								Total	380

(a) For $[0/+45/90/-45]_{2s}$ a minimum of 3 specimens per crack length for each of the six temperatures is available.

(b) A limited number of specimens for basic material study.

(c) Poor laminate (fabrication inhomogeneities and warpage).

are obtained, with dimensions of 305 mm (12 inch) long x 25.4 mm (1.0 inch) wide. Center notches of about 0.51, 2.54, 5.08, 10.16, 15.24, 20.32 and 25.4 mm (0.02, 0.10, 0.2, 0.4, 0.6, 0.8 and 1.0 inch, respectively) long and 0.38 mm (0.015 inch) wide were introduced by ultrasonic technique. All specimens were cut, and notches introduced, at NASA LaRC Laboratory from plate sizes of 1270 x 660 mm (50 x 26 inch) or 610 x 610 mm (24 x 24 inch). The type of laminates and number of specimens per crack size is given in Table I.

In order to obtain maximum information and reliable data, the experimental program calls for one to three tests (data points) per crack length at each temperature and for each laminate by the end of the program. The exact number of tests is to be decided during the work when the reproducibility of the data is verified. The exact number of temperatures used in the testing program is to be determined according to the actual test results and the degree to which the temperatures effect the variables tested.

Each of the 380 specimens has been carefully measured at three locations along the length to ensure a minimum acceptable uniformity in specimen dimensions. The location of each specimen on the plate has also been recorded so that designation of specimens according to crack size and test temperature could be made randomly to ensure reliable test results.

The specimens were tested without using the standard end tabs. Instead, a piece of 0.1 mm (0.004 inch) thick plastic sheet was attached to the specimen surface on both sides of the specimen ends, backed by a 400 grit sanding paper. For all practical purposes this procedure successfully eliminated grip slippage.

C. Laser Interferometric Displacement Gage (IDG) - The laser interferometric technique has been successfully employed to measure the crack-opening-displacement (COD) of the center-notched unidirectional metal matrix composite [19]. This technique enables measuring the COD very close to the

crack surfaces (gage length of 500 μm) and was found to be highly sensitive in detecting crack tip damage, very accurate in the submicron scale, and simple to utilize. Moreover, this technique can be used in a large range of environmental temperatures [20]. Since a major effort in the experimental program involved utilizing the IDG for COD measurement, and since this technique has not been employed in fracture studies of composite materials, a detailed description of this technique is presented here.

The crack opening displacement (COD) is measured by means of laser interferometry technique which enables measuring displacement over a very short gage length. When a coherent monochromatic light from a laser source impinges upon two closely adjacent, reflecting indentations on the sample, it is reflected (diffracted) back at an angle α_o with respect to the incident beam. The diffracted beams overlap, generating interference fringe patterns on either side of the incident laser beam. As the distance (d) between the indentations changes, due to the applied load, the two fringe patterns move. As this movement is observed from a fixed position, at an angle α_o, it can be related to the change in distance (δd) between the indentations.

The equation locating the bright interference fringes is [21]

$$d \sin \alpha_o = m\lambda \qquad (1)$$

where m is the fringe order (m = 0, ±1, ±2, ±3 ...), λ is the wave length of the laser beam, d is the spacing between indentations and α_o is the angle between the incident and reflected beams.

The change in distance between indentations, i.e. the displacement δd, is related to the change in fringe order, δm, at the fixed observation point by:

$$\delta d = \frac{\lambda \delta m}{\sin \alpha_o} \qquad (2)$$

where δm is the number of fringes (or fraction of fringes) passing the fixed observation position.

Using a laser beam wavelength (λ) of 0.6328 μm (He-Ne laser) and $\alpha_o = 45°$ the calibration constant $\lambda/\sin \alpha_o$ in Equation (2) is approximately 0.95μm. Thus, a fringe motion of $\delta m = 1$ corresponds to a displacement of about one micron. Since a shift of one half fringe movement is easily detectable, a resolution of the measurement easily reduces to a submicron scale. The displacement range in this technique is limited and depends on the spacing between indentations, dimensions of the indentations, and the power of the recording system. However, a displacement range of up to 300 μm is easily obtained in our experiments.

In order to obtain clear fringe patterns, the specimens should have a fairly flat, smooth and reflective surface. Therefore, small, well-polished aluminum tabs, 1.0 x 1.0 mm (0.04 x 0.04 inch) and 0.0127 mm (0.005 inch) thick were bonded to the specimen on both sides of the crack surface at its center. Preparation of the specimen surface is similar to that for strain-gage bonding (see Micro-Measurement Instruction Bulletin B-129). M-BOND 610 is used, following the procedure described in Micro-Measurement Instruction Bulletin B-130-6. The glue is cured for two hours at 325°F. Shallow reflective indentations, of a pyramidal shape, are applied to the surface of the aluminum tabs with a Lietz microhardness tester. The dimensions of the indentations are approximately 50 x 50 μm. The original distance between the two indentations is about 500 μm, with edges normal and parallel to the crack surfaces, as shown in Figure 2.

The instrumentation system for measuring the crack opening displacement is simple and economical and consists of a Spectra Physics Model 120, 15 mW He-Ne laser, two photoresistor detectors, two signal amplifiers with d-c voltage output, and a three-channel stripchart recorder, as shown schematically in Figure 3. The sensing elements were two CdS bulk effect photoresistors. The active face of each of them was masked, leaving 0.1 mm slit which was

narrower than the fringe spacing so that the photoresistors responded to well defined maximum and minimum values of intensity. The output signals of the photoresistors were recorded on a stripchart recorder through a d-c amplifier. This recording technique is essentially similar to the one described in Reference [22]. A comprehensive description of the laser interferometric technique is given in Reference[23].

Figure 4 shows a typical intensity plot obtained on the stripchart recorder as the fringe patterns pass by the two stationary photoresistors. This particular plot (Figure 4) is for a boron/aluminum specimen having a 12.85 mm (0.5 inch) long crack. The data reduction of these signals is fairly easy, although very time consuming. Correlating the time at which various maxima and minima occur (δm = 0, 1/2, 1, 1 1/2...) with the load-time plot obtained from the Instron chart recorder output yields the required load-COD curve, Figure 4. Fringe motion occurs with any rigid body motion of the sample. However, rigid body motion can be eliminated by averaging the displacement obtained from the upper and lower (Figure 3) photoresistors [23].

It should be noted that the IDG technique has been successfully employed for metal matrix composites [19,24,25,26] as well as for resin matrix composites [27].

D. Compliance Gage - A standard Compliance Gage of 25.4 mm (1.0 inch) gage length was used to test for the basic material properties of the unnotched specimens and to obtain the far-field load-displacement curves for the center-notched laminates. For the latter, the compliance gage was positioned so that the crack was at the center of the gage section. The far-field load-displacement curves and their resulting global compliance curves are compared with the load-COD curves obtained by means of the IDG technique and with its resulting local compliance curves.

E. Strain Gage - Selected specimens were strain-gaged for room and elevated temperature testing. Since all strain gages, strain gage instrumentation and tools were purchased from Micro-Measurements (M.M.), the techniques used in bonding the strain gages follows M.M. Instruction Bulletins (I.B.).

1. Room Temperature Strain Gages: Surface preparation followed the procedures described in I.B. B-129. The bond system used was M-Bond 200 (Eastman 910) and was applied according to I.B. B-127-5. Three types of strain gage systems were applied:

a. For axial measurements: M.M. EA-06-250BF-350 (gage length = 6.35 mm, grid width = 3.18 mm).

b. For Poisson's ratio measurements: a 90° rosette composed of two separate gages, M.M. CEA-06-125UT-350 (gage length = 3.18 mm, grid width = 4.19 mm).

c. In-plane shear modulus measurements: two types of 90° rosettes were applied on $[\pm 45]_{2s}$ Gr/PI laminate following Rosen [28] procedure for measuring in-plane shear modulus:

1) a 90° rosette type M.M. EA-06-125TB-350 (gage length = 3.18 mm, grid width = 3.81 mm). This rosette has a common electrical connection between the gages, resulting in a direct measurement of $(\varepsilon_x - \varepsilon_y)$ in the recording system.

2) Same 90° rosette that was used for the Poisson's ratio as described above. It should be noted that both techniques have resulted in very similar results for the in-plane shear modulus.

The bridge amplifier system used was a six-channel Vishay Instruments 2100 System. Bridge excitation voltage was set at one volt to minimize

zero drift due to heat build-up on the gage grid. All strain readings were corrected for errors due to transverse deformation of the strain gage according to the M.M. Technical Note TN-137.

2. Crack Propagation Gage: For notched unidirectional Gr/PI, crack propogation gages were used to measure the initiation of axial splitting of the matrix. Two M.M. TK-09-CPB02-005 gages were employed at both crack tips at a distance of 0.76 mm (0.03 inch) from the crack surface. This gage includes ten grid lines with a spacing of 0.254 mm (0.01 inch). The circuitry used for the crack propogation gage is described in M.M. PB-110-2.

3. Elevated Temperature Strain Gages: For elevated temperature strain-gaging, the specimen surfaces were prepared according to the M.M./I.B. B-129, after which the specimens were air dried at 220°F for approximately 24 hours. The M.M. M-BOND 610 was used and applied according to M.M./I.B. B-130-6. The glue was cured at 350°F for one hour, making sure that the heating rate did not exceed 20°F/min. Silver solder was applied as described in M.M. TN-129. This procedure requires special care and experience to avoid breaking the strain-gage leads. For the elevated temperature axial gage, type M.M. WK-06-250BG-350 (gage length = 6.35 mm, grid width = 3.18 mm) series was used. The strain gage circuitry includes a dummy specimen to compensate for thermal strains (two-arm bridge) and signals were conditioned by the Vishay 2100 Model Signal Conditioner.

F. Ultrasonic C-Scan - The quality of composite laminates depends strongly upon proper choice of fabrication procedure and parameters of the curing cycles. The Graphite/Polyimide systems, which are relatively new compared to the epoxy matrix composites, require more care and a higher level of expertise. The quality of the plates must still be examined for fabrication inhomogeneities such as local delamination, poor bonding and warpage. Therefore, each of the

380 specimens has been inspected ultrasonically by C-scan testing and the poor specimens have been screened and marked. Due to the sensitivity of C-scan results to the operating procedures and parameters, each specimen has been C-scanned several times, varying the detecting parameters (such as gain and time delay) to ensure confidence in the results. The C-scan testing is performed as follows:

All Gr/PI specimens were C-scanned using a reflector plate method. A 15 MHz transducer with a 25.4 mm focal length was focused below the top surface of a glass plate approximately 9.5 mm (0.37 inch) thick. The C-scan system was set to scan at moderate speeds across the specimen and to scan at 0.0254 and 0.254 mm increments. The system was calibrated using standard NASA LaRC Gr/PI testing plates 12-D and 13-D into which an artificial square insert was implanted for calibration purposes. An excellent agreement between NASA LaRC results and our Composite Laboratory results was established, provided that the gain used in our laboratory ranged between 30 dB - 34 dB as opposed to a 30 dB gain used by NASA LaRC.

The $[0/+45/90/-45]_{2s}$ laminate plates were C-scanned by the NASA LaRC technical staff before being machined and shipped to our laboratory. The gain used by NASA LaRC was 25 dB. We inspected each specimen in great detail as well, using a gain of approximately 28 dB. Again, a good agreement between measurements was established. The $[0]_8$, $[90]_8$, and $[\pm 45]_{2s}$ plates, being thinner than the $[0/+45/90/-45]_{2s}$ plates, were scanned at gain levels between 24 dB - 28 dB. It should be noted that all unnotched specimens were scanned along their entire gage length, while the notched specimens were scanned only in the vicinity of the notch (51 mm on either side of the notch).

As mentioned above, each specimen was scanned several times, varying the detecting parameters. This was unavoidable since it was found that the C-scan results are very sensitive to a number of conditions such as water height and

temperature, focal distance from the reflecting plate, the slant of the plate, and operator errors, all of which may alter the final results, even when instrument settings are held constant.

The equipment in use was:

1. KB-Aerotech transducer Model Alpha 15 MHz/0.375 (1.0 inch focus)

2. Å Laboratory Scanner Model US 450

3. Sperry Reflectoscope Type UM771-50R078 used in conjunction with Krautkramer Model USIP11.

G. X-ray Radiography - This nondestructive test technique has been employed for three major purposes: 1) to monitor crack tip damage growth, 2) to compare C-scan results with X-ray radiography, and 3) to attempt a correlation between monitoring damage growth through acoustic emission and X-ray radiography.

A Hewlett-Packard Faxitron model 43804N X-ray cabinet with a 3mA continuous current and beryllium window (0.63 mm thick), was used with a focal distance of 6.45 mm. The specimens were X-rayed at 20 KV. The $[0/+45/90/-45]_{2s}$ laminates were exposed for 9 seconds, while the $[0]_8$, $[90]_8$, and $[\pm 45]_{2s}$ were exposed for 7 seconds. The penetrant used was 1,4 - Di-iodobutane (D.I.B.) which was either applied under load or after removal of load, depending upon the objective of the test. All photographs used Polaroid Type 57 film.

H. Failure Modes - In addition to the procedures described above for monitoring damage, the fracture surfaces were examined after failure using Scanning Electron Microscope (SEM). In order to obtain a better view of the fracture surfaces and so better understand the different modes of failure, a successful attempt has been made to obtain stereo (three-dimensional) views of the fracture surface.

Photomicrographs were prepared as well to monitor internal damage at various locations along the specimens both before and after failure.

I. Nuclear Magnetic Resonance (NMR) Studies - Attempts were made to examine the molecular mobility and bonding in the fiber-free and reinforced Gr/PI laminates. These were accomplished by looking at the delay of proton spin alignment in a strong magnetic field. The time required for the protons to reorient to the original magnetic field after a 90° pulse can be correlated to the interatomic bonding. For the composite samples, the proton spin-spin relaxation times (T_2) were measured using a Spin-Lock CPS-2 coherent pulsed NMR spectrometer operating at a frequency of 40 MHz. The measurements covered the temperature range of 300°F - 400°F. The T_2 delays were determined directly from the free induction delay of a single pulse, for the matrix and four laminates, because the delay time (T_2) was less than 100 μ sec.

J. Acoustic Emission - A Dunegan/Endevco 3000 series acoustic emission monitor was used to monitor damage initiation and propagation in all four Gr/PI laminates. Acoustic emission has been monitored for each specimen tested and the results are described in Section IV. The data recorded include accumulative events and counts, count-rate as a function of load, line-location of events, and amplitude distribution histograms of events occurring within a pre-set area of interest along the specimens as well as the cumulative events amplitude distributions. All these data were recorded on an X-Y recorder.

A major effort of this research program was to monitor damage initiation and progression through acoustic emission for the different Gr/PI laminates at room and elevated temperatures, notched and unnotched specimens. Because of the importance of this part of the overall program, a more detailed description of the significance of monitoring acoustic emission and the instrumentation used is given in Section III.

K. Equipment Used - As described above, the experimental program of this research work entailed the use of a variety of equipment and instrumentation.

The following is a list of all equipment purchased for and/or built in our Composites Laboratory during this program period and which has been used in this research activity.

1. Spectra Physics Model 120 Helium Neon Laser Unit 15 mW
2. Soltec Model 330 3-Pen Strip Chart Recorder
3. Photocell amplifier*
4. Laser unit bench*
5. IDG oven*
6. Omega Digital Thermometer Model 2166A (Ten thermocouples)
7. Omega Dual Set-Point Temperature Controller Model 4002
8. Vishay Instruments Strain Gage Conditioner and Amplifier System (Six Channels) Model 2100
9. Vishay Instruments Gage Installation Tester Model 1300
10. Vishay Instruments Strain Indicator Model P-350A
11. Vishay Instruments Multi-purpose Digital Strain Indicator Model V/E-20A
12. Vishay Instruments Auxiliary Digital Strain Indicator Model V/E-13
13. Hewlett-Packard X-Y-Y' Recorder Model 7042A (Two Units)
14. Data Acquisition System PDP 1103 Model MINC-11 (supported in part by the Air Force Office of Scientific Research
15. Dunegan/Endevco 3000 Series Acoustic Emission Instrumentation (supported in part by NASA Langley Research Center)
16. Hewlett-Packard X-Ray Cabinet, Faxitron Model 43804N.
17. Wassco Glo-Melt Resistance Soldering Unit.

---

* Home-made units.

III. ACOUSTIC EMISSION INSTRUMENTATION

A. Introduction - A wide range of non-destructive inspection (NDI) techniques are used to detect internal damage and damage growth in composite systems. Ultrasonic pulse echo, brittle casting, Moiré, X-ray and neutron radiography, photoelastic coating, thermography, laser holography, acoustic emission and others are used to study those types of damage which are of principle concern, namely, delamination, matrix crazing and fiber failure. Monitoring acoustic emission appears to offer the most practical procedure for detecting damage and damage growth because it is more readily used in actual service as well as in the laboratory. This is crucial for composite systems since the composite material is fabricated during the manufacturing of the composite structure, thus some means of nondestructive testing of the complete component including data analyses in real-time is required. Therefore, it is not surprising that numerous works have focused on the applicability of acoustic emission to damage detection and monitoring in various composite systems (e.g.[29-37]).

Significant improvements and modifications have been made on acoustic emission instrumentation, including features for the detection and location of defects, amplitude analysis, frequency analysis, RMS, spatial discrimination, and voltage controlled gating, among others, which are coupled with data acquisition systems to display the information in real-time. The more modern systems enable determination, not only of the existence of damage, but of the type and extent of damage. From the information obtained, conclusions can be drawn as to location of specimen failure and the probable mechanism of failure.

In this current study, application of acoustic emission are an important tool in detecting damage progression. The tests are carried out using notched specimens for which damage progresses outwards from the notched area, i.e.

from the crack tip. The damaged area should be the primary source of acoustic emission signals. The rest of the material should be relatively "silent". Thus, the results will demonstrate whether the source locations technique can be used to locate damage, track damage progression and identify potential fracture sites in Gr/PI structures.

These tests were carried out for various crack length-to-width ratios from 0.02 to 0.5, and at different environmental temperatures as well as for unnotched specimens for all four laminates. It is expected that the results of the study will reveal the relationship between the manifested acoustic emission characteristics and factors such as damage size and material degradation. In other words, the acoustic emission characteristics should define the damage size and material degradation.

B. Instrumentation Capabilities: As mentioned above, the new modern and sophisticated acoustic emission instrumentation enables us to define the various failure mechanisms within the composite system and to track the location of activity. This failure characterization and the tracking procedures are achieved by analyzing certain characteristics of each acoustic emission event, such as peak amplitude distributions, rise time, counts, pulse duration, arrival time, etc. The selected instrumentation provides spatial discrimination, spatial filtering, and voltage controlled gating to eliminate unwanted background signals. The acoustic emission information is obtained by means of amplitude analysis and plotting of location.

Location Plotting: Linear location of defects is obtained using two transducers, one at each end of the specimen. The source of the event is located by measuring the difference in the time of arrival of the signal at the sensors. This location data is stored in memory and simultaneously displayed as a histogram on a monitor oscilloscope and reproduced on an X-Y recorder. Thus, a history of activities and location can be obtained.

Amplitude Analysis: This analysis provides amplitude distribution histograms of the various events. From such histograms the various failure mechanisms can be identified. Damage mechanisms which yield low amplitude emissions are characteristic of matrix crazing. The medium peak amplitudes are characteristic of delamination, while the higher peak amplitudes represent fiber fracture. The spectrum of amplitude values ranges between 30dB to 100dB. The spectrum of amplitude distribution is displayed on the monitor oscilloscope and reproduced with an X-Y recorder.

Spatial Discrimination: This technique separates unwanted background noise from valid data and is based on blocking signals from the ends of the specimen. Machine noise, grip noise and tab debonding are all screened from valid data. A four transducer set-up is used. Two inside data transducers are needed for the linear location plotting. Two guard transducers which are placed outside each data transducer function to discriminate machine and other unwanted noise from valid data. The spatial discrimination can be responsible for lowering the threshold amplitude down to 30 dB.

Voltage Controlled Gating: The operation of the linear location and amplitude data instruments can be controlled by an external analog signal such as the outputs of a load-cell, strain gage, etc. The VCG allows the system to operate only during a preselected portion of the load cycle, determined by a high and/or low limit pre-setting on the VCG. This procedure is particularly useful during cyclical test situations such as fatigue tests because it can deactivate the data taking systems when the load drops below a predetermined value, and thus eliminate the recording of unwanted information.

Counts and Events: An independent counting function is possible, displaying the number of counts from 0-999,999 in real-time. It is possible either to accumulate total counts or to obtain count rate. The total number of accumulative events can also be obtained up to 999,999 events in real-time. Both counts and events can be obtained from the entire specimen length or from a pre-set specific

area of interest, the so-called "window" in the specimen which serves as a spatial filter. Schematics of some of the available information obtained from the AE measurements are shown in Figures 5b and 5c.

C. Instrumentation - The list of modules acquired by our Composite Laboratory is listed in detail in the extension proposal (Drexel proposal number 2492) and will not be repeated here. The equipment used is shown in the block diagram in Figure 5a. In this section some of the most pertinent operating parameters are listed.

1. Threshold level used in Model 921 Amplitude Detector is 40 dB.
2. A fixed gain of 40 dB on Model 1801-170B preamplifier was used.
3. Voltage gain on Model 302A Dual Signal Conditioner is 40 dB.

   Therefore, the total system gain is 80 dB.
4. Envelope on Model 920A Amplitude Analyzer was set at 1 m sec.
5. Model 920A Amplitude Analyzer was set at "Locate" mode of test, to provide a location distribution historgram of events.
6. Amplitude distribution histograms were recorded from Model 922 External Memory.
7. Dead Time on Model 922 External Memory was set at 1 m sec.
8. Spatial filtering was achieved by setting the "window" on Model 920A Amplitude Analyzer at 10 ÷ 90. In a few cases a "window" range of 30 ÷ 70 was used.
9. Accumulative Events within the "window" were obtained from Model 920A Amplitude Analyzer.
10. Accumulative counts within the "window" were obtained from channel A of Model 303 Dual Counter.
11. Count Rate within the "window" was obtained from channel B of Model 303 Dual Counter.
12. Wherever Guard transducers were used, a voltage gain of 40 dB was set on the second available Model 302A Dual Signal Conditioner.
13. Wherever spatial discrimination was used, the Event Envelope Selector was set at 10 m sec on Model 420 Spatial Discriminator.

IV. RESULTS AND ANALYSES

A. Mechanical Properties - The experimental results on elastic stiffness and strength for all four laminates are listed in Table II, and they agree well with those reported elsewhere, e.g. [10]. A limited amount of data at elevated temperatures has been recorded so far, therefore those data will be reported later. However, the preliminary tests indicate that no significant variations of stiffness or strength are observed at the temperature ranges tested (up to 500°F), [10].

The values of the axial and transverse stiffness were obtained either with an extensometer of 25.4 mm (1.0 inch) gage length or with strain gages. Both techniques yielded similar results, verifying that the accuracy of the extensometer readings is satisfactory. The Poisson's ratio and the in-plane shear modulus were obtained with the strain gages described in Section II. Typical stress-strain curves for all four laminates are shown in Figure 6.

B. Load-Crack Opening Displacement Curves - As mentioned in Section II, two methods were used to obtain load-displacement curves for the center-notched laminates. The far-field load-displacement curves were obtained using the 25.4 mm (1.0 inch) compliance gage, while the load-COD curves were obtained using the IDG technique. An example of the far-field load-displacement curves for four different crack lengths for $[0/+45/90/-45]_{2s}$ laminate is shown in Figure 7. The load-COD curves for similar crack lengths are shown in Figure 8. A comparison between compliance gage load-displacement curves and IDG load-COD curves reveals the latter to be considerably more non-linear as the load approaches its ultimate values. Moreover, from the initial slope of both curves, Figures 7 and 8, it is clear that the initial slopes of the load-COD curves (IDG) are more sensitive to the size of the damage. A detailed examination of the load-COD curves also shows rapid increases in COD at the higher load levels.

TABLE II: MECHANICAL PROPERTIES

a. Unidirectional:

E_L = 135.76 GPa (19.69 x 10^3 ksi)
E_T = 9.31 GPa (1.35 x 10^3 ksi)
G_{LT} = 6.14 GPa (0.89 x 10^3 ksi)
ν_{LT} = 0.357
σ_f = Unavailable

b. $[0/+45/90/-45]_{2s}$ Laminate

E_x = 45.85 GPa (6.65 x 10^3 ksi)
ν_{xy} = 0.339
σ_f = 433 MPa (62.74 ksi)

c. $[\pm 45]_{2s}$ Laminate

E_x = 19.24 GPa (2.79 x 10^3 ksi)
ν_{xy} = 0.739
σ_f = 133 MPa (19.36 ksi)

d. $[90]_8$

σ_f = 49.8 MPa (7.22 ksi)

The actual crack opening is somewhat larger than indicated in Figure 8. However, no details are shown here because the fringe patterns of the IDG are lost as the load approaches approximately 95% of its ultimate value and, for all practical purposes, no data reduction is possible. The loss of the fringe patterns at this load range has been attributed to out-of-plane deformation in the central area of the crack due to local buckling because of transverse compressive stress building up. This out-of-plane deformation could also be attributed to the extensive crack tip damage at this load level as massive ply delamination expectedly occurs [38]. To verify the existence of local buckling, two strain gages were mounted on either side of the specimen, parallel to the center crack and along the same edge. A schematic representation of the strain gage readings is shown in Figure 9. Clearly, the response of the strain gages indicates local buckling of the sublaminates as the load approaches its ultimate value. It should be noted that in this load range the load-COD has already approached a plateau.

C. Compliance Curves - From both test procedures (IDG and Compliance gage), the compliance calibration as a function of the initial crack length has been calculated. Since two different displacements were measured, the appropriate compliances were defined accordingly: the local compliance, C_ℓ, is based on COD obtained from the IDG, and the global compliance, C_g, is based on the far-field displacement.

In order to obtain accurate data on the local compliance, each specimen was loaded to a predetermined load (about 10% of the expected failure load) and then unloaded. This procedure was repeated three times. An examination of the load-COD curve reveals that the unloading curves as well as the subsequent loading curves are linear. In some instances, the first unloading revealed a very small amount of permanent crack opening, approximately 1-2μm, which indicates a small amount of crack-tip damage. However, this damage is subcritical

and practically does not affect the compliance measurements. Figure 10 represents three initial loading curves together with the local compliance values, C_ℓ. It can be seen that the three values of C_ℓ are very close to each other, having a very small standard deviation (S.D.). The local compliance values given in Table III are the average values of the three loading curves. The global compliance values listed in Table III were obtained directly from the initial slope of the complete load-displacement curves when the recording system was set on high sensitivity to obtain good resolution.

The application of the energy release rate approach can predict the global compliance. The formulation is well established in the literature, e.g. [19], and will not be repeated here. The expression used for C_g prediction is:

$$C_g = \frac{\alpha}{E_x B}\left[1.566(2a/W)^2 + 0.268(2a/W)^3 - 0.438(2a/W)^4 + 1.865(2a/W)^5\right. \tag{3}$$

$$\left. + 0.247(2a/W)^6 - 0.393(2a/W)^7 + 0.911(2a/W)^8\right] + \frac{L}{BWE_x}$$

where W and B are the specimen width and thickness, respectively, L is the gage length of the compliance gage, and E_x is the axial stiffness of the laminate.

The orthotropic correction factor, α, (being 1 for quasi-isotropic laminates) is given by:

$$\alpha = \frac{1}{S_{22}}\left(\frac{S_{11}S_{22}}{2}\right)^{1/2}\left[\frac{S_{22}}{S_{11}} + \frac{2S_{12} + S_{66}}{2S_{11}}\right]^{1/2} \tag{4}$$

where S_{ij} are the orthotropic plate compliances and the width correction factor Y used in Equation (3) is [39]:

$$Y = 1 + 0.1282(2a/W) - 0.2881(2a/W)^2 + 1.5254(2a/W)^3 \tag{5}$$

Note that Equation (5) uses the isotropic width correction factor. It has been shown previously, e.g. [19], that this expression of Y is applicable for composites. Further discussion on the applicability of the isotropic width

correction factor to Gr/PI laminates will be discussed later in this Section.

A comparison between the experimental results for the global compliance and the prediction (Equation (3)) is shown in Figure 11. Surprisingly, the agreement is not as good as that previously obtained for other composite systems such as various boron/aluminum systems and graphite/epoxy laminates [19, 26, 27]. No explanation for the discrepancy between experiment and predictions can be given at this stage and it appears that additional tests should be performed.

The local compliance curve can be calculated from elastic stress analysis, predicting the crack opening displacement (COD) which has been measured experimentally from the interferometric displacement gage (IDG). The displacement v in the load direction of the center-notched composites is given by [40-42]:

$$v = a\sigma \left[S_{26} \cos \theta + S_{22} \frac{M}{k} \sin \theta\right] \tag{6}$$

where M and k are material parameters which can be related to α in Equation (4) so that $M/k = 2\alpha$, see details in [41-42].

In the current work, the COD was measured at the center of the crack, very close to the crack surface, and thus θ (the angle from the crack tip to location of indentation) is approximately 90°. Therefore, Equation (6) can be rewritten as:

$$v = \frac{2\sigma a \alpha}{E_x} Y \tag{7}$$

Since the COD is the relative displacement at the center of the crack, which is equal to 2v, the local compliance becomes:

$$C_\ell = \frac{COD}{BW} = \frac{2\alpha}{E_x B} \frac{2a}{W} Y \tag{8}$$

The predicted local compliance curve (Equation (8)), based on the isotropic Y, was compared with the experimental results, Table III, and an excellent agreement was established, as shown in Figure 12. The slight discrepancy between prediction and experiments is attributable mostly to the fact that θ in Equation (6) is not exactly 90°; the smaller the crack length, the smaller the angle θ will be, remembering that the distance between the two indentations (between which the COD is measured) is more or less fixed. The compliance curve however, has been plotted using a constant value of θ being 90°.

It is of interest to note that the local compliance curve (Figure 12) is much more sensitive to changes in crack length, i.e. damage size, than the global compliance curve, Figure 11. Therefore, the local compliance curve can also serve as a more accurate tool for calculating the crack growth resistance curve:

$$K_R = Y \sigma \sqrt{\pi a_e} \tag{9}$$

where a_e is the <u>effective</u> crack half-length obtained from the local compliance calibration curve.

The experimental compliance can also serve for calculating the width correction factor Y by rewriting Equation (8) as follows:

$$Y = \frac{E_x B}{2\alpha} \frac{C_\ell}{2a/W} \tag{10}$$

The term C_ℓ (2a/W) is the secant slope to each experimental value of the compliance in Figure 12. Thus Y is proportional to this slope. A comparison between the experimental results for Y and Equation (10) is shown in Figure 13, evincing quite a good correlation for the larger crack lengths. For the smaller crack lengths the scatter is quite high, but it must be remembered that any experimental scatter in compliance measurements causes a larger error in the slope, $C_\ell/(2a/W)$, for small crack lengths. Also, the analytical

TABLE III: EXPERIMENTAL VALUES OF LOCAL (C_ℓ) AND GLOBAL (C_g) COMPLIANCES FOR GRAPHITE/POLYIMIDE $[0/+45/90/-45]_{2s}$

Crack-Length mm	Crack-Length (inch)	C_ℓ $10^{-3}\mu/N$	Crack-Length mm	Crack-Length (inch)	C_g $10^{-3}\mu/N$
			0.43	(0.017)	4.29
			0.89	(0.035	4.18
2.11	(0.083)	1.34	2.11	(0.083)	4.61
			2.74	(0.108)	4.67
			5.33	(0.310)	4.83
5.51	(0.217)	2.41	5.51	(0.217)	5.30
10.31	(0.406)	4.53	10.31	(0.406)	-
10.36	(0.408)	4.28	10.36	(0.408)	5.44
			10.41	(0.410)	5.71
15.34	(0.604)	6.19	15.34	(0.604)	7.43
			15.34	(0.604)	7.34
15.55	(0.612)	5.91	15.55	(0.612)	6.73
20.45	(0.805)	8.11	20.45	(0.805)	9.62
			20.47	(0.806)	9.59
			20.47	(0.806)	9.76
			25.45	(1.002)	11.76
20.45	(1.004)	11.07	25.50	(1.004)	12.02

equations formulated for sharp cracks will no longer apply to real cracks of a smaller length, since the crack width-to-length ratio becomes larger. In adddition, any crack-tip damage will have a more significant effect on the elastic compliance so that the initial slope of the subsequent loading-unloading curve may not accurately represent the compliance. However, analytically, the deviation of Y from the isotropic values is negligible as the crack length gets smaller [43], and no K-calibration is needed for small cracks. Y is smaller than 1.001 for cracks having 2a/W less than 0.1, thus poor correlation for small cracks is of little significance.

D. Elevated Temperature Load-COD Curves - Elevated temperature load-COD curves and local compliances were obtained for $[0/+45/90/-45]_{2s}$ laminates. A comparison between room temperature (70°F) and elevated temperature (450°F) load-COD curves for a crack length of 15.37 mm (0.605 inch) is shown in Figure 14. The difference between the two curves indicates much larger crack-tip damage growth at elevated temperatures, which is mostly attributable to differences in the elevated temperature properties of the matrix material. A more detailed discussion on this effect is given later in the Section on acoustic emission. The effect of elevated temperatures on the deformation characteristics of the notched Gr/PI composite is already significant, even at low load levels, Figure 15. A comparison between the local compliances recorded at room and elevated temperatures shows the elevated temperature compliance to be increased by about 10% over the room temperature compliance.

E. Fracture Strength - Fracture strength results are listed in Table IV for various crack lengths. These data are compared with an existing model suggested by Waddoups, Eisenman and Kaminski (WEK) [44], who assumed the existence of intense energy regions at the edges of the notch which are modeled as edge cracks of size c_o. With this in mind, the linear elastic fracture mechanics is applied, and the fracture strength can be predicted

TABLE IV. NOTCHED STRENGTH DATA FOR GRAPHITE/POLYIMIDE $[0/+45/90/-45]_{2s}$

Crack Length		Notched Strength	
mm	(inch)	MPa	(ksi)
0.43	0.017	372	53.93
0.89	0.035	400	58.02
2.11	0.083	367	53.22
2.74	0.108	318	46.06
5.33	0.210	317	46.01
5.51	0.217	300	43.58
10.31	0.406	-	-
10.36	0.408	243	35.18
10.41	0.410	260	37.78
15.34	0.604	208	30.22
15.34	0.604	212	30.75
15.55	0.612	229	33.22
20.45	0.805	180	26.15
20.47	0.806	187	27.14
20.47	0.806	162	23.55
25.45	1.002	150	21.80
25.50	1.004	146	21.15

according to:

$$Y \frac{\sigma_f}{\sigma_o} = \left(\frac{c_o}{a + c_o} \right)^{1/2} \tag{11}$$

where σ_f and σ_o are the notched and unnotched strength, respectively. It should be noted that c_o can only be obtained experimentally by performing at least one fracture test, and must be determined for each composite system independently. A similar model has been mathematically formulated by Nuismer and Whitney [45], called the "average stress criterion", and which assumes that failure occurs when the average stress over a certain distance ahead of the crack-tip equals the unnotched strength. Both of these models have been widely used in recent years for predicting laminates' notch sensitivity, e.g. [46, 48]. However, this is a semi-empirical approach because c_o must be determined experimentally.

Since c_o is assumed to be a material property, i.e. a quantity independent of crack size, rearranging Equation (11) will give c_o as the slope of the following equation:

$$a = c_o \left[\left(\frac{\sigma_o}{Y\sigma_f} \right)^2 - 1 \right] \tag{12}$$

Figure 16 shows the experimental results plotted according to the format of Equation (12). The solid lines represent a least squares fit of c_o which was found to be 2.59 mm (0.109 inch). As seen in Figure 16, the use of a constant value for c_o for different crack lengths appears to be justified. Figure 16 also shows the results obtained recently [27] for Graphite/Epoxy (Gr/Ep) $[0/90/+45/-45]_s$ laminate with a specimen width of 25.4 mm (1.0 inch). Comparing the results for Gr/PI with those for Gr/Ep, it is seen that the latter has a much smaller c_o, indicating a higher notch sensitivity. Although the laminate stacking sequence of each material is somewhat different, and the size effect should also be taken into account (the width of Gr/PI is

double that of Gr/Ep), the differences in slope, as shown in Figure 16, are striking.

Using the values of c_o from Figure 16, the fracture strength can be predicted from Equation (11), Figure 17, and a good correlation has been established. Quite a significant notch sensitivy is observed for Gr/PI $[0/+45/90/-45]_{2s}$ laminate, however the Gr/Ep laminate shows an even higher notch sensitivity, Figure 18.

Values of the critical stress intensity factor, K_c, obtained from the equation:

$$K_c = Y\sigma_f \sqrt{\pi(a + c_o)} = \sigma_o \sqrt{\pi c_o} \tag{13}$$

are also given in Figures 17 and 18, and listed in Table V.

Another approach to analyzing the fracture strength data, suggested by Mar and Lin (ML-model), [49-51] is to assume:

$$\sigma_f = M(2a)^{-m} \tag{14}$$

where M and m are determined so as to best fit the data. This model interprets m to be "the order of singularity of a crack lying in the matrix with its tip at the interface of matrix and filament."

The data obtained in this program are plotted on a log $(Y\ \sigma_f/\sigma_o)$ versus log $(2a/W)$ format, Figure 19. A least squares fit yields the values of the slope m, of the coefficient M, and of the coefficient of correlation (c.c.), as shown in Figure 19 and as listed in Table V. It can be seen from Figure 19 that Equation (14) represents the data quite closely. Similar agreement has been established for several other composite systems, Table V [24-27, 52]. In order to compare these two approaches, Equations (11) and (14), the WEK model has also been plotted on a logarithmic format in Figure 20. A comparison between Figures 19 and 20 reveals that the first model, Equation (10), does more accurately represent the notch sensitivity of Gr/PI.

TABLE V: NOTCH SENSITIVITY*

Material	Average Unnotched Strength MPa	(ksi)	(Equation (13)) K_c MPa$\sqrt{m}$	(ksi$\sqrt{in}$)	(Equation (12)) c_o mm	(inch)	(Equation (14)) m	M	$Y\frac{\sigma_f}{\sigma_o}$ ($\frac{2a}{W}=0.3$)	$Y\frac{\sigma_f}{\sigma_o}$ ($\frac{2a}{W}=0.5$)
5.6 mil B/Al-6061F	2004	(290.7)	112.7	(102.6)	1.00	(0.0396)	0.321	0.313	0.3942	0.3653
8.0 mil B/Al-1100F	1273	(184.6)	108.4	(98.7)	2.31	(0.0910)	0.227	0.466	0.6207	0.5136
5.6 mil B/Al-6061F $[0/\pm22/0]_s$	1335	(193.7)	56.1	(51.0)	0.56	(0.0221)	0.371	0.226	0.3597	0.2835
BSiC/Ti-A	837	(121.4)	69.7	(63.1)	2.20	(0.0868)	0.258	0.449	0.6287	0.4858
BSiC/Ti-B	807	(117.4)	69.4	(63.1)	2.35	(0.0925)	0.277	0.452	0.6798	0.5125
5.6 mil B/Al-6061F, Type I	1290	(187.1)	107.3	(97.6)	1.15	(0.0455)	-	-	0.6304	0.4901
5.6 mil B/Al-6061F, Type II	1432	(207.7)	91.8	(83.5)	1.31	(0.0515)	-	-	0.5117	0.4077
5.6 mil B/Al-6061F, Type III	1526	(221.3)	91.9	(83.7)	2.20	(0.0867)	-	-	0.5136	0.3938
Gr/Ep AS/3501-5A $[0/90/\pm45/-45]_s$	609	(88.32)	34.5	(31.4)	1.02	(0.0401)	0.415	0.286	0.4718	0.3588
Gr/Ep AS/3501-5A $[0/\pm45]_s$	660	(95.69)	35.4	(32.2)	0.91	(0.0360)	0.322	0.299	0.4069	0.3810
Gr/Ep AS/3501-5A $[90/\pm45]_s$	197	(28.58)	23.5	(21.4)	4.54	(0.1787)	0.288	0.537	0.7753	0.6268
Gr/PI Celion 6000/PMR-15 $[0/+45/90/-45]_{2s}$	433	(62.74)	39.1	(35.5)	2.59	(0.102)	0.207	0.459	0.5280	0.4061

* All specimens are 25.4 mm (1.0 inch) wide. Only Gr/PI is 50.8 mm (2.0 inch) wide.

F. Notch Sensitivity - In studying the notch sensitivity of the different material systems it is customary to use the critical stress intensity factor, K_c, as a parameter indicative of notch sensitivity. Values of the critical stress intensity factor, Equation (13), are listed in Table V for twelve different material systems (including the present results on Gr/PI), along with the values of the unnotched strength, σ_o, and the crack-tip damage size, c_o. The actual changes in $Y(\sigma_f/\sigma_o)$, representing the actual notch sensitivity, are also displayed in Table V for the values 2a/W = 0.3 and 0.5.

Comparison of the K_c values with the values of $Y(\sigma_f/\sigma_o)$, Table V, shows that the K_c used in the two-parameter model, Equation (11), is not actually the proper indicator for notch sensitivity since it depends also on the unnotched strength. In other words, for high unnotched strength, K_c may be as high as 100 MPa $\sqrt{m}$ while values of $Y(\sigma_f/\sigma_o)$ indicate high notch sensitivity. Conversely, the trend in the values of c_o does follow the notch sensitivity characteristics as indicated experimentally by curve fitting Equation (11) with the experimental results. As long as this model, Equation (11) is accepted for predicting notched strength of composites, values of c_o can serve as a proper indicator of notch sensitivity.

Although Equation (14) is applied through a curve fitting procedure to determine the constants M and m, it is of interest to note that these constants can also serve as an indication of the notch sensitivity as determined in terms of changes in $Y(\sigma_f/\sigma_o)$. Smaller values of m and higher values of M indicate a lesser degree of notch sensitivity. As seen in Table V, both m and M values consistently follow the notch sensitivity of the various composite systems.

G. Axial Splitting - Notched unidirectional Gr/PI $[0]_8$ was tested for initiation and progression of crack-tip damage. It is well known that in unidirectional resin matrix composites, due to the brittle characteristics of the matrix material, splitting is generated at the crack tip along the fibers and in the

loading direction. It has been the objective of this program to determine the stresses at which such splitting is initiated, follow the axial cracking as a function of the far-field stress, and identify the damage growth by means of the laser interferometric displacement gage, X-ray radiography, ultrasonic C-scan, acoustic emission, and scanning electron microscopy.

Several notched unidirectional Gr/PI were tested with a $2a/W = 0.1$ and 0.3. Each specimen was loaded to a predetermined load and then unloaded, removed from the testing machine and X-rayed. This procedure was repeated several times incrementally up to failure. "Failure" is determined as the load at which splitting approaches the end-tabs of the specimen. For each load level the length of the axial cracks (splitting) was measured from the radiographs. During each loading-unloading cycle the extent of damage was monitored by means of acoustic emission.

Results on the length of the axial splitting, δ, as a function of load, measured from the radiographs, is shown in Figure 21 for two crack lengths. It is clear that initiation of splitting depends strongly upon the size of the crack and that it increases rapidly with applied load.

Since it is difficult to detect the initiation of splitting by the testing method described above, additional tests were performed using a crack propagation gage at the crack tip, as described in Section II-E. Here, initiation and progression of splitting could be followed very accurately, as shown in the insert of Figure 21. Again we see that, once splitting occurs, it progresses very rapidly with applied load.

The rapid extension of the splitting, δ, is manifested by the large crack opening displacement measured through the laser interferometric displacement gage. Load-COD curves obtained with the IDG for several loading cycles are shown in Figure 22. A detailed examination of the load-COD curves reveals rapid increases in COD when the load approaches the fracture strength. Such

behavior has also been found in other material systems, such as unidirectional boron/aluminum [24, 26]. These jumps in COD are indicative of discontinuities in the progression of the splitting. Examination of the δ-P curves of Figure 21 also give some indication that axial splitting progresses in a step-wise fashion. A continuous increase in δ is observed only at relatively low load levels. However, additional careful testing is required to confirm the nature and characteristics of the progression of splitting under load.

Radiographs of the split area for a crack length of 15.37 mm (0.605 inch) as a function of load are shown in Figure 23 together with results of the C-scan after failure. The axial splitting is clearly detectable from the radiographs and agrees well with the ultrasonic C-scan inspections. Results from acoustic emission and fracture surfaces will be discussed in a later Section.

H. Acoustic Emission (AE) - For all specimens tested in this program, acoustic emission was monitored using Dunegan/Endevco 3000 series AE instrumentation, and results were recorded as explained in Sections II-J and III. The following discussion will present some of the representative results obtained. The presentation will include results for all four laminates tested, notched and unnotched, and at room and elevated temperatures.

1. $[0/+45/90/-45]_{2s}$ laminate (unnotched): Figure 24 shows location distribution histograms of events for a total of twelve various loading stages on a linear scale. Note that the two diagrams are of different scales. Of interest is the fact that major activity occurred at the center of the specimen and at both ends. The AE activity at the specimen ends is primarily due to friction at the end tabs as well as to stress concentrations in the gripping area. In fact, the specimen failed at location "100". Significant amounts of activity also occurred throughout the specimen length. This is due to matrix cracking and crazing, or possibly to delamination or

fiber-matrix interface failure. Notably the X-ray radiographs of the specimen reveal significant amounts of matrix failure in the ±45° and 90° layers throughout the specimen length.

Figure 25 shows the amplitude distribution histograms for the various loading levels as indicated in the Figure (note that the two diagrams are of different scales). It seems that the amplitude level is attributable to matrix failure, although at this stage we cannot as yet identify which of the actual failure mechanisms is dominant.

The matrix failure progresses until the ±45° and 90° plies begin losing their load-carrying capacity. Most of the load is carried into the 0° plies, causing fiber failure. This fiber failure is associated with high amplitude levels and, in fact, several events appear in the 80 dB - 90 dB range as the load approaches its maximum value. This can be clearly seen in Figure 26 which shows the amplitude distribution for the same specimen as well as the Cumulative Event Amplitude Distribution (CEAD) on a logarithmic scale.

An amplitude distribution histogram displayed on a logarithmic scale is advantageous whenever a low number of events is occurring at specific amplitude levels, but it may conceal information whenever a large number of events occurs. Therefore we were using both linear and logarithmic scales for amplitude distributions. An example of this for a similar unnotched laminate is shown in Figure 27. The logarithmic scale indicates the occurrance of a few events in the high amplitude levels of 75 dB - 93 dB, which indicate fiber failure. The linear scale shows two distinct peaks of events, one at the 46 dB - 50 dB level and a second at the 54 dB - 58 dB level. As mentioned above, several matrix failure mechanisms are involved during the laminate failure, which most probably accounts for the occurrance of these two maxima. Additional studies would be required to correlate the specific failure mechanism with the amplitude distribution characteristics.

The "b slope" of the Cumulative Event Amplitude Distribution (CEAD) can be indicative of failure progression. This CEAD can be represented as [53]:

$$F(V) = F(V_o) \left(\frac{V}{V_o}\right)^{-b} \tag{15}$$

where V_o is the threshold value, V is the peak amplitude and "F(V) is defined as the number of events whose amplitude exceed V" [53] and is the CEAD. The constant b should be determined for each material system and deformation mechanism. More details can be found in [53]. Such a CEAD plot is shown in Figure 28 for seven different load levels. No attempt has been made at this stage to correlate the "b slope" with failure, and more testing is required before any conclusions can be made. However, it is interesting to note that as the load increases, the value of V_{max} (the peak amplitude of the largest emission) increases from about 52 dB up to 92 dB just prior to failure.

2. $[0/+45/90/-45]_{2s}$ Laminate (Notched): An example of a location distribution diagram for a notched quasi-isotropic laminate after failure is shown in Figure 29 in both linear and logarithmic scales. It is clearly seen that most of the activity occurred at the center of the specimen, exactly at the location of the notch. In other words, crack-tip damage growth could be easily detected. Very limited activity occurs in the rest of the specimen. The two peaks of events seen at locations "43" and "55" are most probably due to progression of matrix failure along the 45° plies toward the specimen edge.

The amplitude distribution of a notched laminate has a shape similar to that of the unnotched laminate. Although it seems that the number of events for the notched specimen is smaller (Figure 30) than for the unnotched specimen (Figure 27), care should be taken in regards to the "window" for which the amplitude distribution has been obtained. Note that the "window" in Figure 30 for the notched specimen is much smaller than the one in Figure 27 for the unnotched specimen. Generally, insufficient information is available at

this stage to draw definite conclusions from such a comparison. However, when CEAD for both cases is compared, it does seem that the "b slope" for the notched laminate is smaller than for the unnotched laminate regardless of the "window" range, Figure 31, and that the number of events at the high amplitude levels (up to 97 dB) is much larger for the notched specimen. This distinction in CEAD between notched and unnotched specimens has been observed in practically all of the specimens.

3. $[0/+45/90/-45]_{2s}$ Laminate (Notched) at 450°F: Location and amplitude distribution histograms for this case are shown in Figures 32 and 33, respectively. Comparing the results with those obtained at room temperature, Figure 34 and Figures 29 to 31, indicates that elevated temperatures have a marked effect on the characteristics of acoustic emissions. First, the amount of emission is significantly lower at the elevated temperature, Figure 32. Second, a relatively larger number of events appear in the higher amplitude range of 75 dB - 95 dB, while no distinct activity is observed in the 40 dB - 60 dB range, Figure 33. This can be attributed to the fact that the matrix material is less brittle at this temperature than at room temperature. Therefore, a lesser amount of matrix cracking occurs (in any form of the previously mentioned failure mechanisms) and consequently different levels and smaller amounts of acoustic emission events are manifested. Surprisingly, although the major activity occurs around the notch area (around location "53" in Figure 32), a significant amount of activity is also observed along locations "65" to "80", away from the crack tip.

4. $[90]_8$ (Notched): Very few events occurred during loading for this type of laminate, notched or unnotched, Figure 35. It is possible that the emission pulse was dispersed and damped before reaching the data transducer, and additional tests should be carried out at reduced threshold and increased

gain. However, calibration tests with a hand-held pulser did not show any significant amount of damping. Moreover, the limited amount of activity can be directly attributed to the low strength of the $[90]_8$ laminate in which specimen failure occurs soon after matrix failure. In this specific case, the major activity occurred around location "43" where the notch was located. Amplitude analysis within locations "40" - "46" is displayed in Figure 36, showing that the amplitude range is at the 40 dB - 55 dB level, which is the same range previously attributed to matrix failure.

5. $[\pm 45]_s$ Laminate: Location and amplitude distribution histograms after failure are shown in Figures 37 and 38 in both linear and logarithmic scales. Activity occurs throughout the specimen length, which is similar to the results obtained for $[0/+45/90/-45]_{2s}$ laminate. It is of interest to note that most of the activity occurred at location "72" and that the specimen subsequently failed within this approximate region (see radiograph in Figure 37). In other words, this acoustic emission test did succeed to indicate, a priori, the location of failure. However, such an agreement between the AE records and the actual site of failure did not always occur.

The amplitude distribution histogram, Figure 38, is quite different than that obtained for $[0/+45/90/-45]_{2s}$ laminate, Figures 25-28. While only a few number of events occur at the 40 dB level, most activity occurs at the 50 dB - 60 dB level, accompanied by a significant amount of high amplitude events, 75 dB - 95 dB. In other words, the amplitude distribution histogram for $[0/+45/90/-45]_{2s}$ laminate is skewed to the left, while the amplitude distribution histogram for $[\pm 45]_s$ laminate is skewed to the right.

6. $[0°]_8$ (Notched): As discussed earlier, notched unidirectional Gr/PI composites exhibit axial splitting under tensile loading. Location distribution

of events for such a specimen is shown in Figures 39 and 40 for the different load levels. The distinct accumulation of events at ten specific sites is typical to all such specimens. One explanation can be that the axial splitting progresses in a discontinuous manner, and each time it is arrested somewhere along the specimen, transverse extension of damage creates additional acoustic activity. This is similar to the failure mechanism described for boron/aluminum [24, 26]. Amplitude distribution histograms are shown in Figure 41. As expected, most events occurred at the 40 dB - 60 dB level (matrix failure mechanism), while only a few events occurred at the high peak amplitude level (fiber failure).

7. $[0°]_8$ (Unnotched): Figures 42 and 43 show location and amplitude distribution histograms, respectively, for unnotched unidirectional Gr/PI. Both distributions are strikingly similar to those obtained for unidirectional notched specimens, Figures 39-41. Characteristics are practically the same. In fact, post-failure examination of unnotched unidirectional specimens also reveals a significant amount of axial splitting, primarily due to damage existing in the specimen prior to loading. Although failure of unnotched unidirectional specimens is referred to as "fiber-controlled" failure, it should be noted that most of the activity again occurred at peak amplitudes in the 40 dB - 50 dB level.

8. Kaiser and Felciity Effects: In the detection of damage growth through monitoring acoustic emission, it has been demonstrated for many isotropic materials that acoustic emissions occur only when the material is loaded beyond a previously applied load level, referred to as the Kaiser Effect [54]. Composite materials, however, behave somewhat differently, with emissions occurring below the previous load level. This phenomenon in composites is called the "Felicity Effect" [36-37], and the ratio of the load at onset of emission to the maximum previous load is defined as the"Felicity Ratio"[37].

This effect has been studied in the current work for various Gr/PI laminates.

Several $[0/+45/90/-45]_{2s}$ laminates were loaded to a predetermined load and then unloaded. This procedure was repeated incrementally up to failure. During the tests, events, counts, count rate, location and amplitude distribution histograms, and CEAD were recorded.

A schematic representation of events and counts versus load during the unloading/reloading cycle is shown in Figure 44. Deviation from the Kaiser Effect is clearly seen, i.e. emissions occur prior to the previous load level. In other words, the phenomenon referred to as the Felicity Effect has been verified. However, it was also found that emissions occurred during the early stages of unloading. Only upon further unloading does the material become acoustically "silent". More important, during the reloading stage, emissions began again at exactly the same load level at which the material had become "silent" during the unloading stage, Figure 44. This last phenomenon was observed for each unloading/reloading cycle (a total of eighteen cycles) irrespective of the load or the total emission levels.

The fact that emissions also occur during the early stages of unloading can be attributed to internal friction of fracture surfaces in the damaged areas within the specimen. This is due to the crack closure process during load removal. These internal cracks will then emit noise upon reloading when they are reopened, due to the same internal friction. Such explanation can also be verified by analyzing the amplitude distribution histogram shown in Figure 45. Two curves are shown: curve "1" is for the distribution recorded during the first loading to 15.57 KN (3500 Lbs). Then the specimen was unloaded/reloaded, and amplitude distribution was recorded again at the previous load level, curve "2". All of the additional emission is in the 40 dB - 65 dB level, and both curves are practically parallel to one another.

A similar test was performed for notched $[0°]_8$ Gr/PI. The specimen was loaded to a predetermined load, causing axial splitting of approximately 50 mm in length, and then unloaded/reloaded several times. Emissions occurred during all loading cycles and during the entire unloading cycle down to zero load. When the specimen was reloaded, emission occurred immediately upon application of load. As mentioned above, this behavior is attributed primarily to the internal friction between adjacent fracture surfaces during the unloading/reloading cycle. Another way of presenting the emission activity during the unloading/reloading cycle is by monitoring count-rate, as shown in Figure 46, which indicates the same phenomenon.

This modification in the Felicity Effect may distort the acoustic emission records for cyclic loading tests. However, it may be of significant importance in detecting existing damage. It can, in fact, serve as an "early warning" system for either proof-loaded structures or for those rare cases when the previously applied load is unknown. The degree of this "early warning" can also be quantified through the Felicity Ratio;

$$F = P_{i2}/P_{i1} \tag{16}$$

where i is the cycle number (see Figure 44).

This ratio of P_{i2}/P_{i1} as a function of the percent of ultimate load has been plotted in Figure 47 for three different specimens. The solid lines represent an eyeball fit of the data. It can be seen that for the stronger materials (high failure load - P_f) the slope of these lines is smaller. Since the Felicity Ratio F cannot be larger than 1.0 (though it has been argued otherwise in [37]), all three lines were extended up to the point at which acoustic emission initiated (point A in Figure 47). Although a limited number of tests were performed, it would seem that the slope of the Felicity Ratio curve can also serve as an indicator of material strength, e.g. as an acceptance-rejection

criterion and as an indicator for allowable load.

In regards to the monitoring of counts and events, a large amount of counts is generally being recorded for unnotched Gr/PI composites, in the order of 10^5, as compared with the total number of events, in the order of 10^3. The number of counts per event may vary depending upon the load level and the amount of damage. Initially, about 2-6 counts accompany each event, but with increasing load the count per event can be 20 or higher. This phenomenon might be attributed to one of the following two reasons or a combination of both: 1) As damage progresses and the number of events increases, it may happen that two or more events interfere, depending also upon the duration of "Dead-Time" set in the instrumentation. When several events interfere, the system will register all of them as one event which includes some combination of the counts of the individual events; 2) As damage increases, higher amplitude events occur, possibly due to fiber failure, and thus a larger number of counts above the threshold level set in the system may be recorded.

Therefore the variation in counts per event with load might be attributed either to instrumentation setting or to variation in failure mechanism or to a combination thereof. In any case, the absolute number of events or counts recorded does not necessarily represent the actual degree of damage. The recorded data are of a random representation of the total amount of emission.

Some preliminary measurement of the number of events occurring during the unloading stage as a function of the maximum applied load P_{il} (Figure 44) shows that the number also increases with load, and that it depends heavily on the P_{il}. However, more testing will be required to understand the significance of this phenomenon.

I. Failure Modes and Fracture Surfaces - The general appearance of the failed Gr/PI laminates is very similar to that of other resin matrix composites, such as graphite/epoxy (Gr/Ep). Except for the $[90]_s$ specimen, all three other laminates remained intact after failure; the $[0/+45/90/-45]_{2s}$ and $[\pm 45]_s$ were held together by the internal friction between adjacent 45° plies. An extensive amount of delamination, fiber failure and matrix cracking appeared at the crack tip, and the 45° layers broke along the fiber directions. As evidenced by the radiographs, delamination and matrix cracking along the fiber directions occurred all along the specimen gage length. No evident difference between notched and unnotched specimens in the general failure pattern could be distinguished. A few of the $[0]_8$ specimens failed with the typical brush-like failure, although it was much less extensive than that found in unidirectional Gr/Ep. For most specimens, several axial cracks (splitting) appeared during loading, the length of which increased with applied load. Failure was defined as the load at which the splitting extended to the end-tabs, and this was much below (by about 25%) the expected ultimate strength. The type of gripping used in this work (see Section II-B) is most probably responsible for this type of failure. Although in many cases the splitting initiated within the gage length, in other cases it also initiated in the gripping region. Therefore additional testing is required in which standard glass/epoxy end-tabs are applied.

For three virgin specimens, photomicrographs of the cross-sections were prepared. Examples of such photomicrographs for $[0/+45/90/-45]_{2s}$, $[\pm 45]_{2s}$ and $[0]_8$ are shown in Figures 48, 49 and 50, respectively. These photographs are typical of the entire cross-section examined. It is of interest to note that resin rich areas are noticeable between all layers in all three laminates, so that each individual layer was easily distinguishable. Although fiber

distribution within each layer was quite uniform, in some cases, such as Figure 49, a noticeably low fiber volume fraction was observed. Additional micrographic examinations are warranted for failed specimens at various environmental temperatures.

Scanning electron microscope (SEM) photographs of the fracture surfaces were also taken. In order to obtain a better view of the fracture surfaces and better understand the different failure mechanisms, three-dimensional (stereo) views were obtained as well. Figures 51 and 52 represent views of fracture surfaces of $[0/+45/90/-45]_{2s}$ notched and unnotched, respectively. Figure 53 shows the fracture surface of a $[90]_8$ specimen, and Figure 54 shows the fracture surface of the split area of a notched unidirectional specimen. The following general observations can be made in regard to the failure modes:

1. Fiber surfaces are clean of matrix material, indicating poor bonding between fibers and matrix, Figures 51 to 54.

2. There are large amounts of matrix material debris clinging to the fiber surfaces and throughout the fracture surface, Figures 51, 53 and 54.

3. There is a relatively large amount of fiber fracture and, in many cases, failure of the complete tows and even groups of tows, Figures 51 to 54, Surprisingly, this type of failure was also observed in the $[90]_8$ specimen.

4. Cracks, parallel to the fiber direction, were also pronounced in the $[90]_8$ specimen, Figure 53.

5. A rugged, rather than planar, fracture surface is observed. This irregularity is in the direction of the specimen thickness and can be seen only by using the stereo viewer. These irregular surfaces are also pronounced in the $[90]_8$, Figure 53, and in the split area of the notched $[0]_8$, Figure 54.

6. The matrix deformation in the 45° layers includes small serrations which are dense and numerous, Figure 51, while in the $[90]_8$ specimen, mostly cleavage is observed, Figure 53.

It is of interest to note that the matrix deformation of the polyimide is quite different than that observed in Gr/Ep [27]. In the latter, larger and more numerous serrations are observed. Also, the amount of scattered debris is much more limited in Gr/Ep. This might possibly be attributed to the amount of resin rich areas observed in the photomicrographs of Figures 48 to 50. A more detailed discussion on the deformation characteristics and failure modes can be found in [27, 55].

J. Ultrasonic C-Scan - As explained in Section II-F, all specimens were C-scanned to determine and evaluate the degree of internal damage due to fabrication inhomogeneities. In fact, many specimens were C-scanned several times (5-8 times), varying the detecting parameters to ensure confidence in the results. Also, several operators were employed in order to obtain more objective results. This procedure was applied because of the large variations obtained in the C-scan measurements.

An example of C-scan records is given in Figure 55 for Gr/PI $[\pm 45]_{2s}$ laminate. Due to warpage and internal delamination, this plate was of poor quality, Table I, as determined by preliminary C-scan examination conducted by NASA LaRC, Section II-F. In fact, the C-scan records shown in Figures 55a to 55e demonstrate the poor quality of this plate as compared with a good quality $[\pm 45]_{2s}$ plate, Figure 55f. However, there is considerable variation in the results shown; five individual records of Figures 55a to 55e were obtained by varying the gain and delay time, and were conducted on different dates (i.e. with possible slight variations in water height and temperature, in focal distance from the reflecting plate, and the slant of the plate, etc.). The variations in the C-scan records can be clearly seen. In other words, although we succeeded in distinguishing between good and bad quality plates, the degree of internal damage and the actual size, shape and location of this damage are questionable.

Figure 55g shows a radiograph of the same specimen shown in Figures 55a to 55e. The general appearance of the radiographs is quite similar to the C-scan records, although it is hard to match the details of location and extent of damage in both types of records. Moreover, the radiographic records strongly depend upon the method by which the D.I.B. penetrant is applied. When the penetrant is carefully applied only along the edges of the specimen, very little "damage" is displayed. However, when it is applied also on the specimen flat surface, Figure 55g, the extent of "damage" is much greater. This is due to the roughness, the amount of grooves, existing on the plate surface, created during fabrication. Additional comparisons between radiographs and C-scan examinations in specimens which exhibited primarily free-edge delamination showed mixed results. In other words, a correlation could not always be found between these two types of examination.

As mentioned in Section II-F, the C-scan examinations were conducted in order to screen between poor and good specimens and to compare those results with mechanical testing results. Results on ultimate strength of the "good" and "poor" $[\pm 45]_{2s}$ laminates, show the latter to have lower values by approximately 10 percent. In addition, heating the "poor" specimens up to 500°F caused additional warpage and large amounts of acoustic emission at an audible level. Thus, additional tests at room and elevated temperatures are yet warranted.

K. Elevated Temperature Tests - In addition to the elevated temperature tests described in Sections IV-D, IV-H and IV-L, a few tests were conducted to obtain the variation in stiffness and strength with temperature. In order to eliminate the effect of inherent material scatter, each of the specimens was first tested at room temperature for stiffness measurements, unloaded, heated up to 450°F, and retested to failure. The results indicate that for $[0/+45/90/-45]_{2s}$ and $[0]_8$ no variation in either stiffness or strength due to temperature was

found, which agrees with results obtained elsewhere [10]. However, the $[90]_8$ specimen results were markedly affected by temperature; both transverse stiffness and strength were reduced by about 25% and 35%, respectively, from room temperature values. This agrees well with the observations from load-COD, acoustic emission and NMR results, all of which indicate variations in matrix properties at elevated temperatures. Thus, additional detailed studies on this effect should be conducted.

L. Pulsed Nuclear Magnetic Resonance (NMR) Measurements - It has been shown by various authors [56,57] that pulsed NMR can be used to elucidate certain aspects of polymer structure and those properties which are affected by molecular mobility. In particular, the spin-spin relaxation time, T_2, which is primarily determined by the relatively slow translatory motion of the chain in the fluid state was found useful in investigating polymer structural order, chain entanglement and the presence of permanent crosslinks. This versatile technique can be applied to polymers in the solid state, the liquid state or as composites with inorganic or proton-free fillers. In general, it was found that short polymer chains in the liquid state or at high temperature in the molten state will give a single exponential T_2 decay. When the molecular weight exceeds a critical value, however, the spin-spin relaxation deviates from the single exponential behavior. This was explained by the presence of molecular entanglements at the higher molecular weights sufficient in number to provide a three-dimensional network. These entanglements persist over a sufficient length of time so as to restrict the chain mobility.

Below the polymer's melting point, the T_2 decay spectrum, in general, has two distinct components, and represents two distinct regions, the crystalline and the amorphous domains. At longer times, the decay tends to be a single exponential which represents the more mobile region. The initial portion, on the other hand, is non-exponential and in many systems (e.g. polyethylene)

was found to be Gaussian in form. The present result on pure polyimides seem to conform with this picture well as can be seen in the spectrum presented in Figure 56 at 400°F. When the total curve was subtracted from the exponential base line (dotted), the result (ΔS) was linear with the square of the time confirming that a Gaussian type decay is followed.

Figure 57 shows the decay pattern for the same resin at different temperatures. As expected, the mobile fraction of the resin (the exponential end) appears to increase with temperature while the initial Gaussian portion diminishes with temperature over the range 300°F to 400°F. At 400°F the relaxation pattern can be represented by the Equation:

$$\frac{S}{S_o} = 0.32 \text{ EXP } (-t/30) + 0.68 \text{ EXP } (-t/22.3)^2 \qquad (17)$$

Where $\frac{S}{S_o}$ is the normalized signal, 0.32 represents the proportion of the mobile fraction and 0.68 the less mobile segment. The value of T_2 in these two regions are 30 μ sec and 22.3 μ sec, respectively. From these values one can estimate that the change in mobility between the two regions is minimal. In a semi-crystalline polymer, e.g. Polyethylene, this change is about two orders of magnitude apart. The present system, however, is very rigid and therefore the relative increase in mobility is small.

V. RESULTS AND CONCLUSIONS

In this progress report we have presented and analyzed experimental results on various aspects of the fracture behavior, deformation characteristics and failure modes of several graphite/polyimide Celion 6000/PMR-15 laminates. It has been demonstrated that the testing methodology employed in this program, namely the use of a variety of experimental techniques, is pertinent and even necessary, to the study of a new material system. A summary of the results presented in this report is given below:

1. Compliance curves: good correlation with predictions (energy release rate and COD).

2. Calibration curves: isotropic width correction factor can be applied.

3. Fracture strength: concept of critical damage zone size can be applied for graphite/polyimide laminates.

4. Notch sensitivity: somewhat smaller than that of graphite epoxy.

5. Load-COD curves: good indicator for crack tip damage. Slow crack tip damage growth has been observed. At high load levels out-of-plane deformation occurs.

6. Notched unidirectional Gr/PI: longitudinal cracks (splitting) progression is discontinuous (Load-COD, AE, Radiography).

7. Fracture surface studies: a combination of several interdependent failure modes such as fracture of individual fibers and fiber tows, matrix serration (shear failure), matrix cleavage and matrix/interface failure.

8. SEM results:

   Matrix serrations - mostly in 45° plies (much smaller than in Gr/Ep); shear failure.

   Fiber failure - in 90° plies as well as along axial splitting

   Poor interface - clean fibers in all layers

   Matrix debris - large amount of matrix debris in all layers

   Fracture surfaces - highly irregular, also in $[90]_8$ and in axial cracks.

9. Photomicrographs: resin rich areas between plies. A uniform fiber distribution.

10. X-Ray radiography: helpful in detecting damage at free surfaces such as crack tips. Good correlation with acoustic emission.

11. Ultrasonic C-scan: sensitive to detection parameters and operator. Results are questionable. Very poor correlation with X-ray radiography, no correlation with acoustic emission.

12. Acoustic emission: qualitative correlation exists between acoustic emission events and deformation characteristics as detected in the load-COD curves.

13. AE information includes: accumulative counts and events, count rate, location and amplitude distribution histograms, pulse width, and Cumulative Event Amplitude Distribution (CEAD), all in real-time.

14. AE results: demonstrate a possible distinction between various failure mechanisms of different laminates, detection of initiation and progression of damage (failure site), and screening of weak specimens.

15. Kaiser and Felicity effects: it has been determined that emission starts at about 90 percent of the previous load level.

16. Effect of unloading/reloading cycle: a clear indication that, during reloading, emission starts exactly at load level at which the material became acoustically silent during the unloading stage.

17. The Felicity effect: the early initiation of emission does not necessarily mean additional damage. Most probably existing damage is the cause of this emission. Therefore, existence of the Felicity effect does not contradict the Kaiser postulate.

18. Felicity ratio: shows potential as an acceptance-rejection criterion.

19. Acoustic emission potential: exists as an NDI tool. However, expectations will remain too high, encouraging skepticism, unless:

    a. Basic studies are carried out on the constituents and "simple" composite structures.

    b. Acoustic emission instrumentation is interfaced with data acquisition systems.

    Data on accumulative counts are insufficient for determining material susceptibility to failure!

20. Elevated temperature tests: load-COD curves successfully obtained. Good control in applying high temperature strain gages.

21. Effect of elevated temperature: no effect on global laminate properties up to 500°F. Indication on local effects:

    a. Local compliance curve.

    b. Load-COD curve.

    c. Acoustic emission outputs.

    d. Matrix controlled failure mechanisms.

22. Pulsed Nuclear Magnetic Resonance (NMR) studies: reveal the existence of two distinct regions in the polyimide resin; one mobile, the other of lesser mobility.

23. Pulsed NMR results: the mobile fraction of the resin is insignificant at 300°F but increases with temperature.

24. The fraction of the mobile region and its relative mobility, determined by the proton spin relaxation time, can be determined quantitatively and correlated to the matrix degree of cure.

VI. RECOMMENDATIONS

The results of this work indicate that elevated temperatures do possibly have an effect on the fracture behavior, deformation characteristics, failure modes, and microstructures of graphite/polyimide composites. Also, the potential of some of the testing methods and concepts employed in this program, such as NDI, acoustic emission, NMR and others, deserve to be investigated in more detail. It is therefore our recommendation that the following general subjects should be pursued.

1. A detailed study on the effect(s) of elevated temperatures on crack tip damage, damage growth, notch sensitivity, failure modes, damage mechanisms, etc. should be conducted.

2. All the described testing methodology should be applied in such a program, including acoustic emission, radiography, SEM, NMR, etc.

3. Basic material properties should be included in studies on graphite/polyimide systems.

4. The concept of critical damage zone size as a material parameter used in predictions of notched strength should be thoroughly examined.

5. Potential application of monitoring acoustic emission to damage detection should be pursued. However, more efficient and consistent studies are warranted:

    a. Studies should be carried out on the constituents and "simple" composite structures to obtain "base-line" data.

    b. Acoustic emission instrumentation should be interfaced with data acquisition systems to provide parametric analyses capabilities.

c. The validity of the Kaiser and Felicity effects for graphite/polyimide systems.

d. The effect of various types of fabrication anomalies on the progress of failure.

e. Specific acoustic emission acceptance-rejection criteria.

6. The use of nuclear magnetic resonance (NMR) to:

a. Measure the effect of lamination on the mobile segment of the composite matrix.

b. Extend the temperature effect data to the composite's operating temperature (about 550°F).

c. Correlate the relaxation time data to change in modulus at different temperatures.

d. Correlate the proton spin relaxation times and the mobile fraction to the matrix degree of cure.

REFERENCES

1. T. T. Serafini, P. Delvigs and G. R. Lightsey, "Thermally Stable Polyimides from Solutions of Monomeric Reactants," J. of Appl. Polymer Science, Vol. 16, 1972, pp. 905-915.

2. T. T. Serafini, "Processable High Temperature Resistant Polymer Matrix Materials," Proc. of the 1975 International Conference on Composite Materials (ICCM), 1975, pp. 202-220.

3. T. T. Serafini and P. Delvigs, "PMR Polyimides Prepeg with Improved Tack Characteristics," Proc. of the 1978 International Conference on Composite Materials (ICCM), 1978, pp. 1320-1329.

4. P. Delvigs, T. T. Serafini and G. R. Lightsey, "Addition-Type Polyimides from Solutions of Monomeric Reactants," 17th National SAMPE Symposium and Exhibition, SAMPE, Vol. 17, 1978, pp. III-B-7-1-III-B-7-15.

5. T. L. St. Clair and R. A. Jewell, "LARC-160: A New 550°F Polyimide Laminating Resin," 8th National SAMPE Technical Conference, Vol. 8, 1977, pp. 82-93.

6. I. Petker and B. A. Stern, "Microstructure, the Interface and the Structural Performance to 700°F of Graphite/Polyimide Composite," Proc. of the 23rd National SAMPE Symposium and Exhibition, SAMPE, Vol. 23, 1978, pp. 775-790.

7. T. L. St. Clair and R. A. Jewell, "Solventless LARC-160 Polyimide Matrix Resin," Proc. of the 23rd National SAMPE Symposium and Exhibition, Vol. 23, SAMPE, 1978, pp. 520-527.

8. J. S. Jones, "Graphite/Polyimide Composite Materials System for Potential Space Shuttle Use," 21st National SAMPE Symposium and Exhibition, SAMPE, Vol. 21, 1976, pp. 438-458.

9. I. Petker, "Polyimide Resins in Advanced Composites - A Current Assessment," 21st National SAMPE Symposium and Exhibition, SAMPE, Vol. 21, 1976, pp. 37-49.

10. H. B. Dexter and J. G. Davis, Jr., "Graphite/Polyimide Composites," NASA Conference Publication 2079, Proceedings of Technical Symposium, held at Langley Research Center, February 28 - March 1, 1979.

11. R. D. Vannuci, "Effect of Processing Parameters on Autoclaved PMR Polyimide Composites," Proc., 9th National SAMPLE Technical Conference, Vol. 9, 1977, pp. 177-199.

12. T. T. Serafini, P. Delvigs, and R. D. Vannuci, "In Situ Polymerization of Monomers for High-Performance Poly (Phenylguinoxaline)/Graphite Fiber Composites," J. of Appl. Polymer Sci., Vol. 17, 1973, pp. 3235-3238.

13. P. Delvigs, L. C. Hsu, and T. T. Serafini, "The Synthesis of Novel Polyimide Precursor," J. of Polymer Sci. B, Vol. 8, 1970, pp. 29-35.

14. W. E. Winters and T. T. Serafini, "PMR Polyimides - Precessable High Temperature Composite Matrix Resins," 20th National SAMPE Symposium and Exhibition, SAMPE, Vol. 20, 1975, pp. 629-643.

15. H. H. Gibbs, "The Aging Characteristics of NR-150 Polyimide Binder System," 7th National SAMPE Technical Conference, Vol. 7, 1975, pp. 244-259.

16. H. H. Gibbs, "NR-150 Polyimide Binders - A New Approach to High Performance Composites," 17th National SAMPE Symposium and Exhibition, SAMPE, Vol. 17, 1972, pp. III-B-6-1-III-B-6-9.

17. D. F. Sims, D. N. Weed, and P. H. Francis, "Experimental Evaluation of Polyimide Composite Materials," Proc. of the 1978 International Conference on Composite Materials, (ICCM), 1978, pp. 91-99.

18. I. M. Daniel and T. Liber, "Lamination Residual Stresses in Fiber Composites," NASA CR-134826, 1975.

19. J. Awerbuch and H. T. Hahn, "K Calibration of Unidirectional Metal Matrix Composites," J. Composite Materials, Vol. 12, 1978, pp. 222-237.

20. W. N. Sharpe, Jr., "Preliminary Development of an Interferometric Strain Gage for Use on Nosetip Materials Subjected to Thermal Shock," AFML-TR-76-63 Air Force Materials Laboratory, 1976.

21. F. A. Jenkins and H. E. White, Fundamentals of Optics, McGraw-Hill, New York, 1957.

22. D. E. Macha, W. N. Sharpe, Jr. and A. F. Grant, Jr., "A Laser Interferometry Method for Experimental Stress Intensity Factor Calibration," ASTM STP 601, American Society for Testing and Materials, 1976, p. 490.

23. W. N. Sharpe, Jr., "Interferometric Surface Strain Measurement," International Journal of Nondestructive Testing, Vol. 3, 1971, p. 56.

24. J. Awerbuch and H. T. Hahn, "Crack Tip Damage and Fracture Toughness of Boron/Aluminum Composites," J. Composite Materials, Vol. 13, 1979, pp. 82-107.

25. J. Awerbuch and H. T. Hahn, "Crack Tip Damage and Fracture Toughness of Borsic/Titanium Composites," to be published in Experimental Mechanics, October 1980.

26. J. Awerbuch, "Effect of Constituents on the Fracture Behavior of Unidirectional Boron Aluminum Composites," to be published.

27. J. Awerbuch, "Deformation Characteristics and Failure Modes of Center Notched Graphite/Epoxy Laminates," to be published.

28. B. W. Rosen, "A Simple Procedure for Experimental Determination of the Longitudinal Shear Modulus of Unidirectional Composites," J. Composite Materials, Vol. 6, 1972, pp. 552-554.

29. C. D. Bailey, J. M. Hamilton, Jr., and W. M. Pless, "Acoustic Emission of Impact-Damaged Graphite-Epoxy Composites," Materials Evaluation, pp. 43-54, May 1979.

30. J. T. Ryder and J. R. Wadin, "Acoustic Emission Monitoring of a Quasi-Isotropic Graphite/Epoxy Laminate Under Fatigue Loading," Lockheed-California and Dunegan/Endevco Companies, Internal Report.

31. M. A. Hamstad, "Variabilities Detected by Acoustic Emission from Filament-Wound Aramid Fiber/Epoxy Composite Pressure Vessels," International Instrumentation Symposium, Vol. 24, pp. 419-431, 1978.

32. J. M. Carlyle, "Imminent Fracture Detection in Graphite/Epoxy Using Acoustic Emission," Experimental Mechanics, pp. 191-195, May 1978.

33. R. L. Randall and L. J. Graham, "Acoustic Emission Characterization Systems," International Instrumentation Symposium, pp. 439-444, 1978.

34. A. Arora and K. Tangri, "On Methods of Structural Integrity Evaluation by Acoustic Emission," Int. J. of Fracture, Vol. 15, 1979.

35. R. G. White and H. Tretout, "Acoustic Emission Detection Using a Piezoelectric Strain Gauge for Failure Mechanism Identification in CFRP," Composites, pp. 101-109, 1979.

36. T. J. Fowler, "Acoustic Emission Testing of Fiber Reinforced Plastic Equipment," ASME Design Engineering Conference, Chicago, May 1979.

37. T. J. Fowler and E. Gray, "Development of an Acoustic Emission Test for FRP Equipment, ASCE Winter Convention, Boston, April 2-6, 1979, preprint 3583.

38. F. H. Chang, J. C. Couchman, J. R. Eisenmann, and B. G. W. Yee, "Application of a Special X-Ray Nondestructive Testing Technique for Monitoring Damage Zone Growth in Composite Laminates," Composite Reliability, ASTM STP 580, American Society for Testing and Materials, 1975, pp. 176-190.

39. W. F. Brown and J. E. Strawley in "Plane Strain Crack Toughness of High Strength Metallic Materials," ASTM STP 410, American Society of Testing and Materials, 1966, p. 11.

40. G. C. Sih and H. Liebowitz, "Mathematical Theories of Brittle Fracture," in Fracture, Vol. 2, 3d. H. Liebowitz, Academic Press, N. Y., 1968.

41. S. G. Lekhnitskii, Theory of Elasticity of an Anisotropic Elastic Body, Translated by P. Fern, Holden-Day Inc., 1963.

42. S. G. Lekhnitskii, Anisotropic Plates, Traslated by S. W. Tsai and T. Cheron, Gordon and Breach Science Publishers, N. Y., 1968.

43. I. M. Daniel, R. E. Rowlands and J. B. Whiteside, "Deformation and Failure of Boron/Epoxy Plate with Circular Holes," The Test Methods for High Modulus Fibers and Composites, ASTM STP 521, American Society for Testing and Materials, 1973, p. 143.

44. M. E. Waddoups, J. R. Eisenmann and B. E. Kaminski, "Macroscopic Fracture Mechanics of Advanced Composite Materials," J. Composite Materials, Vol. 5, 1971, p. 446-454.

45. R. J. Nuismer and J. M. Whitney, "Uniaxial Failure of Composite Laminates Containing Stress Concentrations," in Fracture Mechanics of Composites, ASTM STP 593, American Society of Testing and Materials, 1975, pp. 117-142.

46. Y. T. Yeow, D. H. Morris and H. F. Brimson, "A Correlation Study Between Analysis and Experiments on the Fracture Behavior of Graphite/Epoxy Laminates," Virginia Polytechnic Institute and State University, VPI-E-77-20, 1977.

47. Y. T. Yeow, D. H. Morris, H. F. Brimson, "A Study of Damage Zones or Characteristic Lengths Related to the Fracture Behavior of Graphite/Epoxy Laminates," Virginia Polytechnic Institute and State University, VPI-E-77-15, 1977.

48. R. B. Pipes, J. W. Gillespie, Jr., and R. C. Wetherhold, "Superposition of the Notched Strength of Composite Laminates," Polymer Engineering and Science, Vol. 19, No. 16, 1979, pp. 1151-1155.

49. J. W. Mar and K. Y. Lin, "Fracture Mechanics Correlation for Tensile Failure of Filamentary Composites with Holes," J. of Aircraft, Vol. 14, No. 7, July 1977, pp. 703-704.

50. J. W. Mar, "Fracture and Fatigue of B-Materials," Mechanics of Composite Review, Air Force Materials Laboratory, Dayton, Ohio, Oct. 1976, p. 117.

51. J. W. Mar and K. Y. Lin, "Fracture of Boron/Aluminum Composites with Discontinuities," J. Composite Materials, Vol. 11, 1977, pp. 405-421.

52. J. Awerbuch, "Notch Sensitivity of Boron Aluminum Laminate," to be published.

53. "Measuring the Slope of Amplitude Distributions," Dunegan/Endevco Product Information Note, PIN-4, 1978.

54. J. Kaiser, "Undersuchungen Uber das Auftreten von Gerauschen beim Zugversuch," Dr.-Ing. Thesis, Technische Hochschule, Munich, 1950.

55. J. Awerbuch and H. T. Hahn, "Off Axis Fatigue of Graphite/Epoxy Composites", to be published in the ASTM-STP.

56. D. W. McCall, D. C. Douglass and E. W. Anderson, J. Polymer Sciences, Vol. 59, 1962, p. 301.

57. V. J. McBrierty, Polymer, Vol. 15, 1974, p. 503.

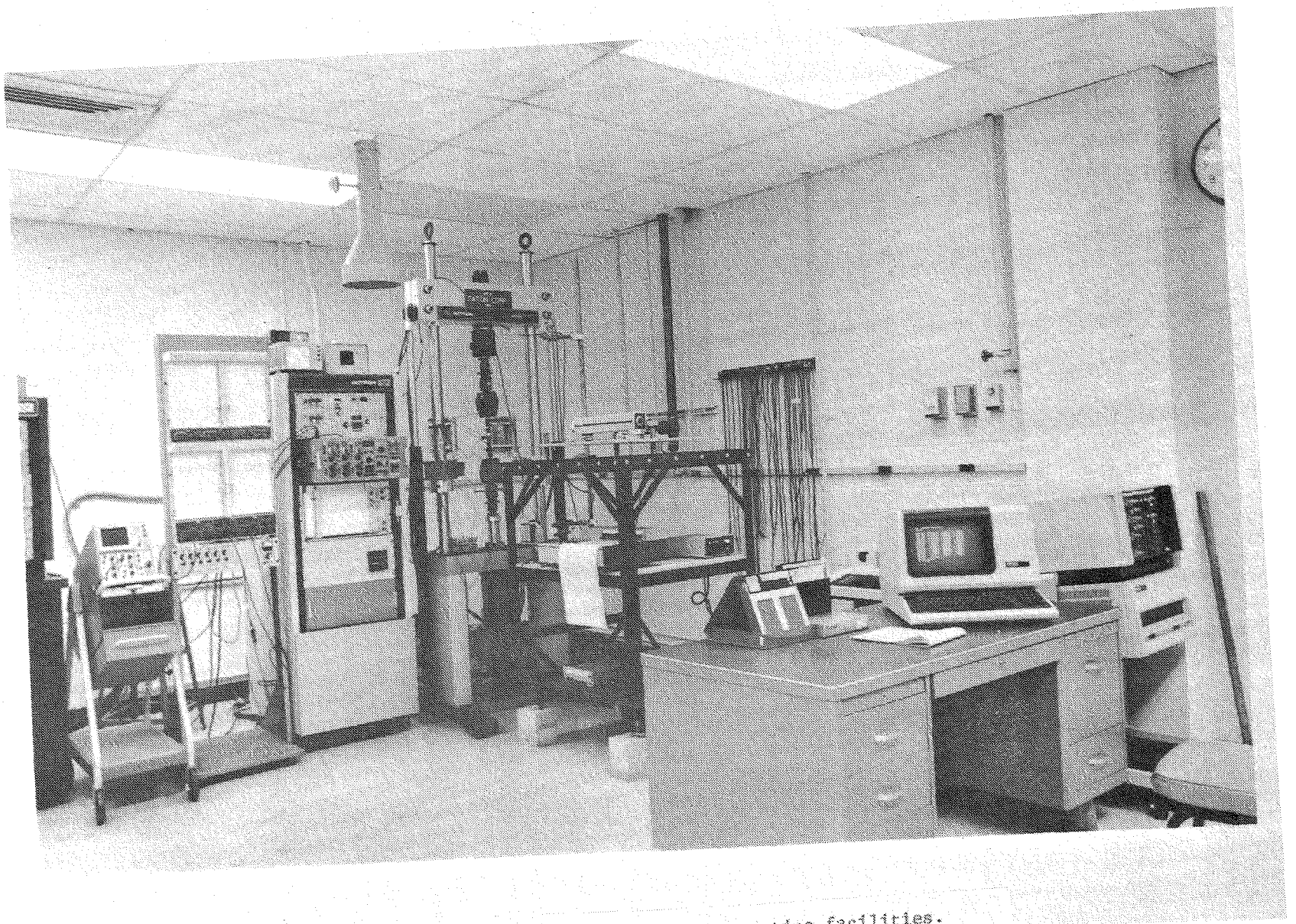

Figure 1. A general view of the testing facilities.

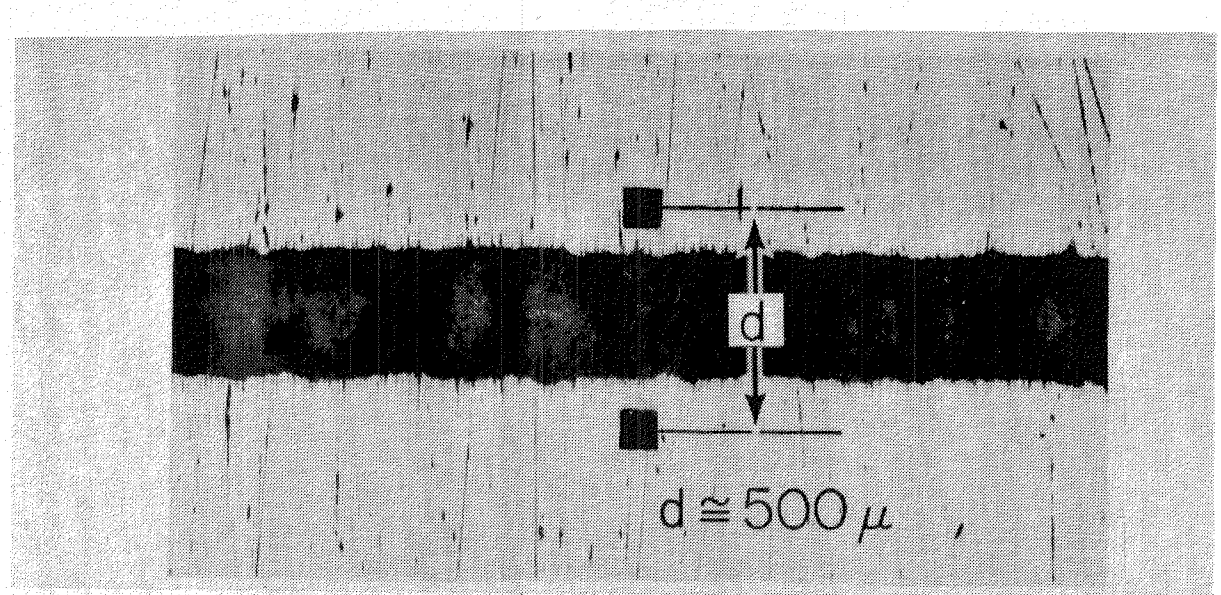

Figure 2. Photomicrograph of two indentations located at the center of the crack.

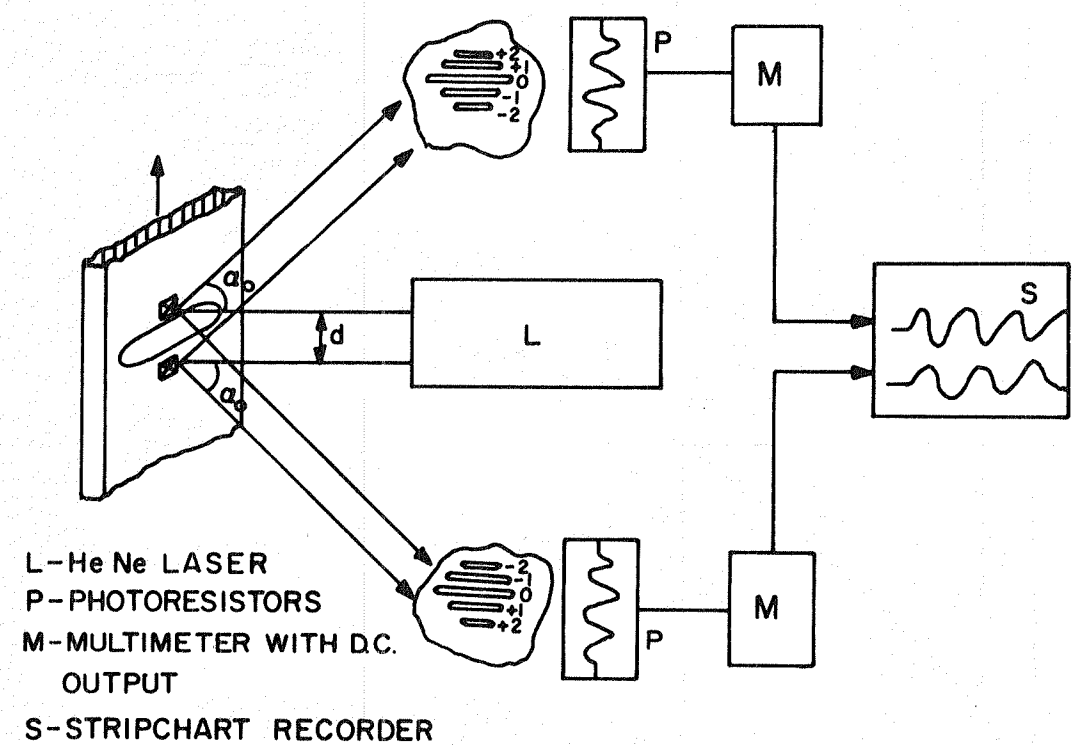

Figure 3. Schematic view of the laser interferometry displacement technique. Nominal value of d is 0.5 mm and α_o is typically 42°.

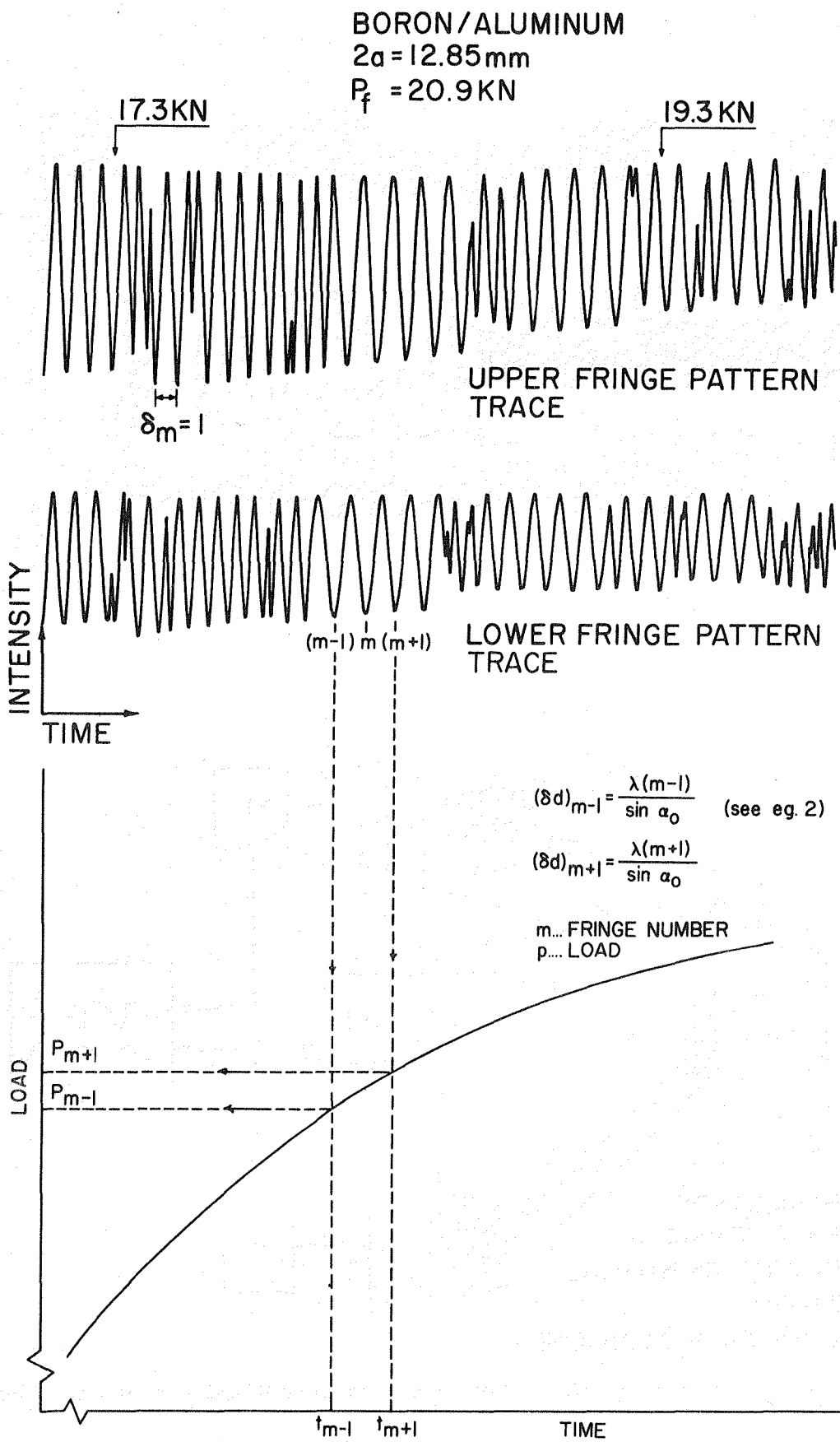

Figure 4. A schematic view of data reduction from the IDG records.

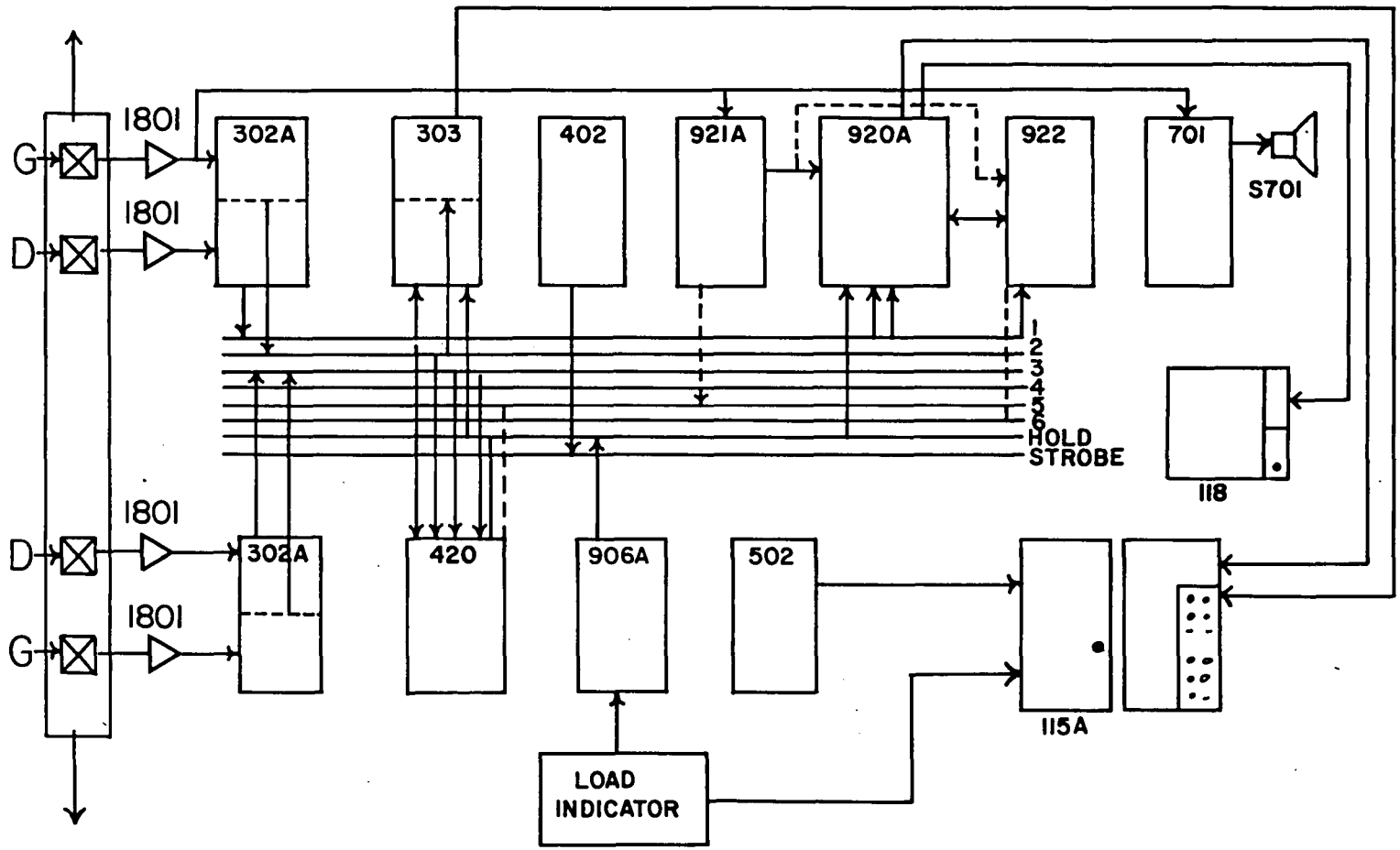

Figure 5a. Block diagram of the Dunegan/Endevco 3000 acoustic emission system.

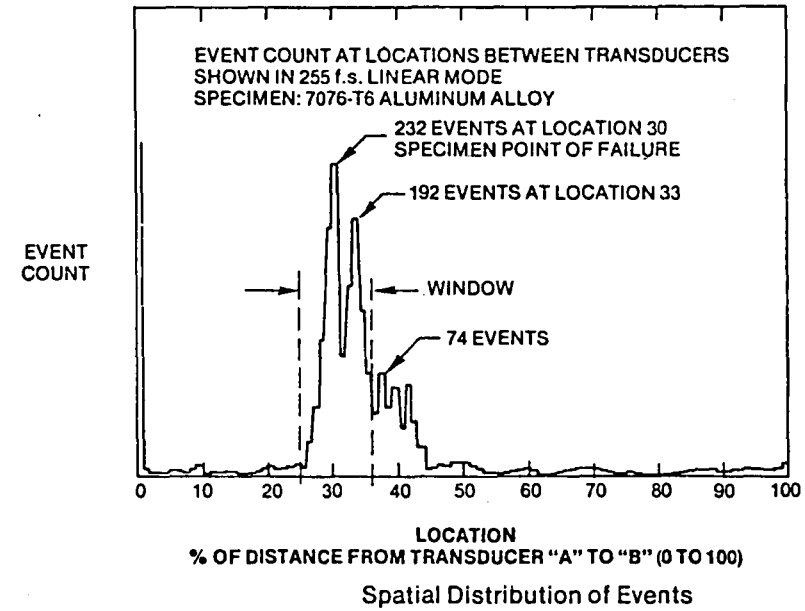

Spatial Distribution of Events

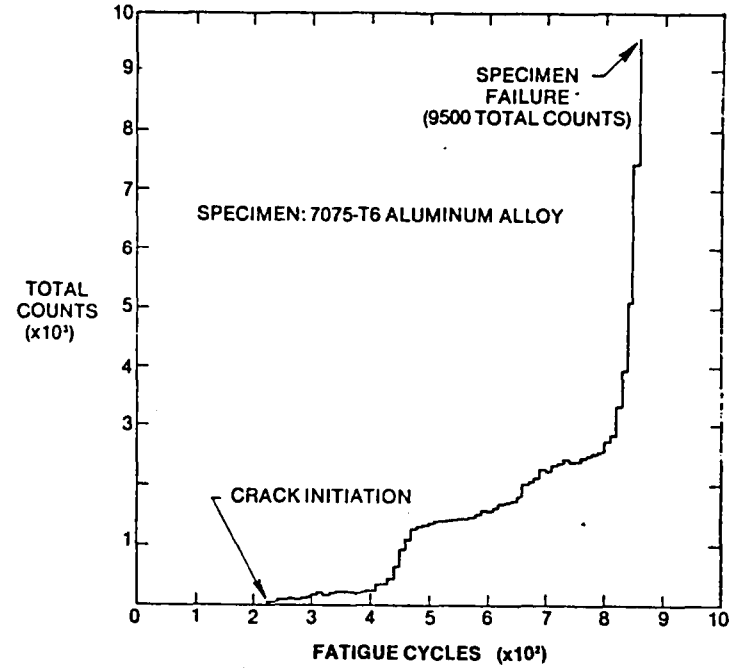

Total Counts as a Function of Fatigue Cycles

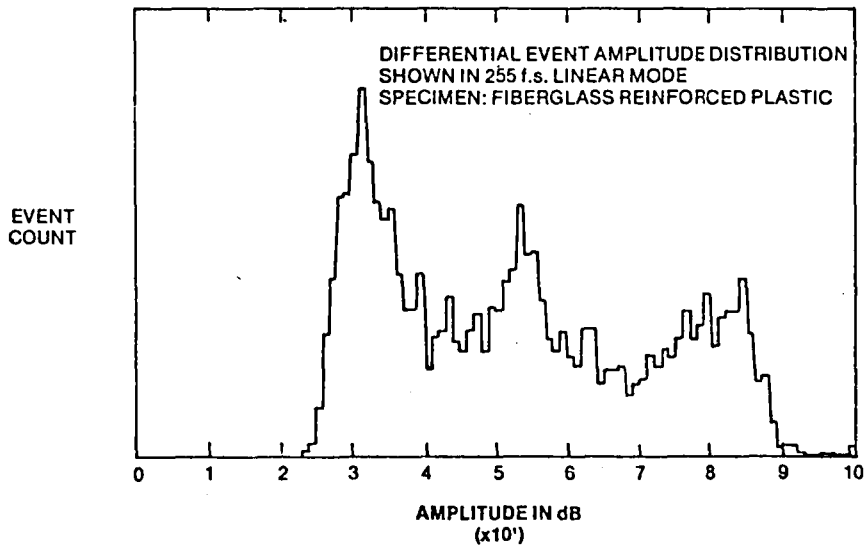

Amplitude Distribution

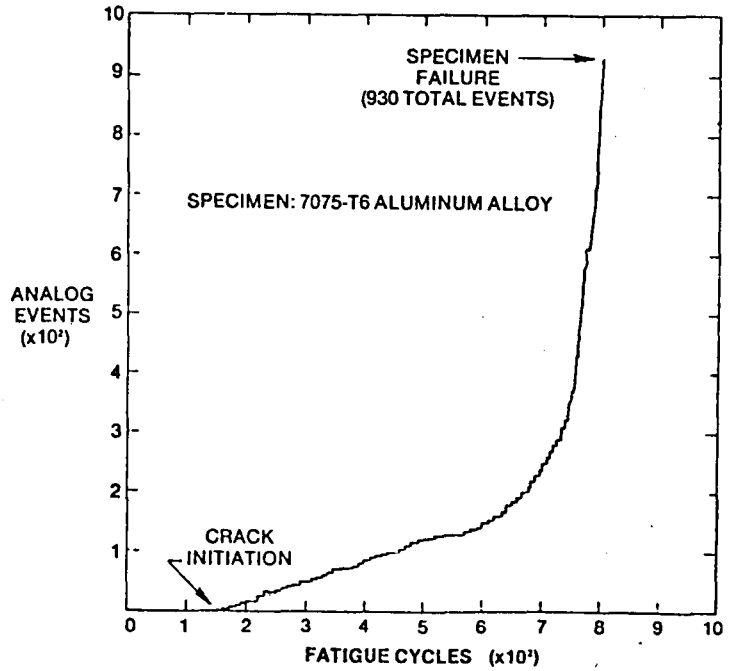

Analog Events as a Function of Fatigue Cycles

Figure 5b. Schematics of location and amplitude distribution histograms and accumulative counts and events diagrams [920A Manual].

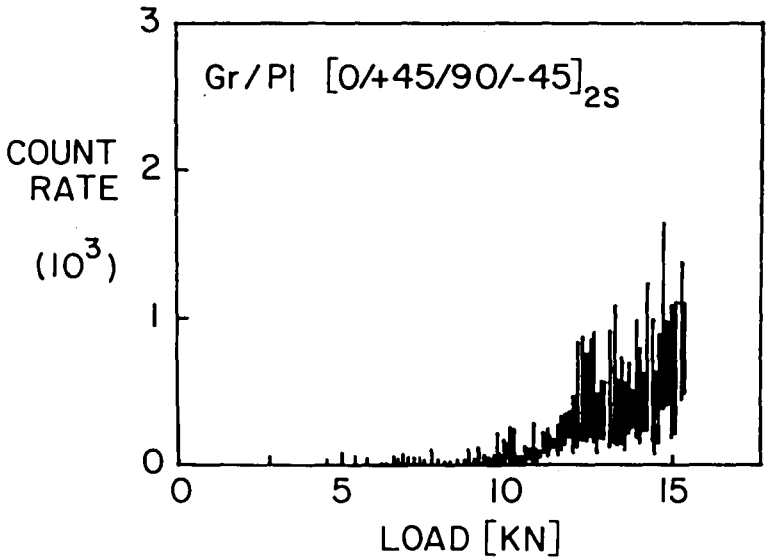

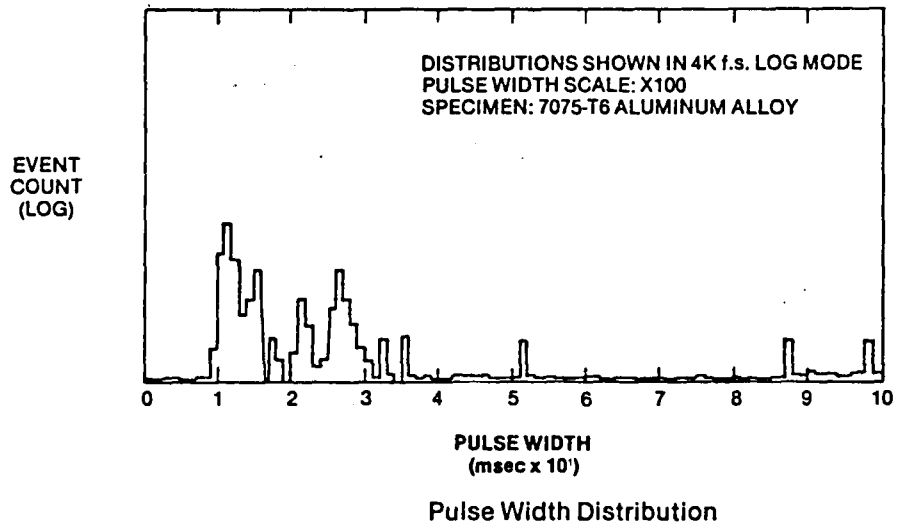

Pulse Width Distribution

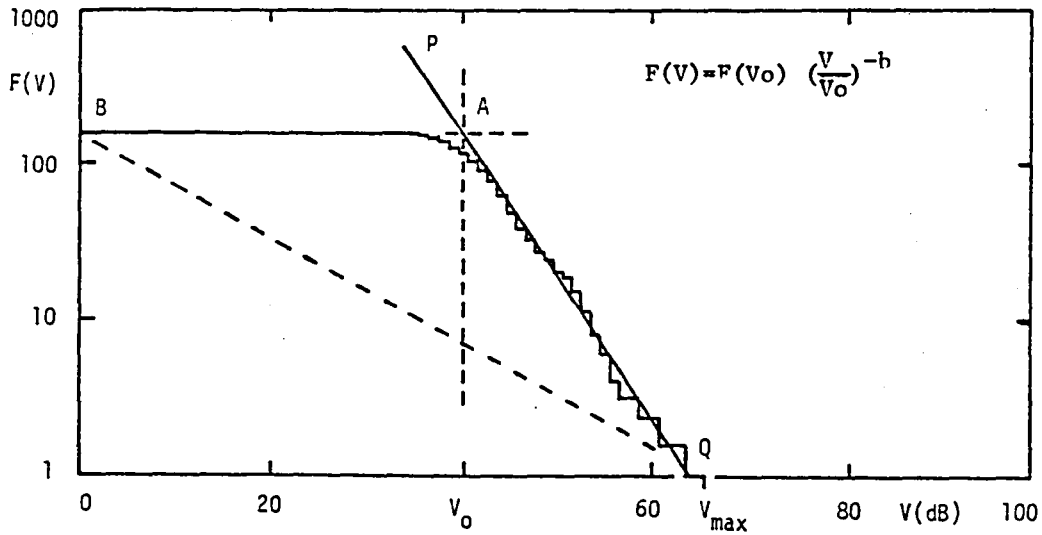

Cumulative Event Amplitude Distribution

Figure 5c. Schematics of pulse width distribution histograms, count rate and Cumulative Event Amplitude Distribution (CEAD) diagrams [920A Manual].

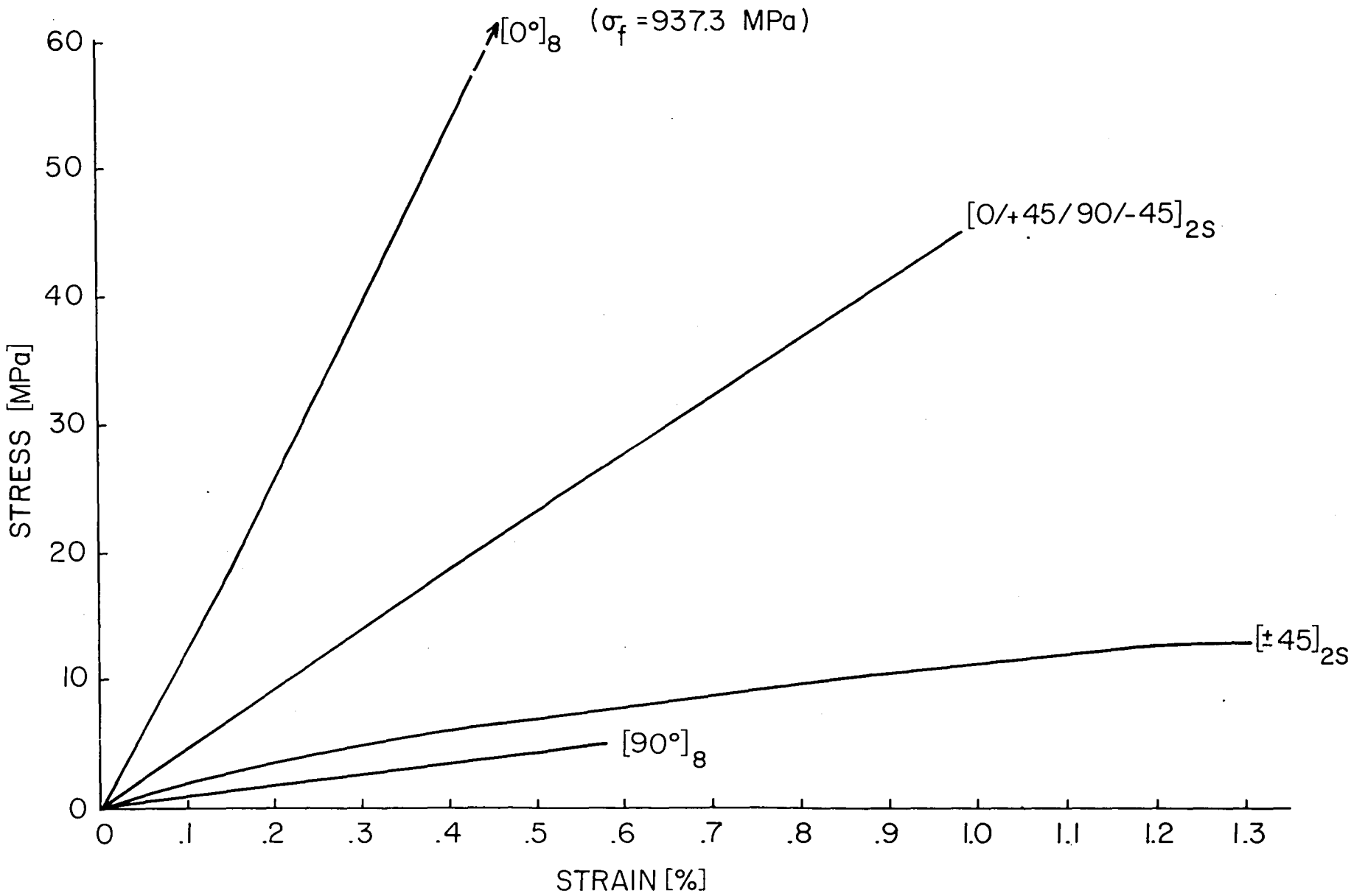

Figure 6. Stress-strain curves for all four graphite/polyimide laminates.

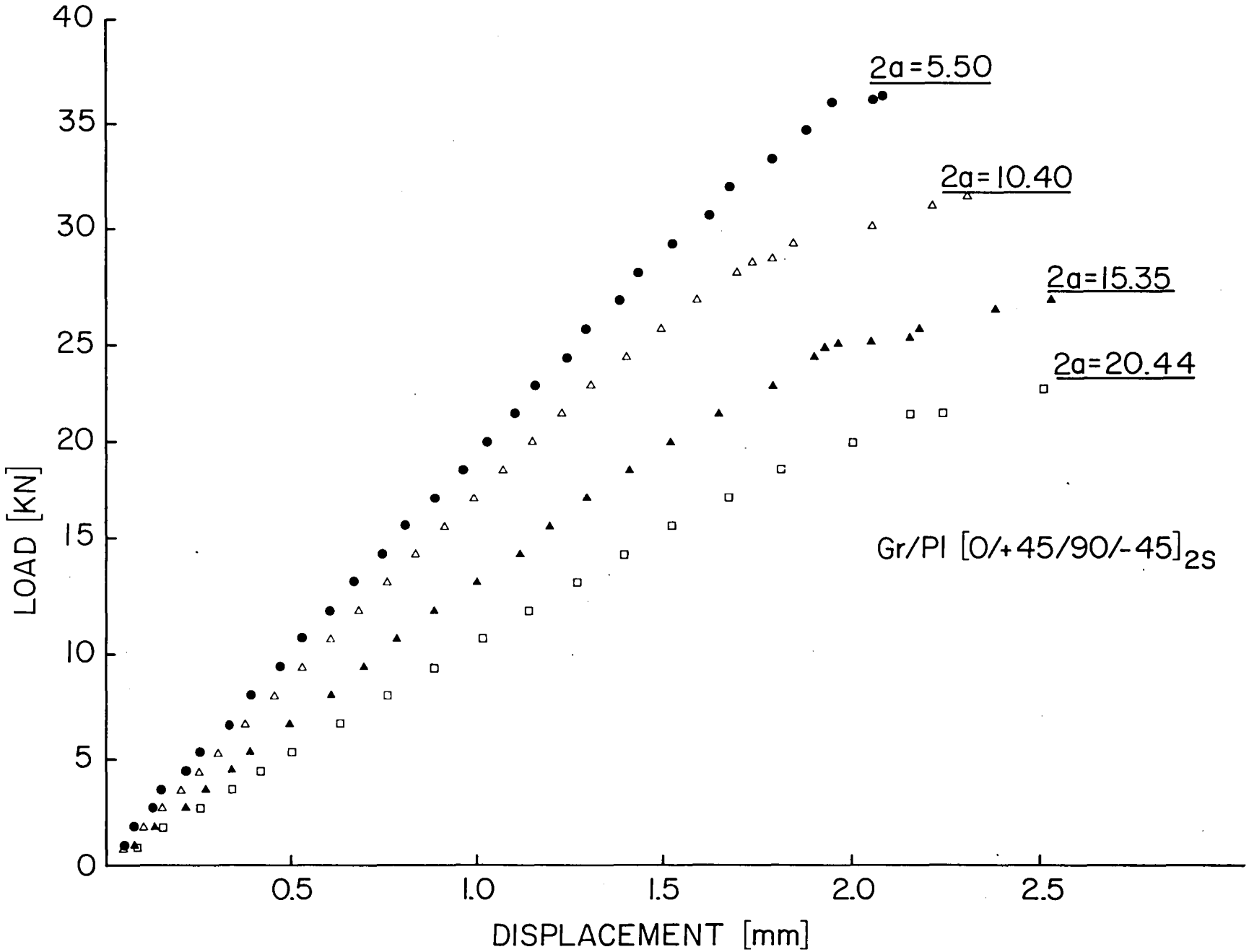

Figure 7. Far-field load-displacement curves for Gr/PI $[0/+45/90/-45]_{2s}$ laminate for various crack lengths obtained with the compliance gage.

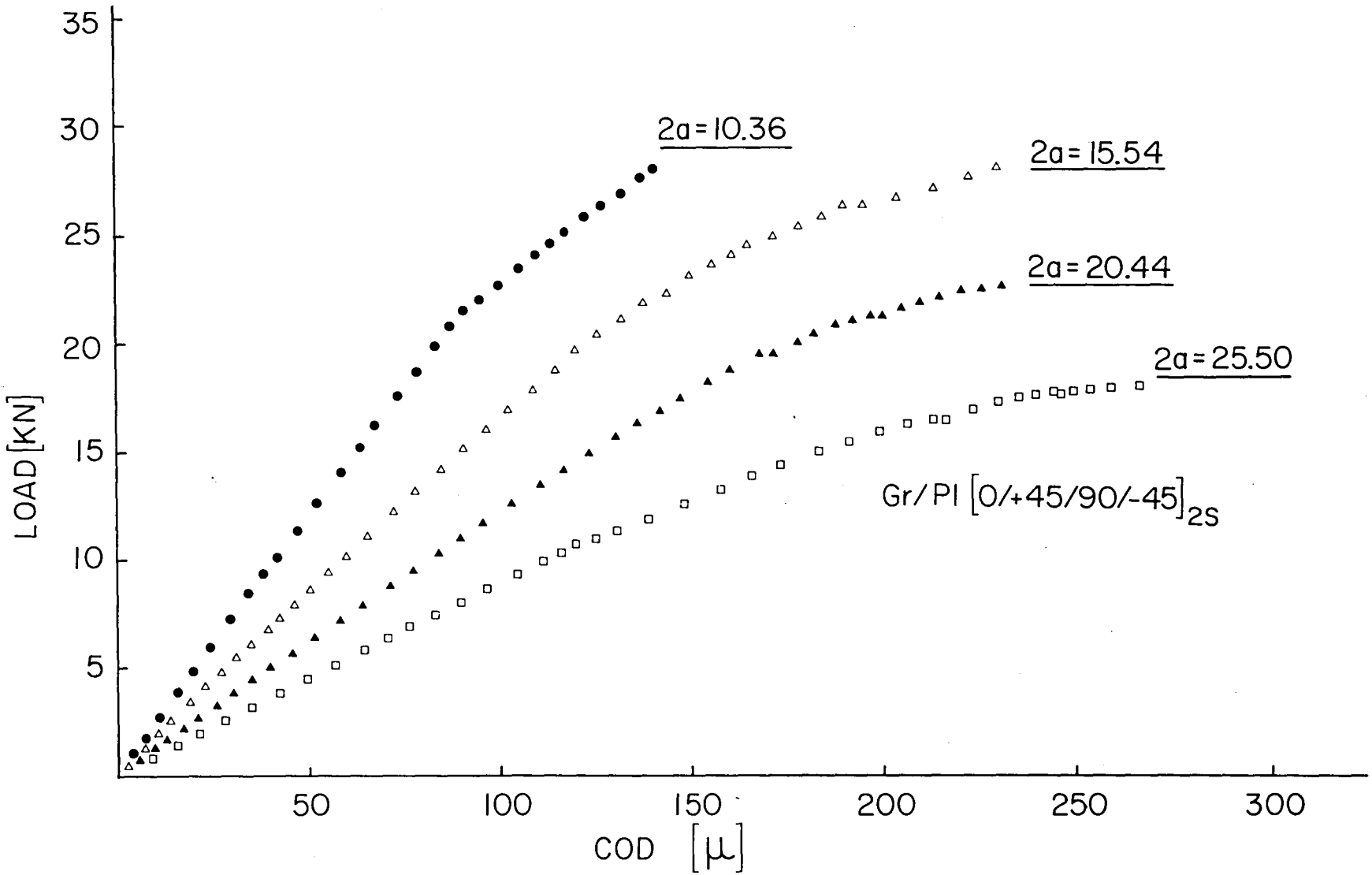

Figure 8. Load-COD curves for Gr/PI $[0/+45/90/-45]_{2s}$ laminate for various crack lengths obtained with the IDG.

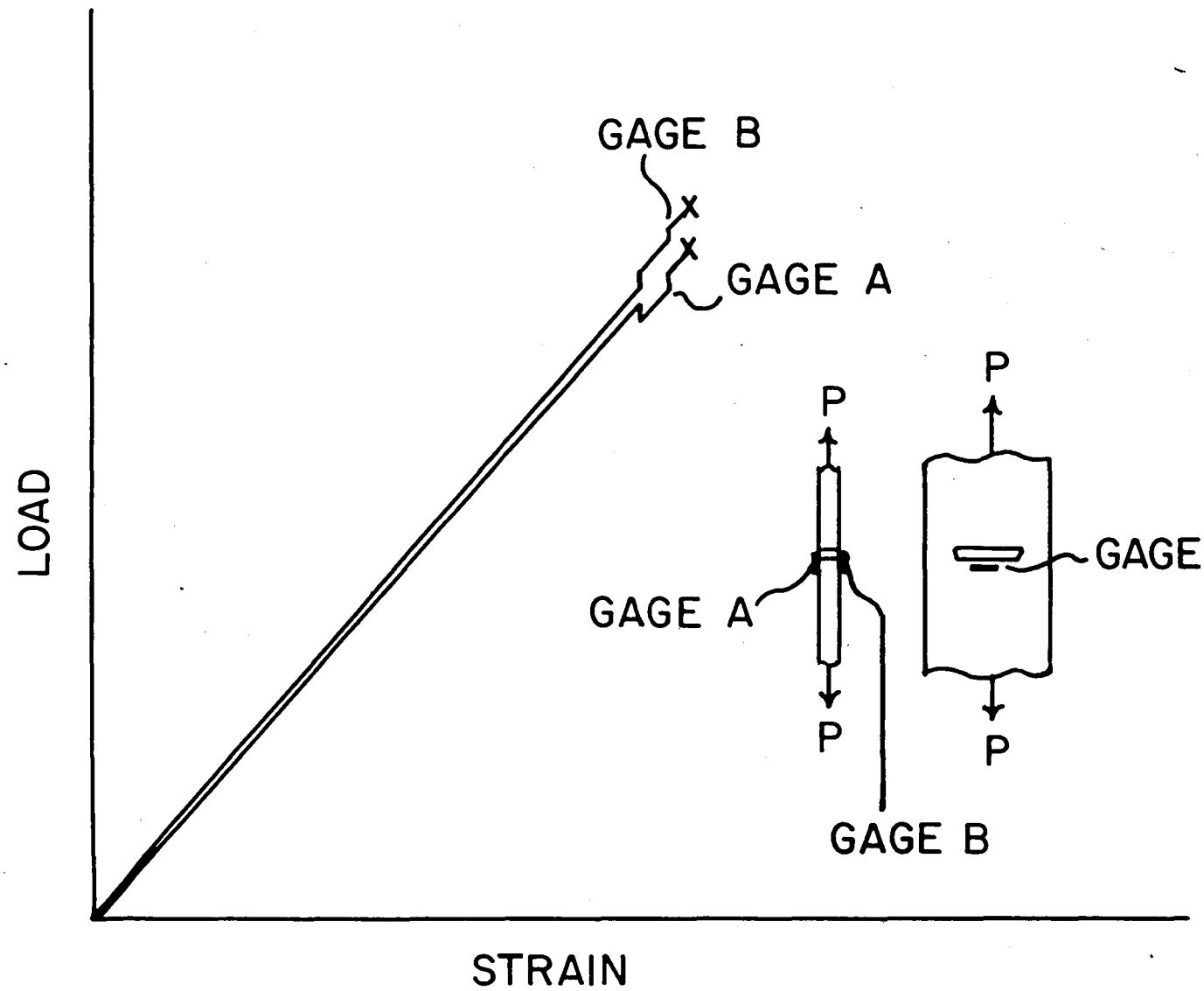

Figure 9. Schematics of transverse strain records at the crack edges.

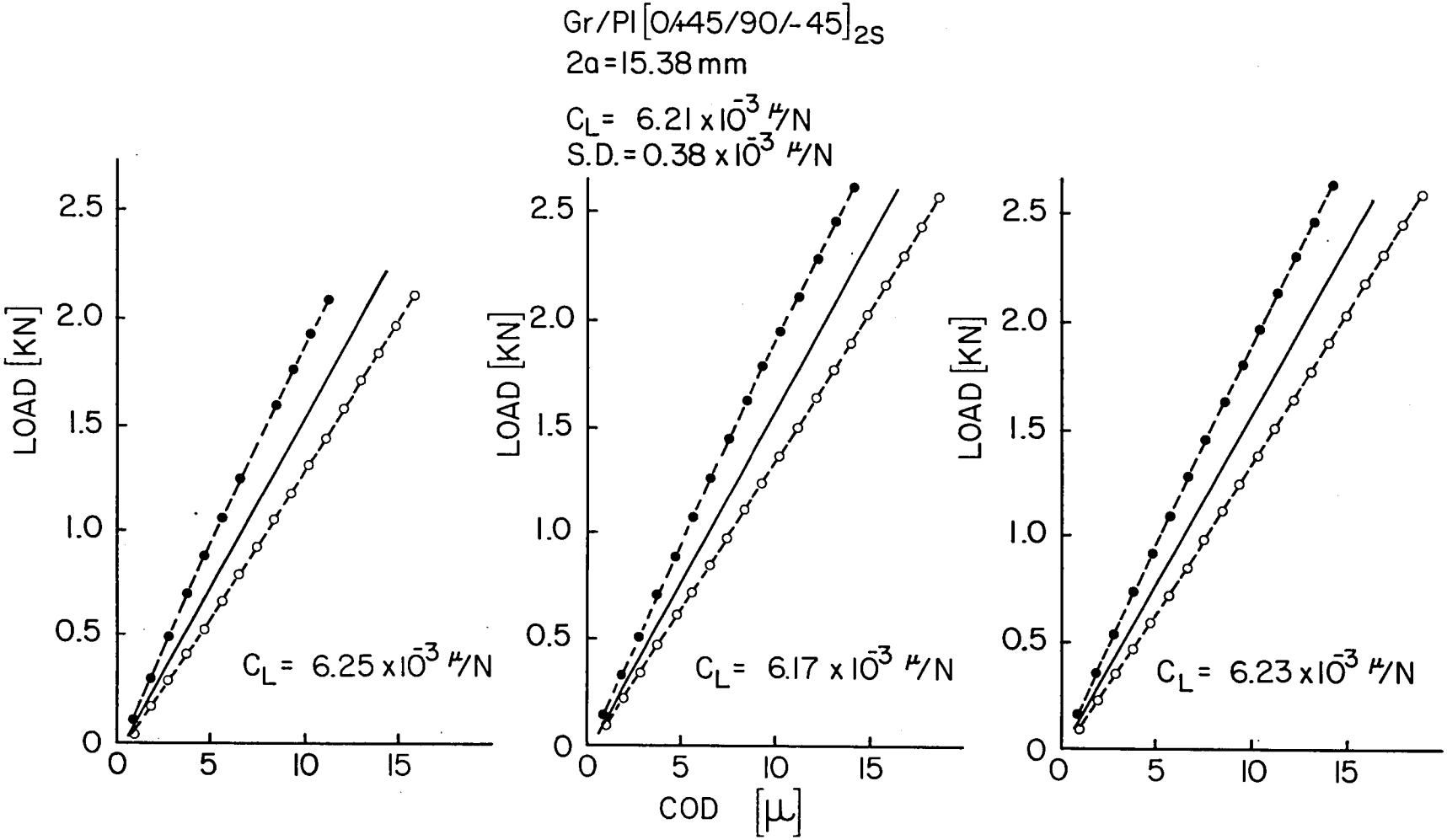

Figure 10. Example of three load-COD curves at initial loading for Gr/PI $[0/+45/90/-45]_{2s}$ laminate.

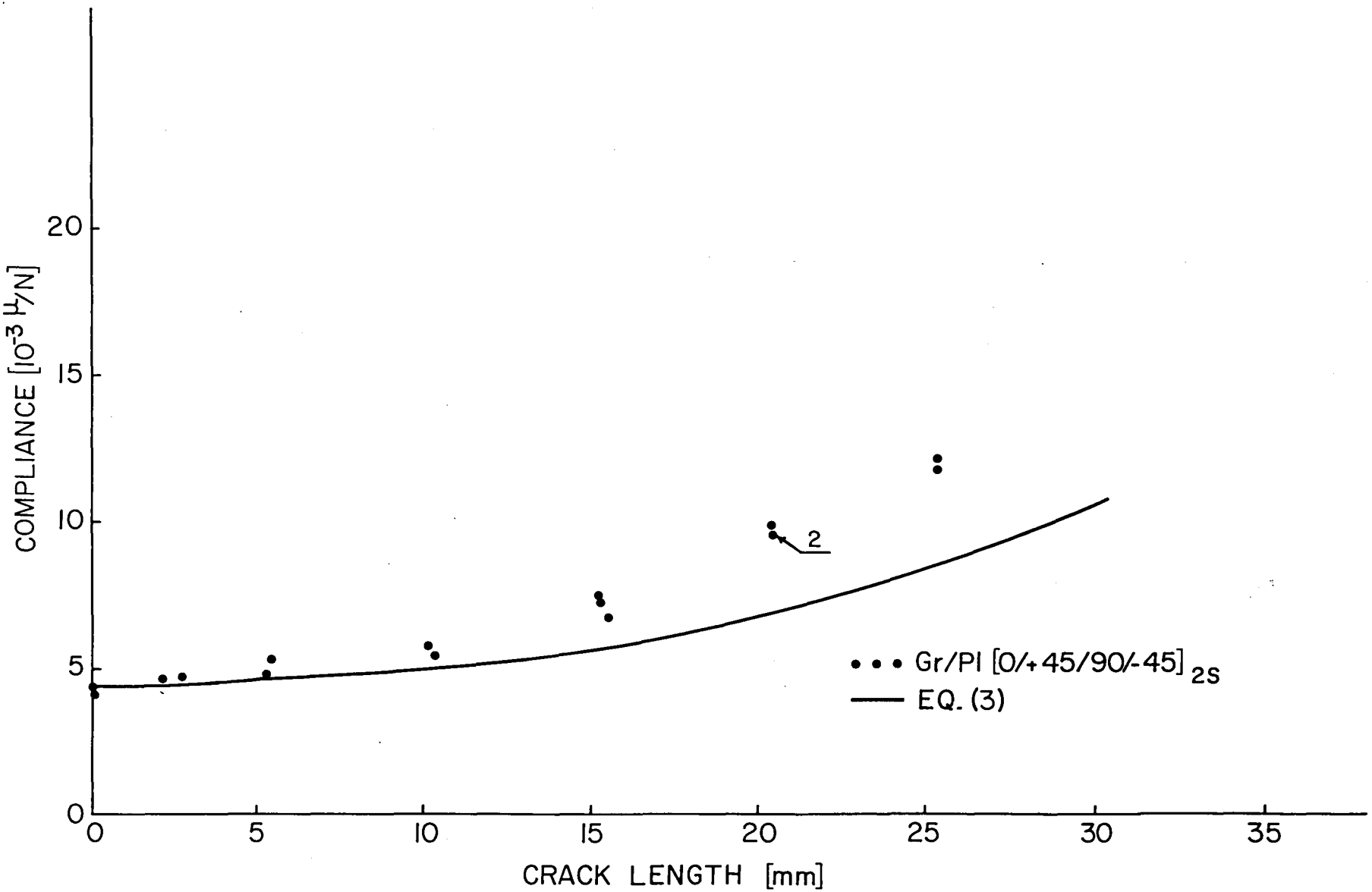

Figure 11. Global compliance vs. crack length for Gr/PI $[0/+45/90/-45]_{2s}$ laminate.

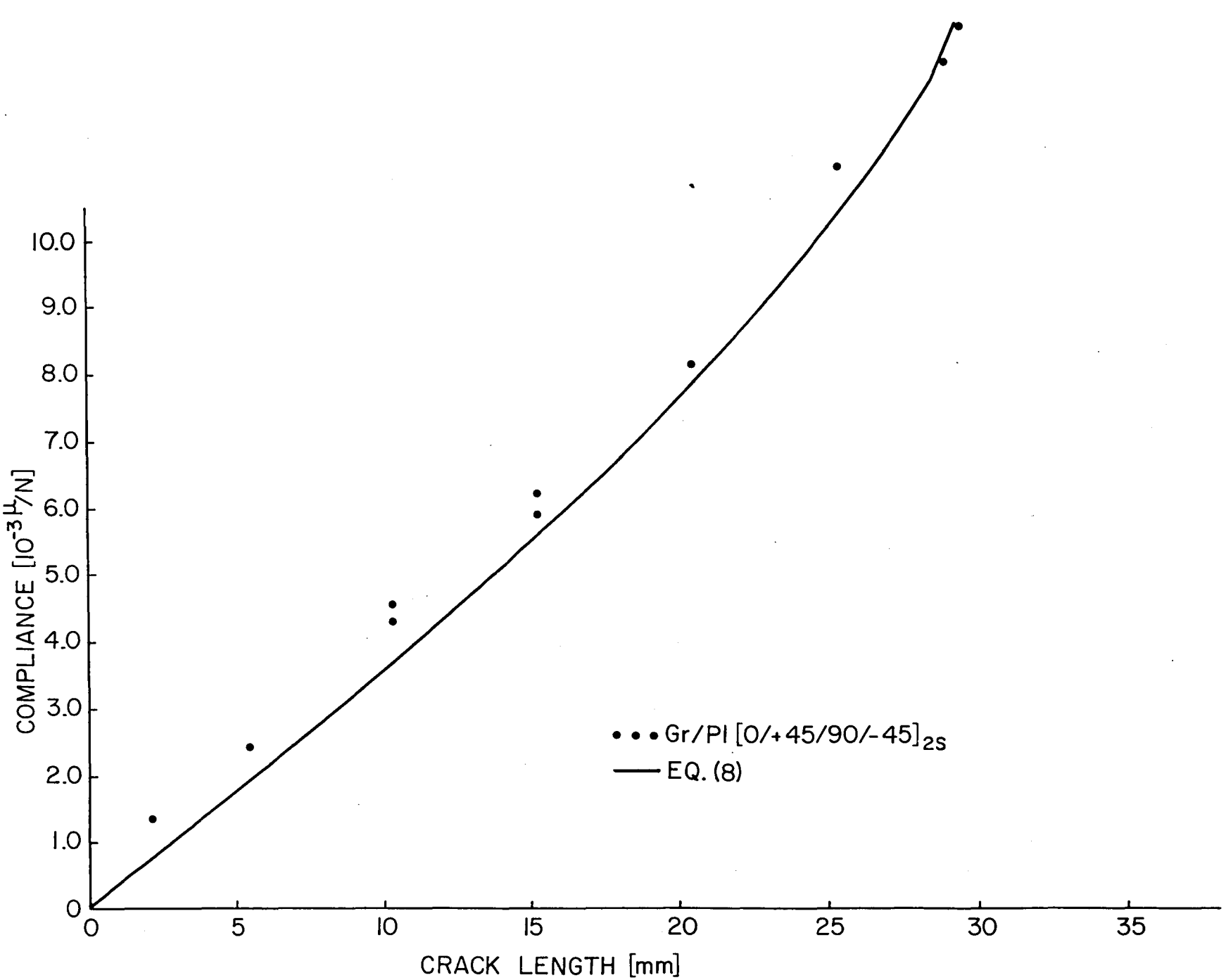

Figure 12. Local compliance vs. crack length for Gr/PI [0/+45/90/-45]$_{2s}$ laminate.

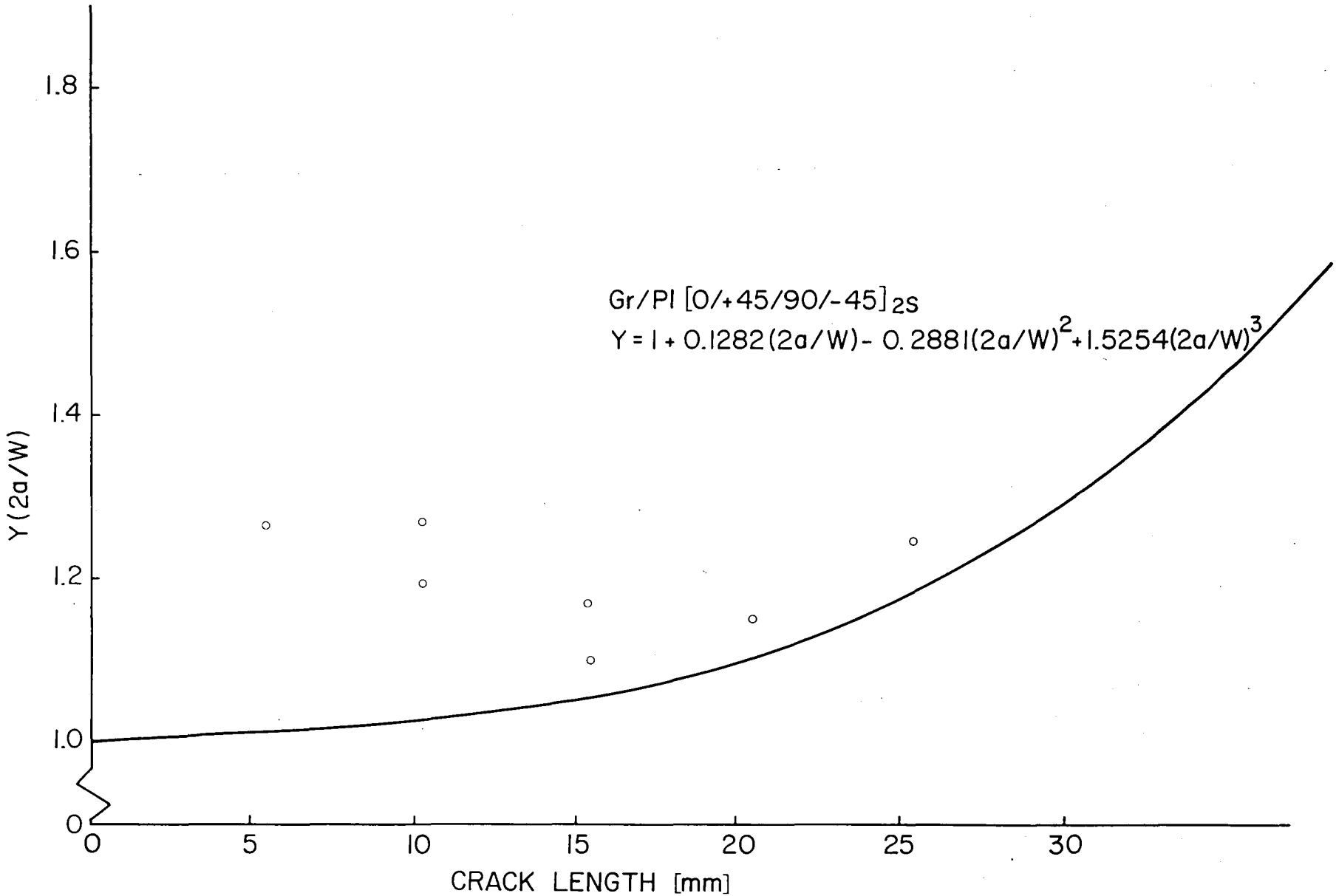

Figure 13. Comparison of experimental K-calibration factors with theoretical isotropic curve for Gr/PI $[0/+45/90/-45]_{2s}$ laminate.

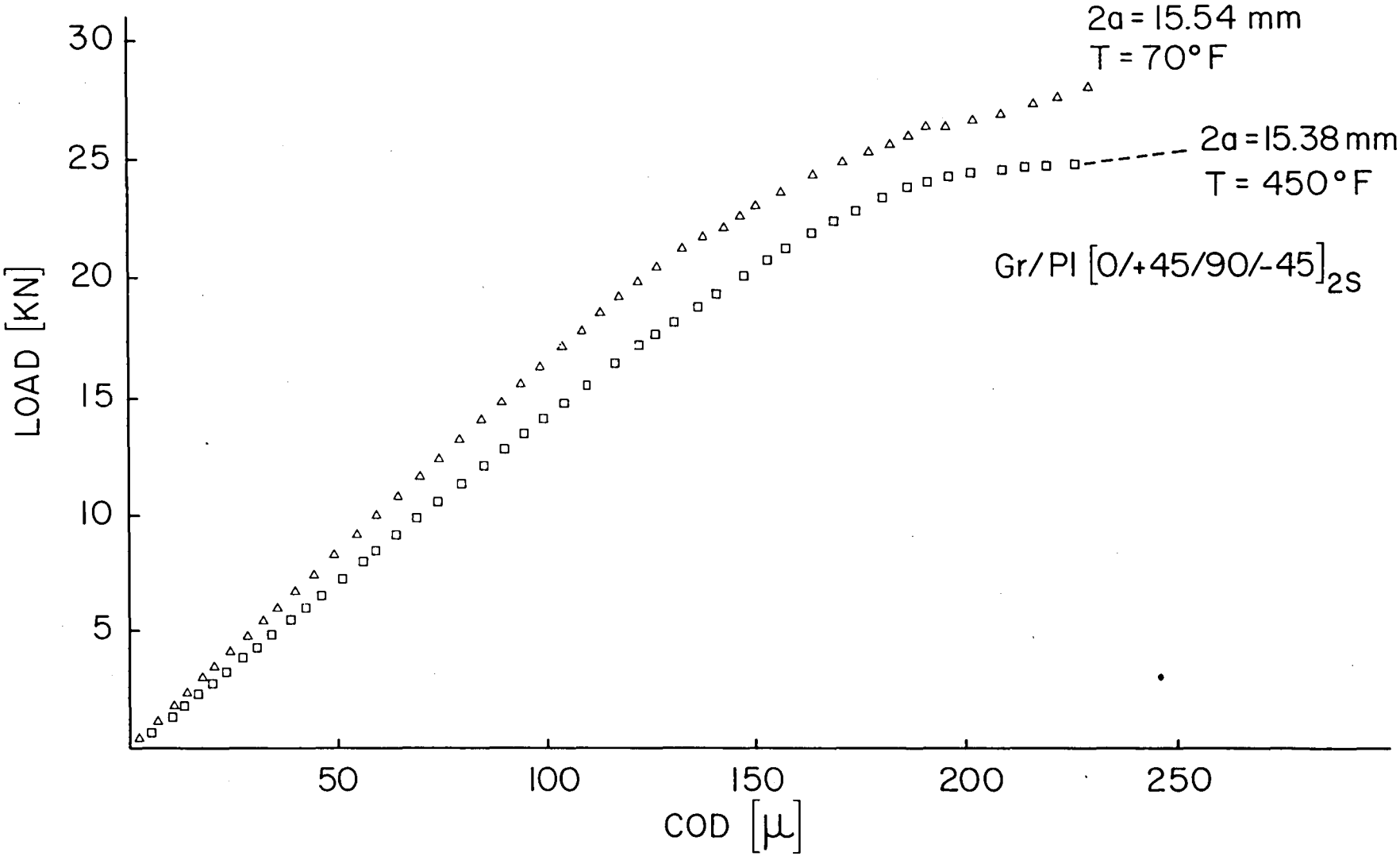

Figure 14. Load-COD curves for Gr/PI $[0/+45/90/-45]_{2s}$ laminate at 70°F and at 450°F, obtained with the IDG.

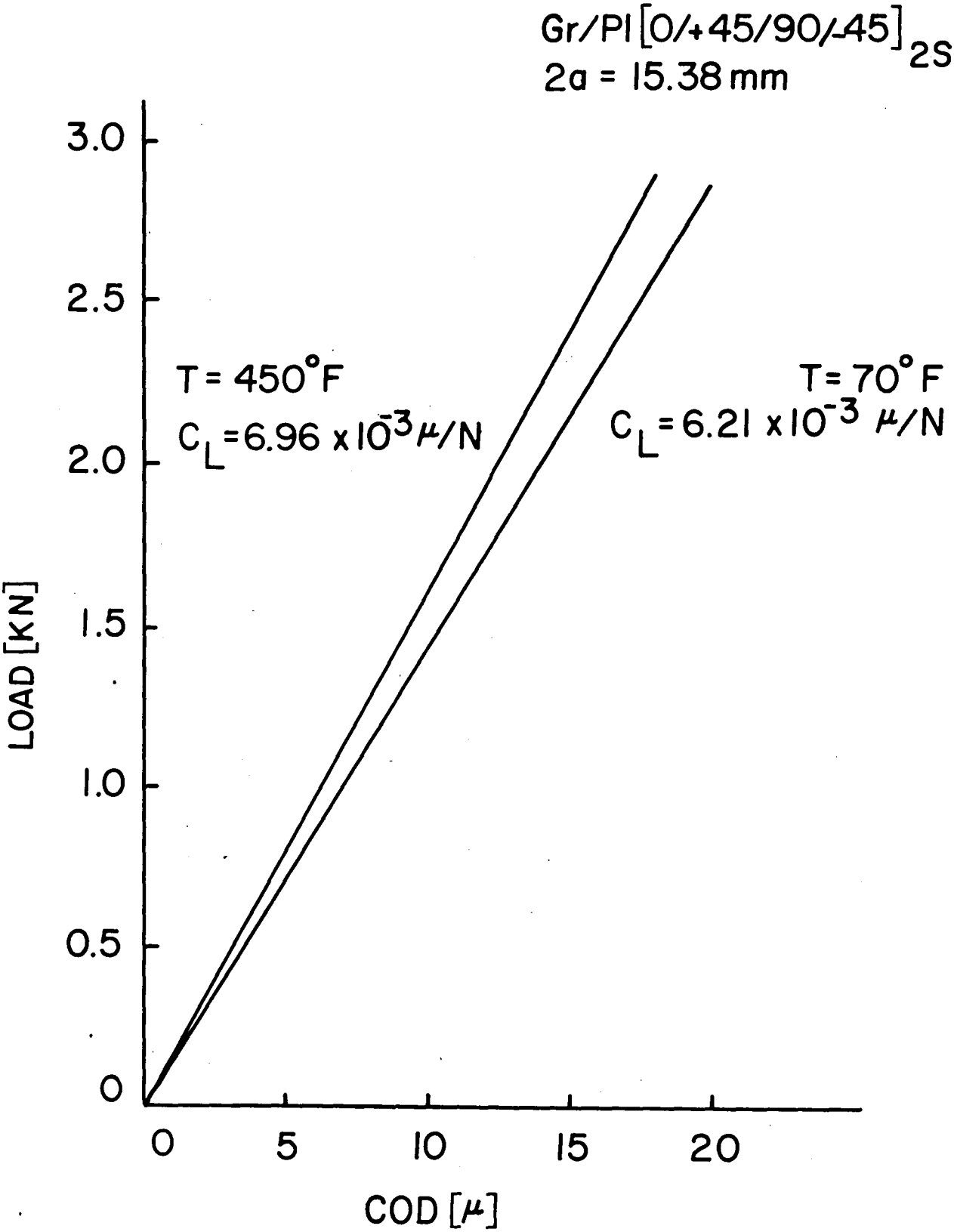

Figure 15. Comparison of initial load-COD curves for Gr/PI $[0/+45/90/-45]_{2s}$ laminate at 70°F and at 450°F, obtained with the IDG.

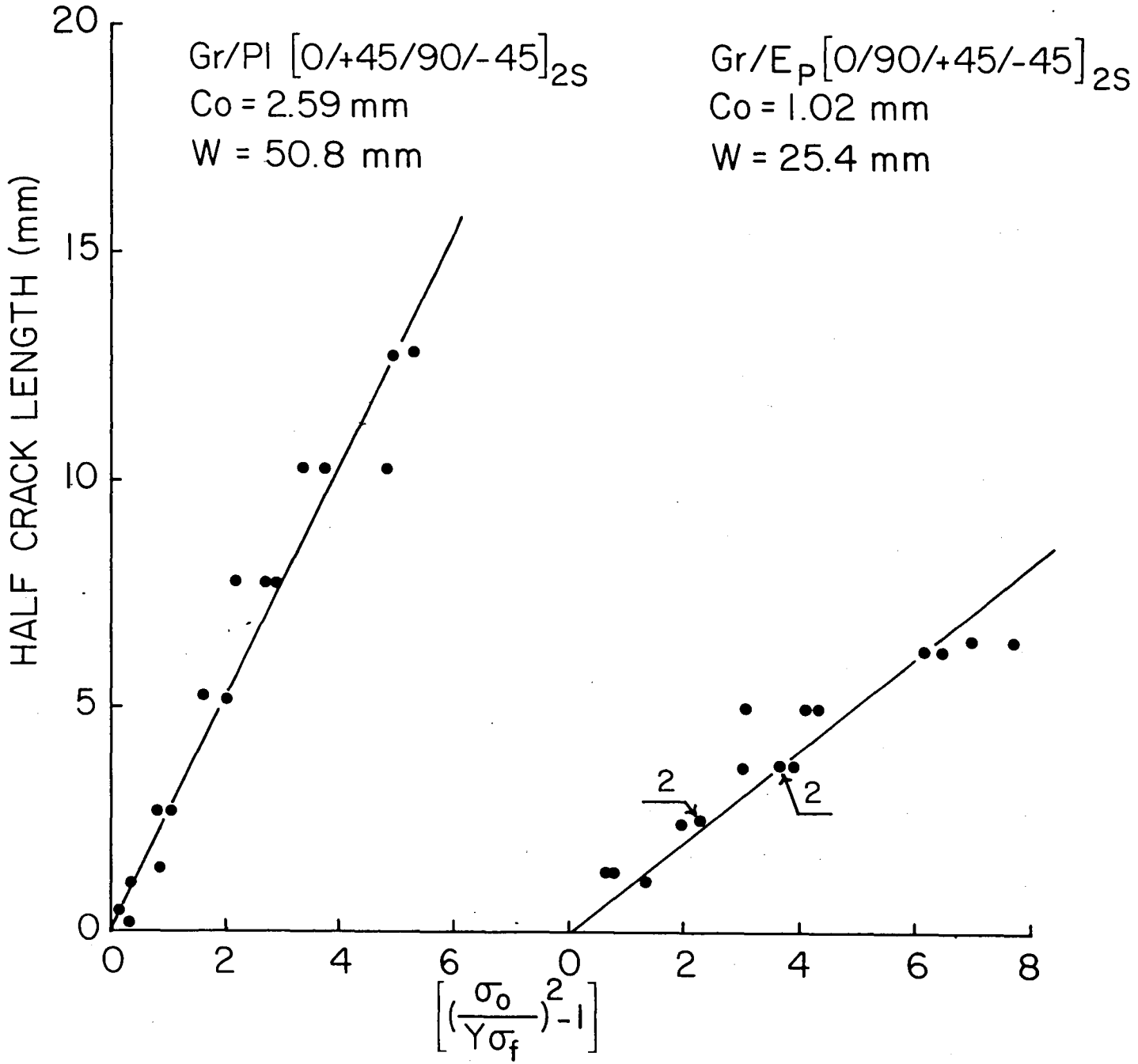

Figure 16. Least squares fit for c_o for Gr/PI $[0/+45/90/-45]_{2s}$ and Gr/Ep $[0/90/+45/-45]_{2s}$ laminates.

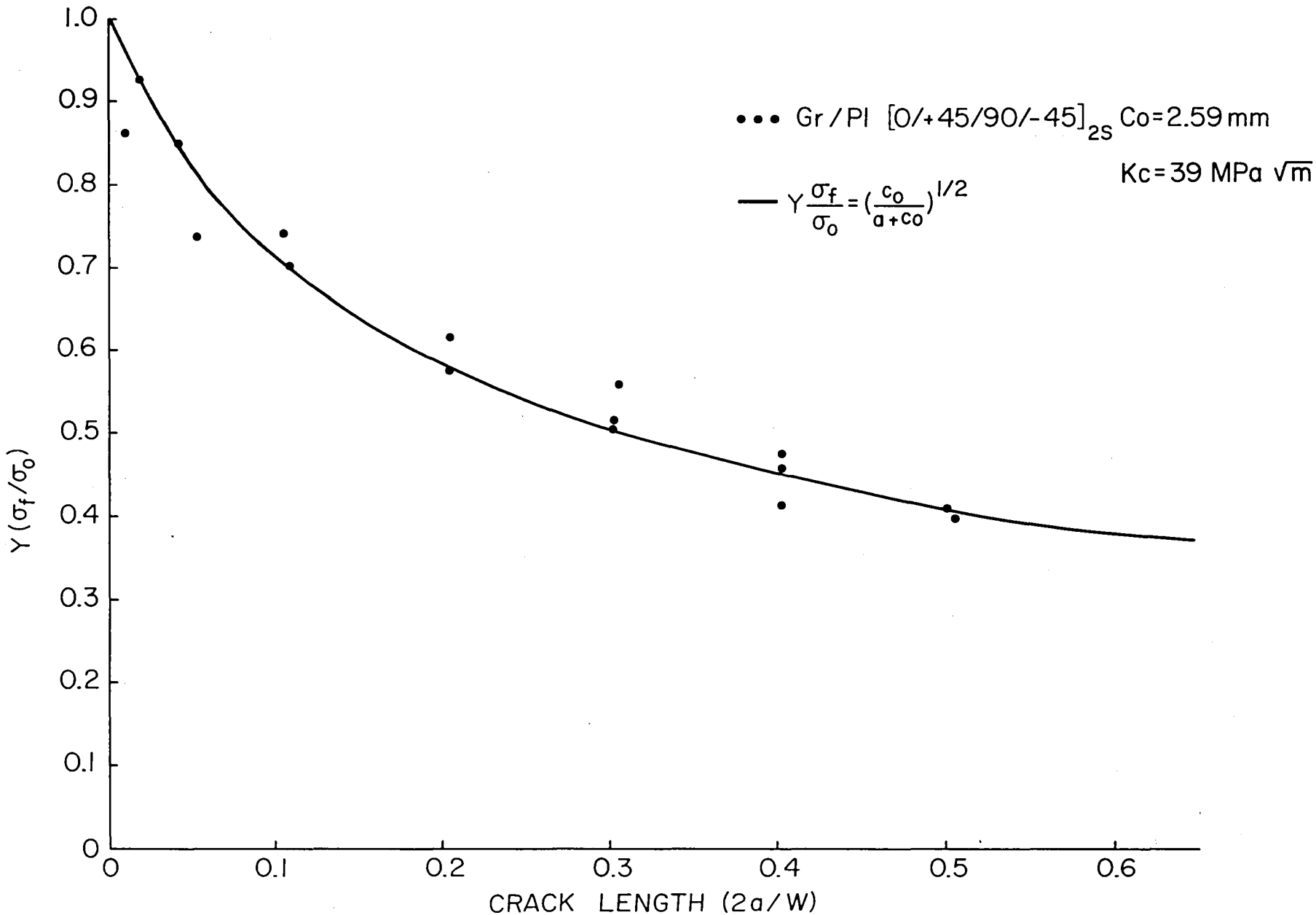

Figure 17. Comparison of analytical (WEK model) and experimental results for notched strength for Gr/PI $[0/+45/90/-45]_{2s}$ laminate.

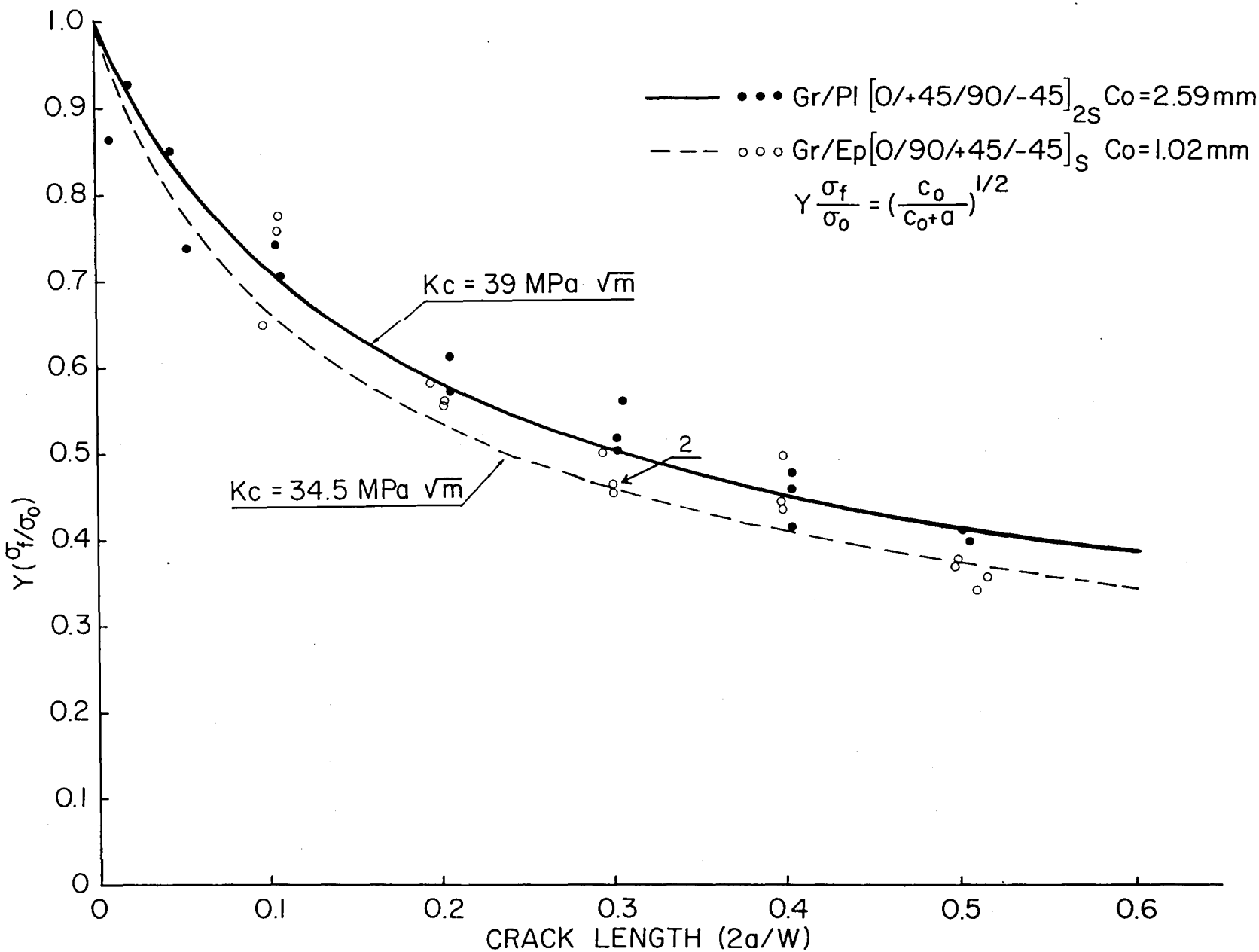

Figure 18. Comparison of notch sensitivity between Gr/PI $[0/+45/90/-45]_{2s}$ and Gr/Ep $[0/90/+45/-45]_{2s}$ laminates.

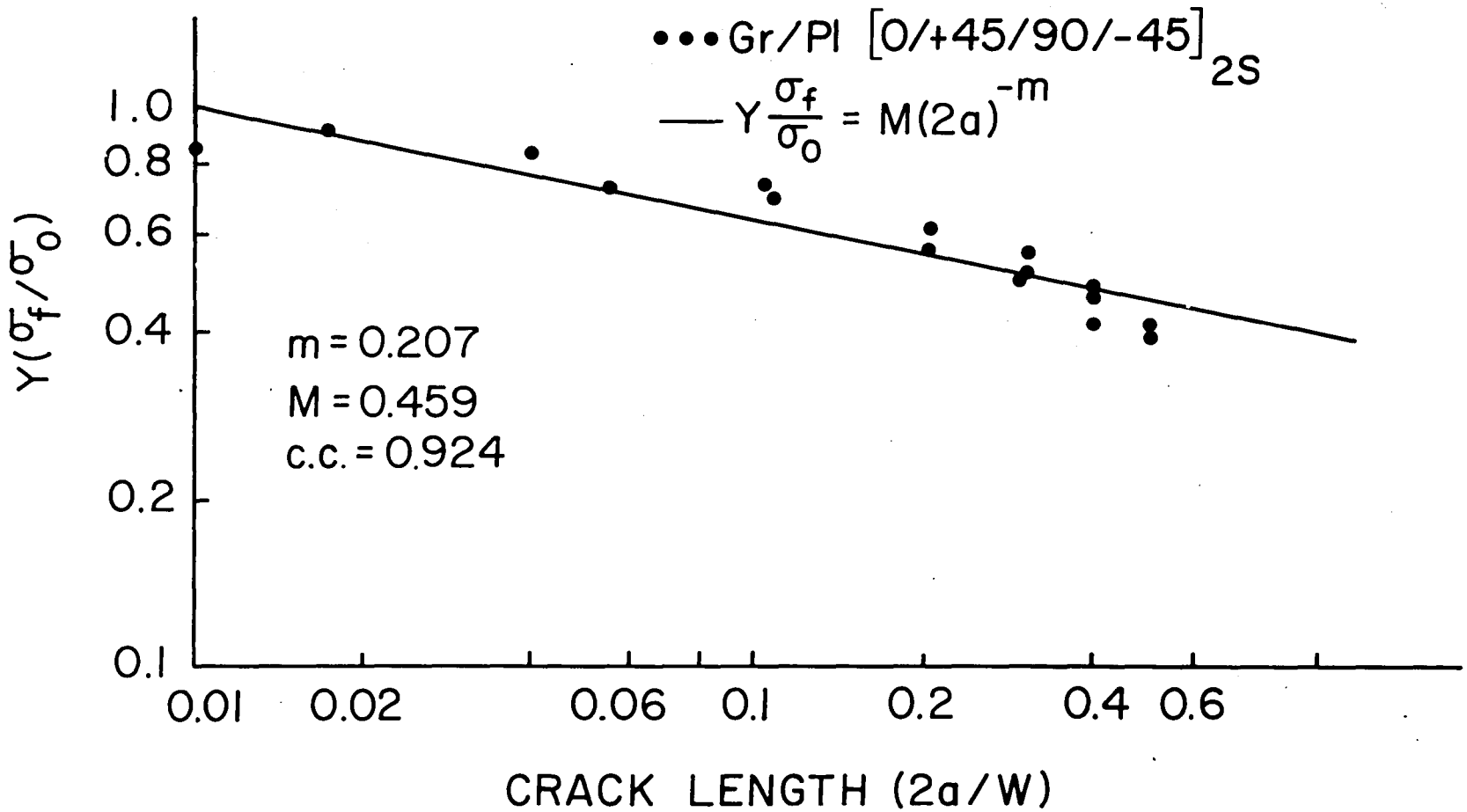

Figure 19. Notched strength versus crack length: comparison of ML model with experimental data for Gr/PI $[0/+45/90/-45]_{2s}$ laminate.

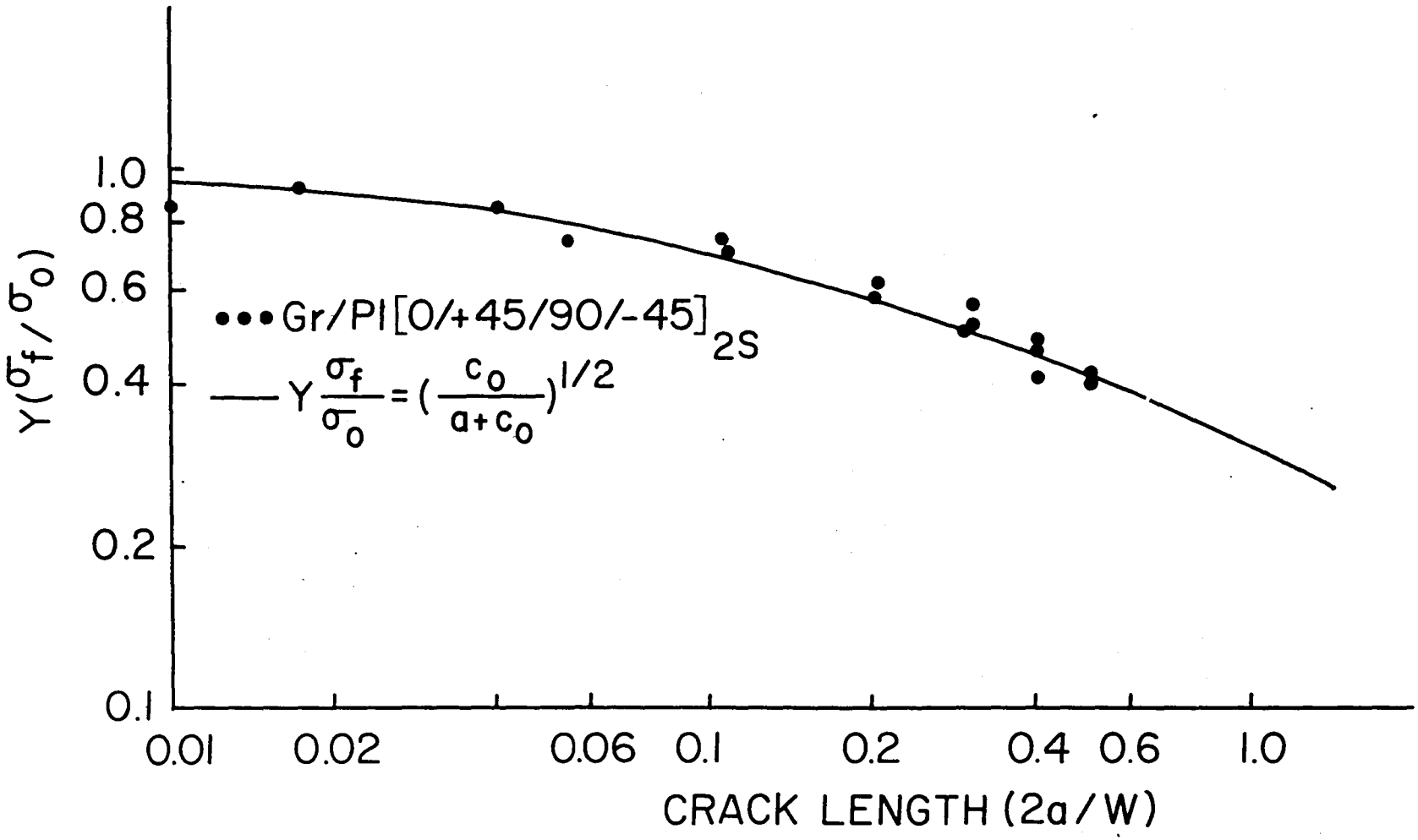

Figure 20. Notched strength versus crack length: comparison of WEK model with experimental data on logarighmic scale for Gr/PI $[0/+45/90/-45]_{2s}$ laminate.

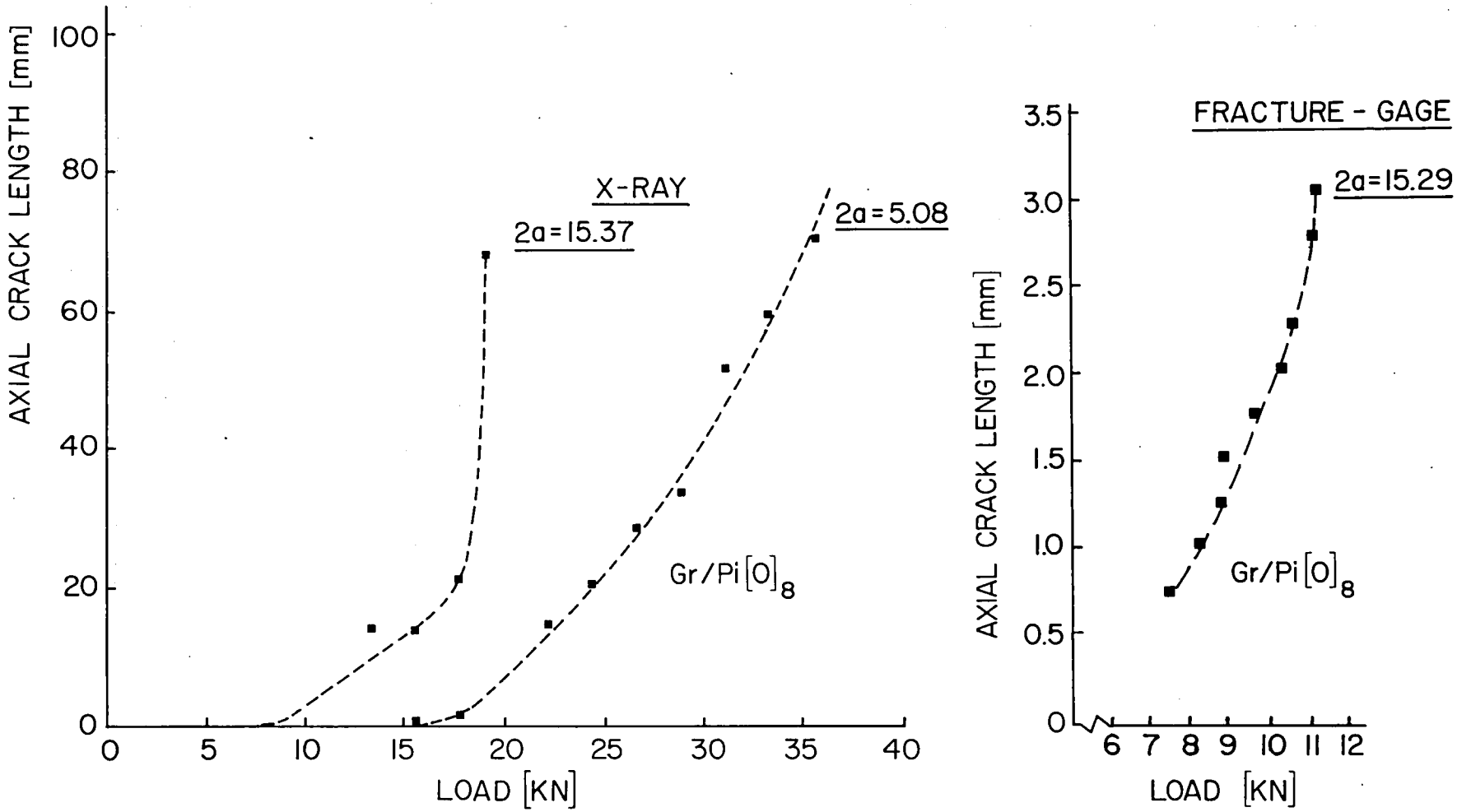

Figure 21. Experimental results on length of axial splitting versus applied load for three notched Gr/PI $[0]_8$ specimens.

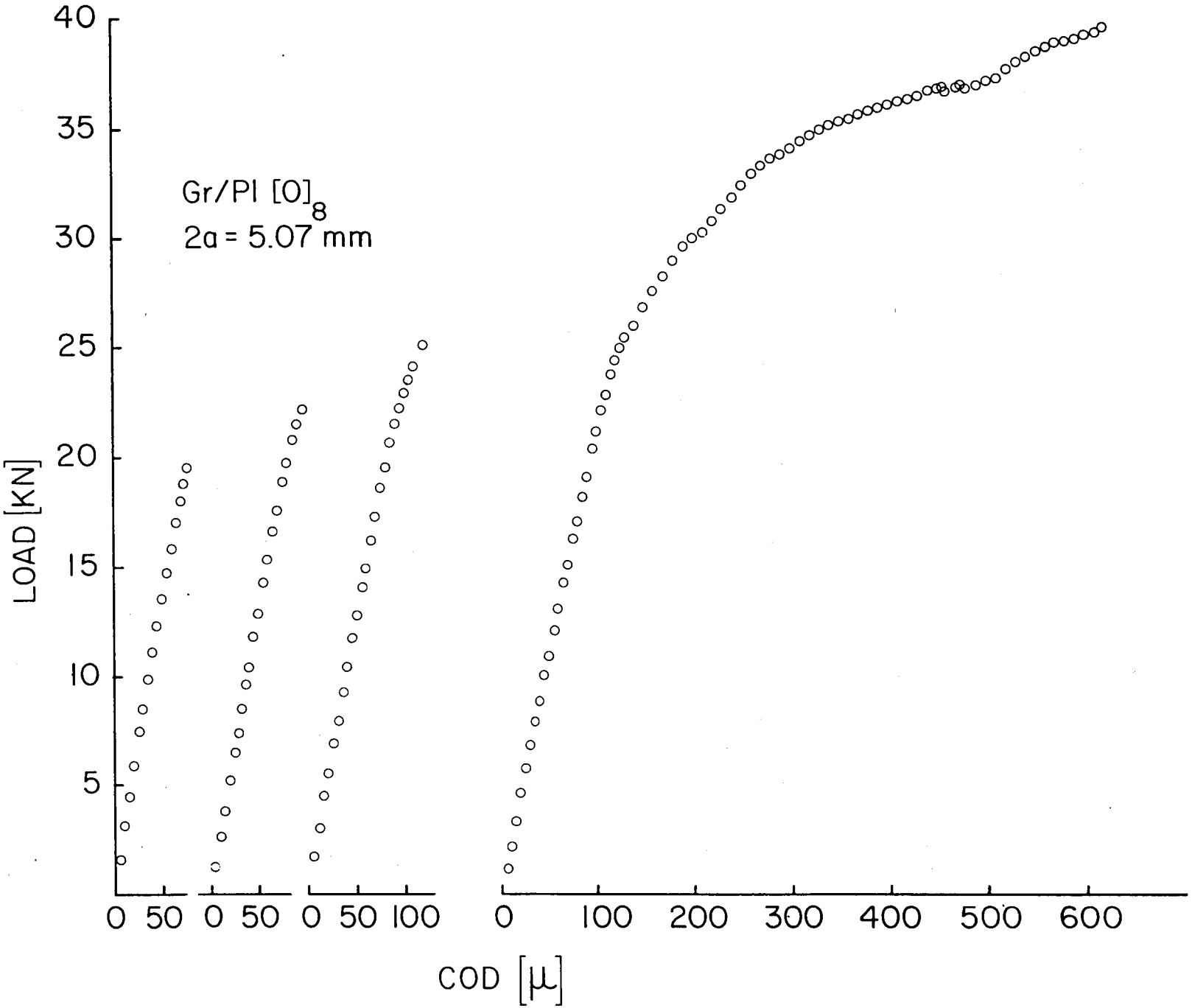

Figure 22. Load-COD curves for notched Gr/PI $[0]_8$ specimen obtained with the IDG (crack length = 15.37 mm).

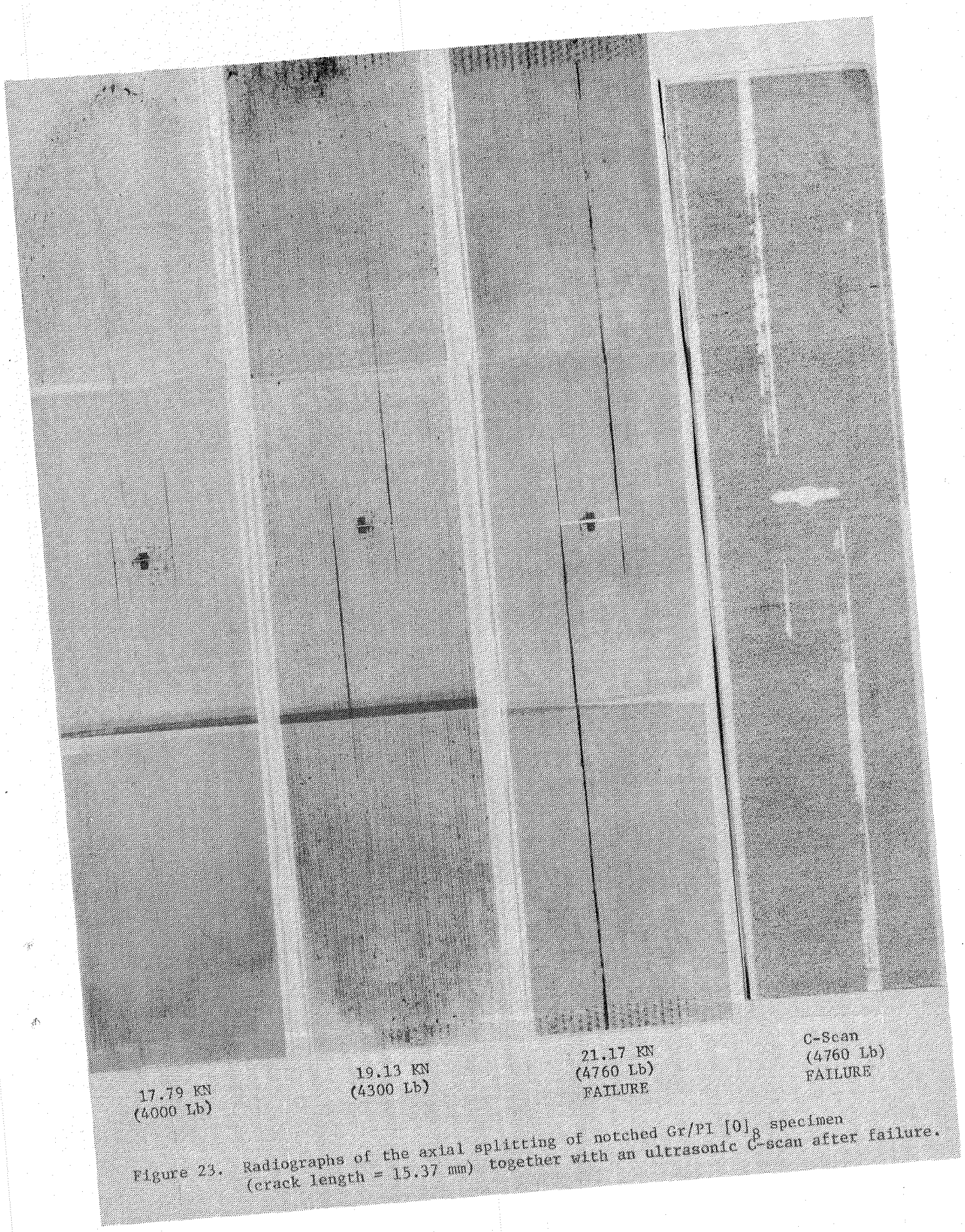

Figure 23. Radiographs of the axial splitting of notched Gr/PI $[0]_8$ specimen (crack length = 15.37 mm) together with an ultrasonic C-scan after failure.

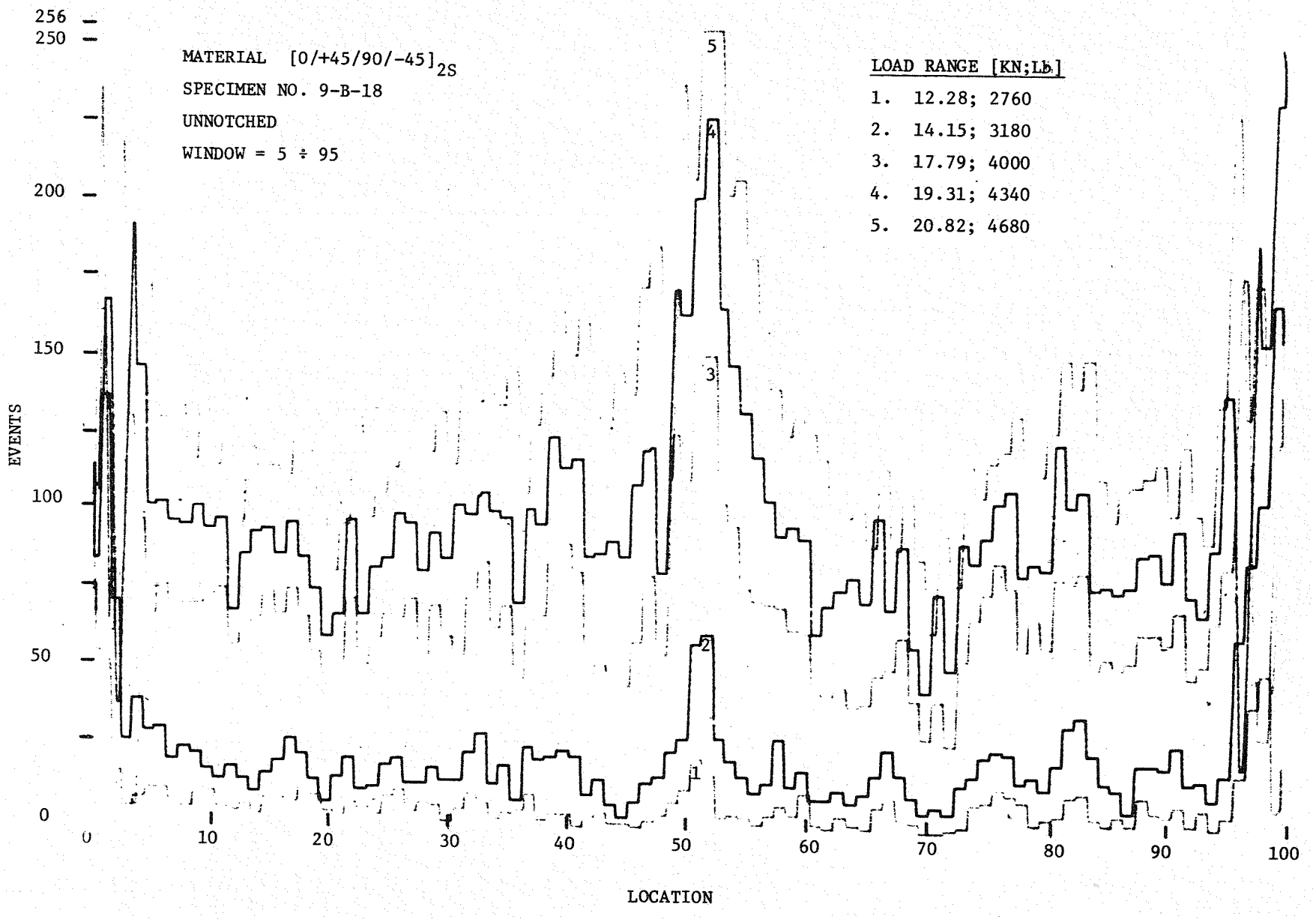

Figure 24. Location distribution histograms of Gr/PI $[0/+45/90/-45]_{2s}$ laminate at various load levels (with spatial discrimination).

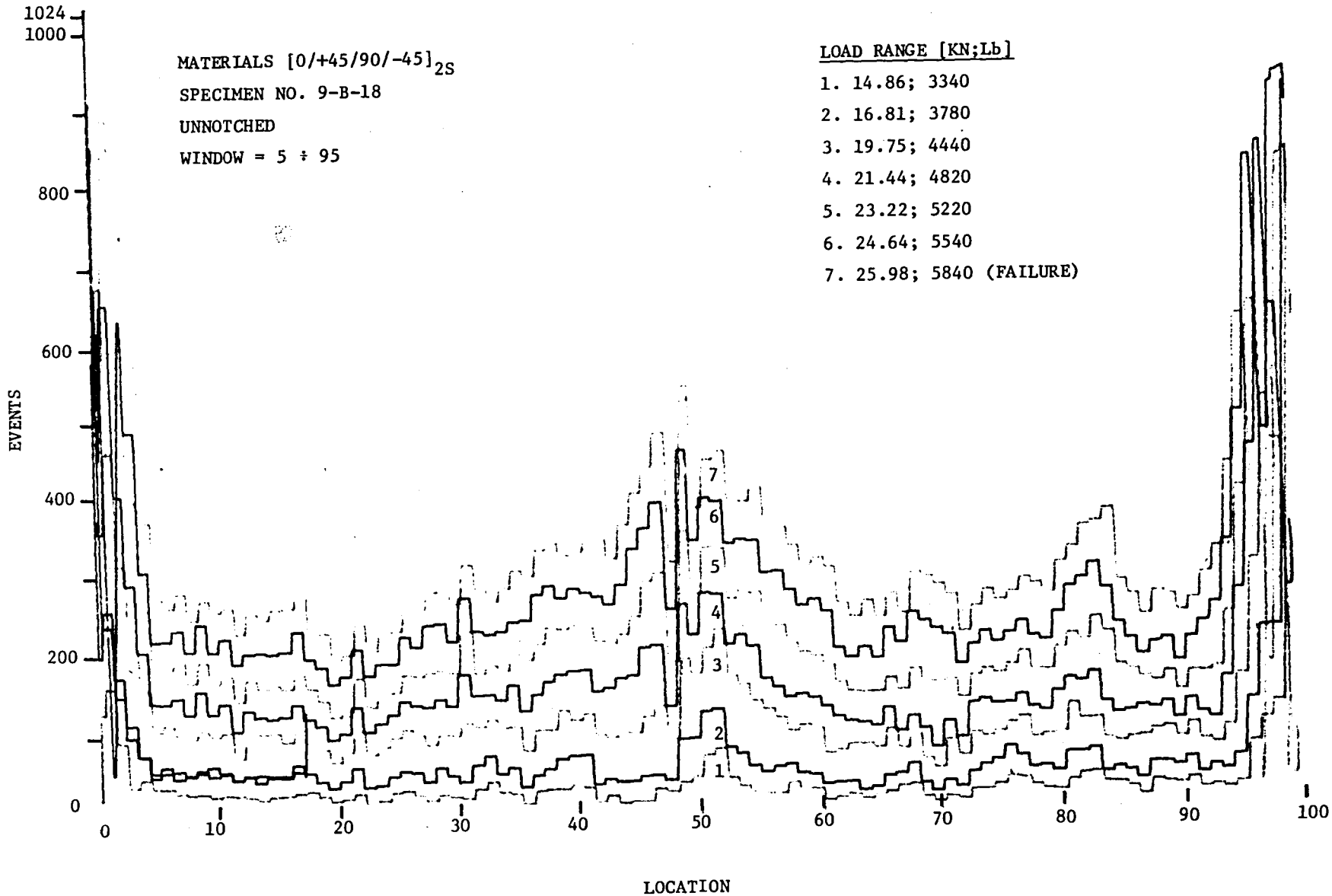

Figure 24. (Continued).

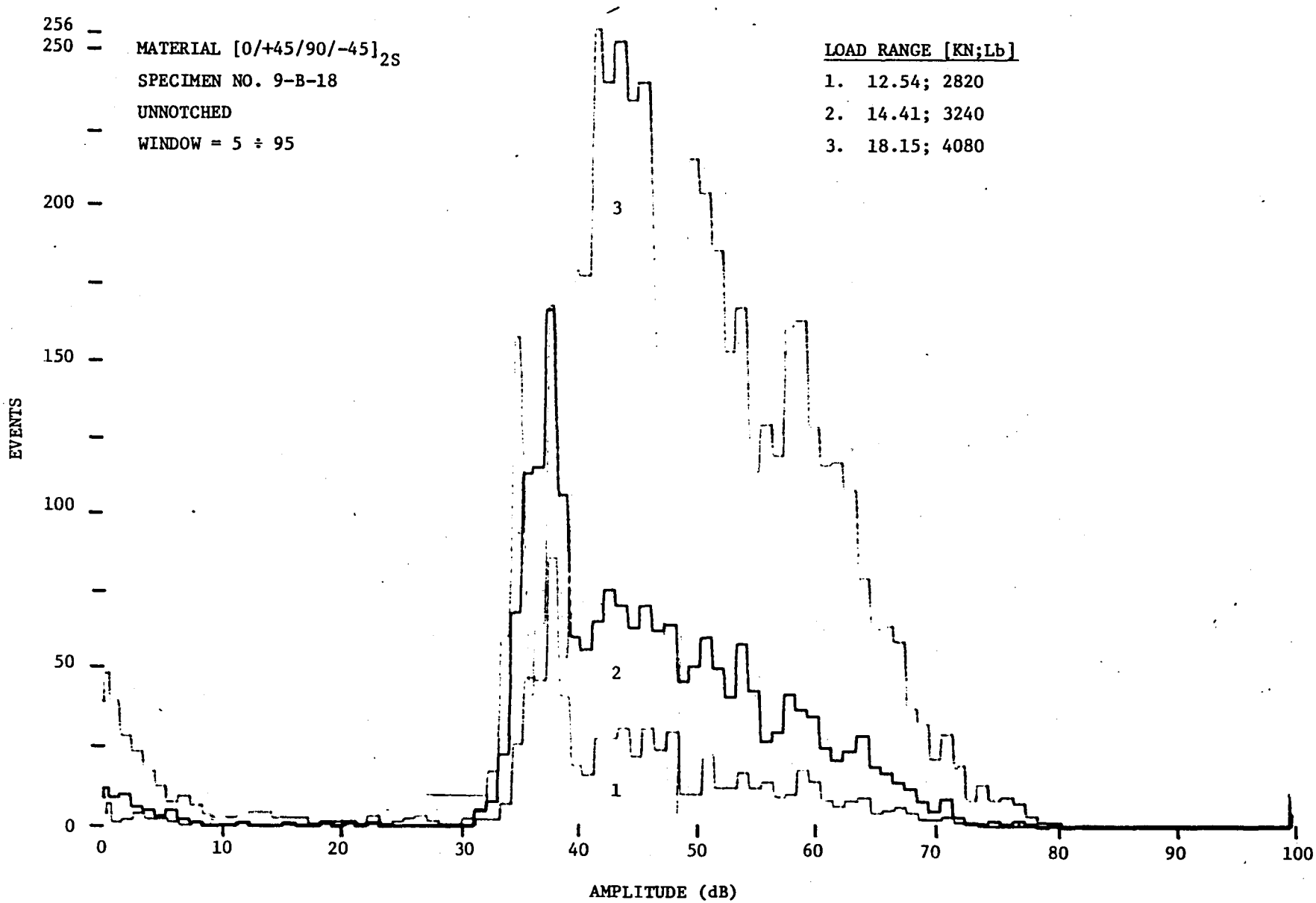

Figure 25. Amplitude distribution histograms for Gr/PI $[0/+45/90/-45]_{2s}$ laminate at various load levels (with spatial discrimination).

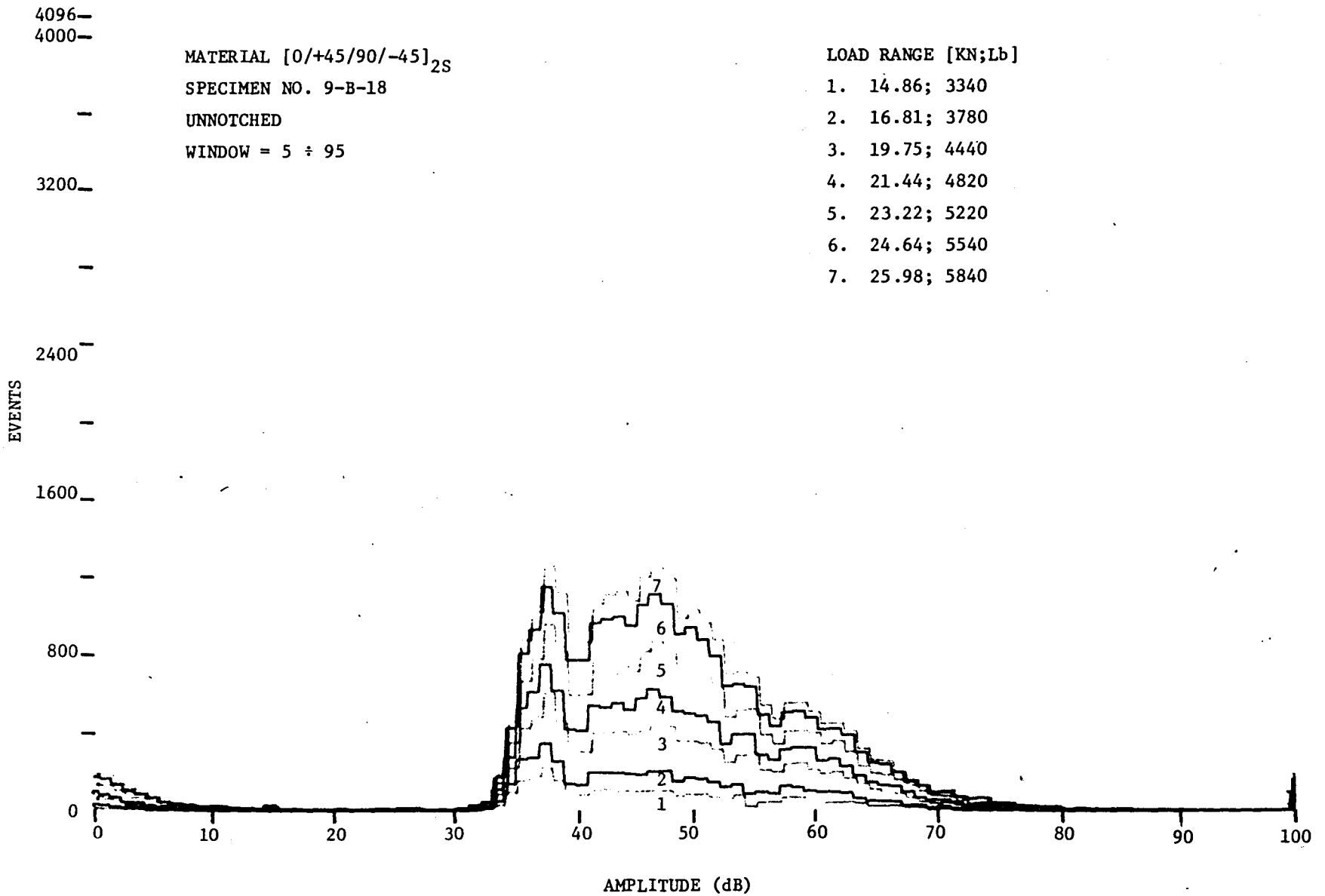

Figure 25. (Continued).

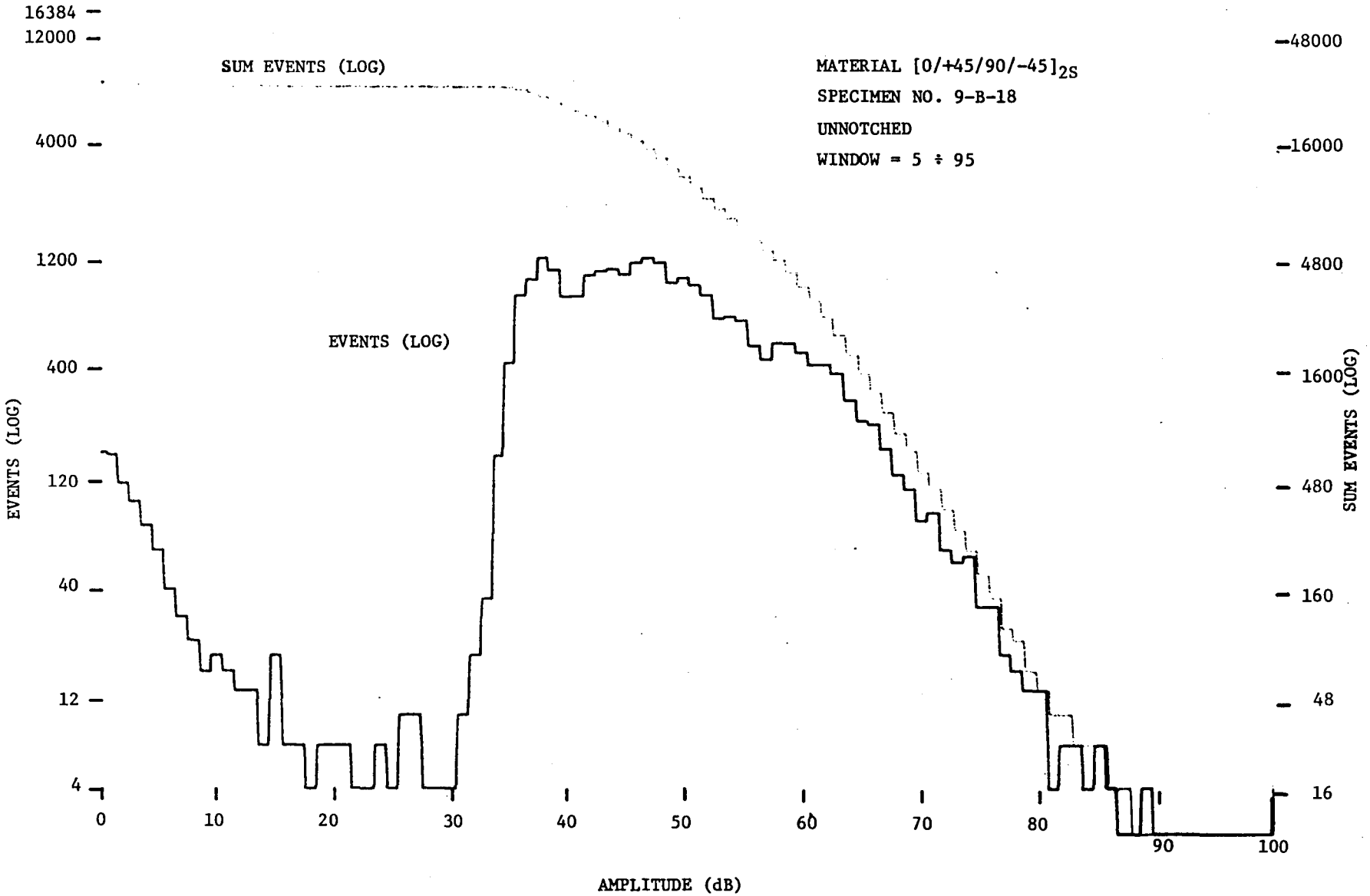

Figure 26. Amplitude distribution histogram and Cumulative Event Amplitude Distribution for Gr/PI $[0/+45/90/-45]_{2s}$ laminate (with spatial discrimination).

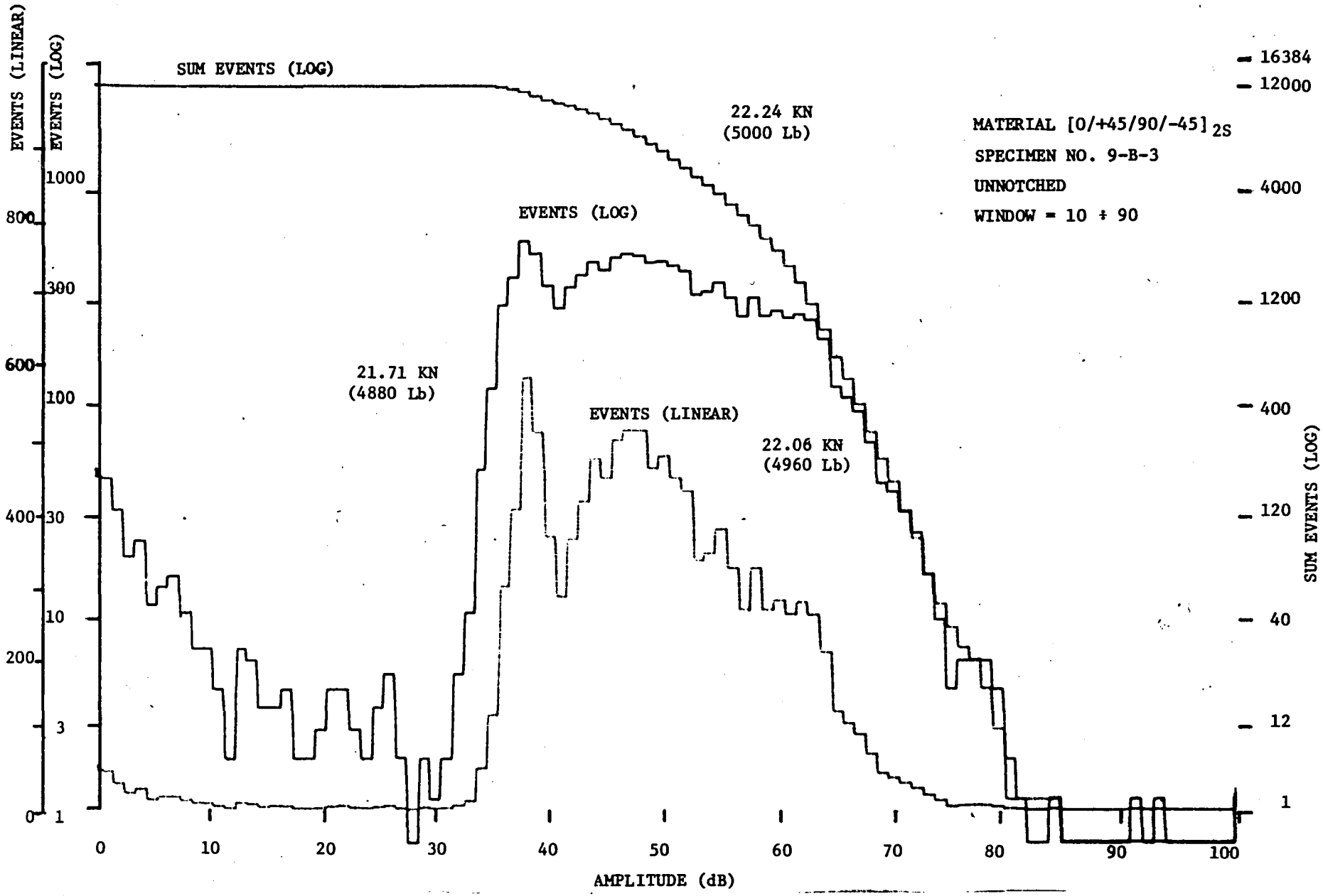

Figure 27. Amplitude distribution histograms (in linear and logarithmic scales) and Cumulative Event Amplitude Distribution for Gr/PI $[0/+45/90/-45]_{2s}$ laminate.

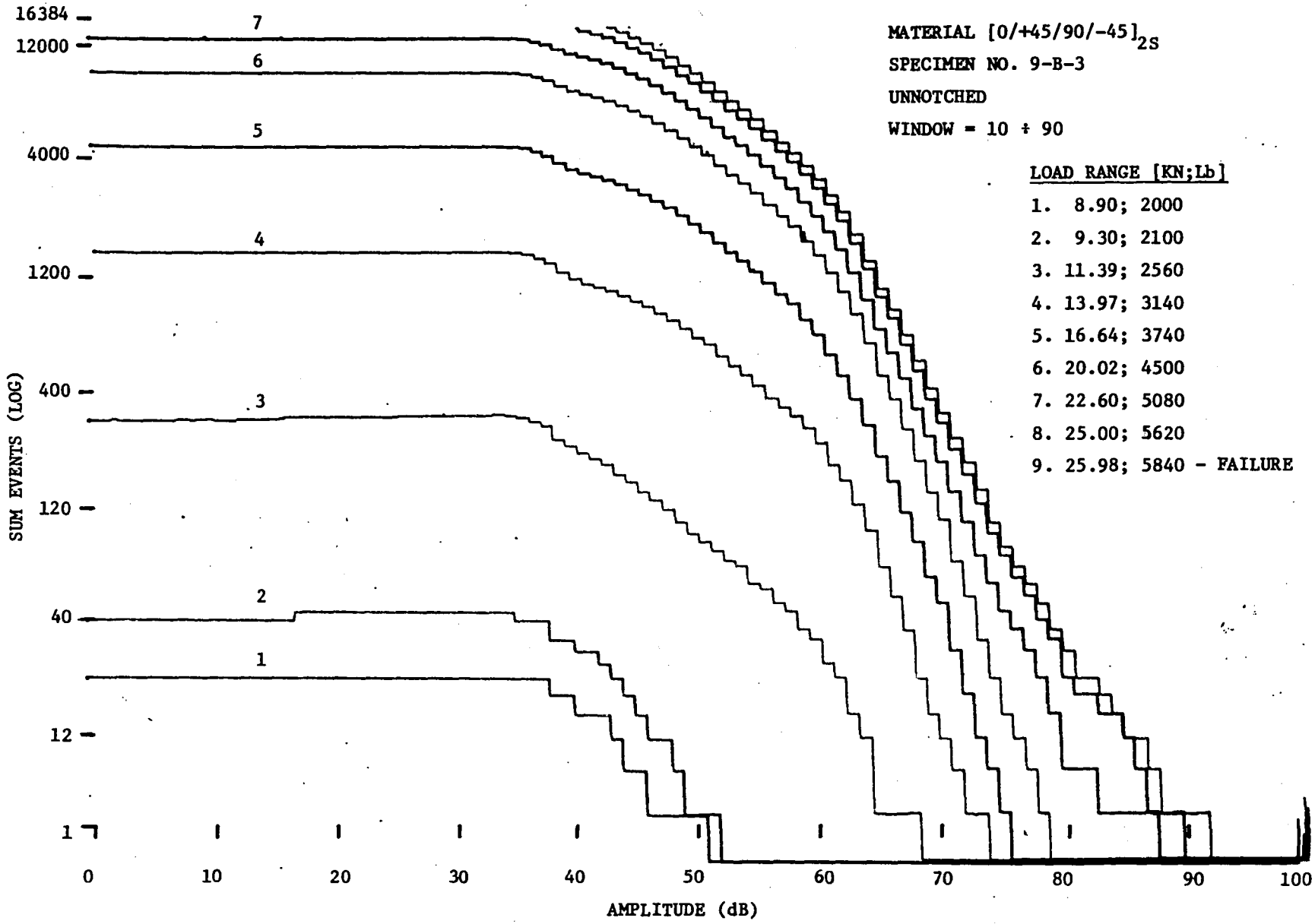

Figure 28. Cumulative Event Amplitude Distribution for Gr/PI $[0/+45/90/-45]_{2s}$ laminate at various load levels.

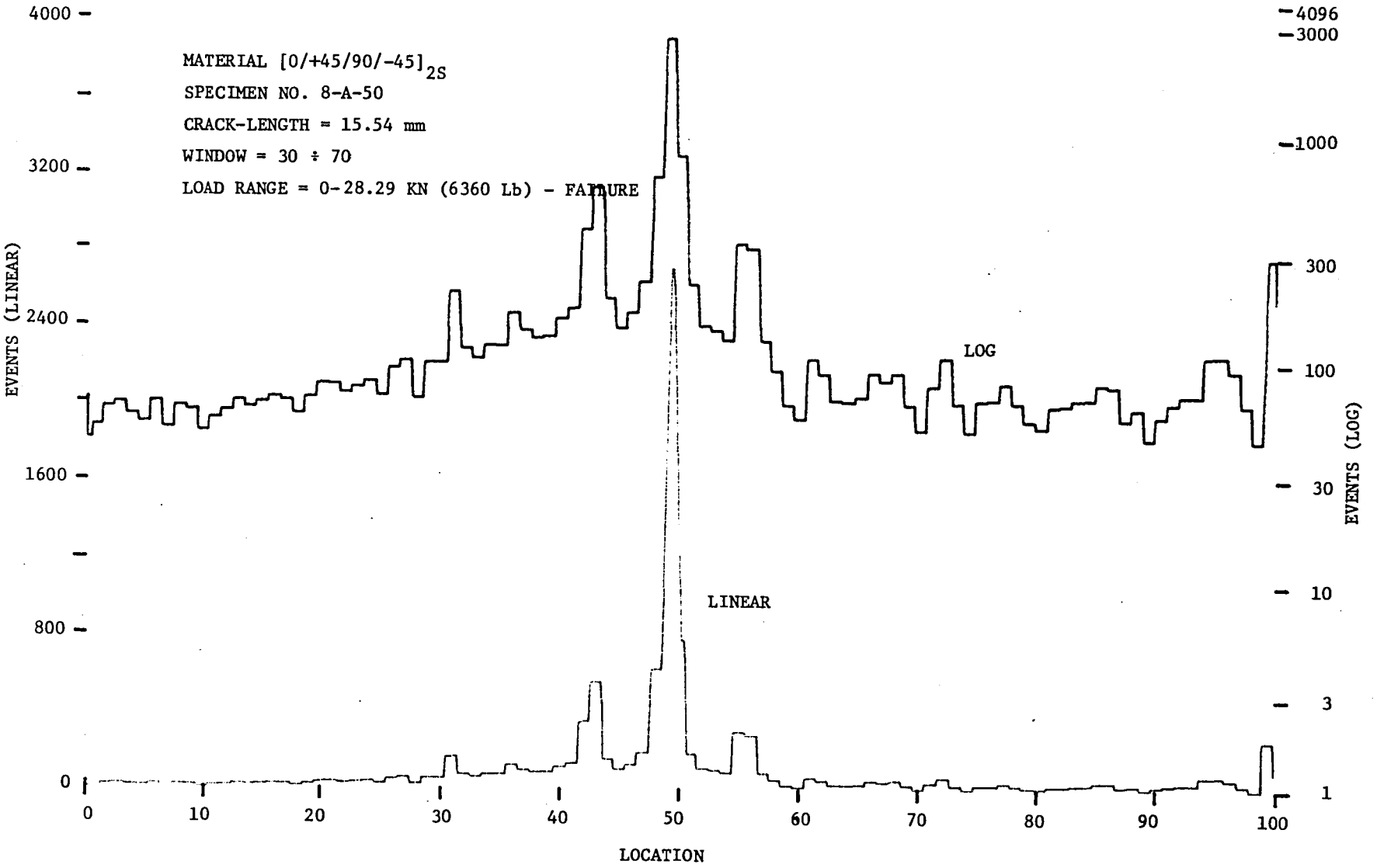

Figure 29. Location distribution histogram (in linear and logarithmic scales) for notched Gr/PI $[0/+45/90/-45]_{2s}$ laminate (crack length = 15.54 mm).

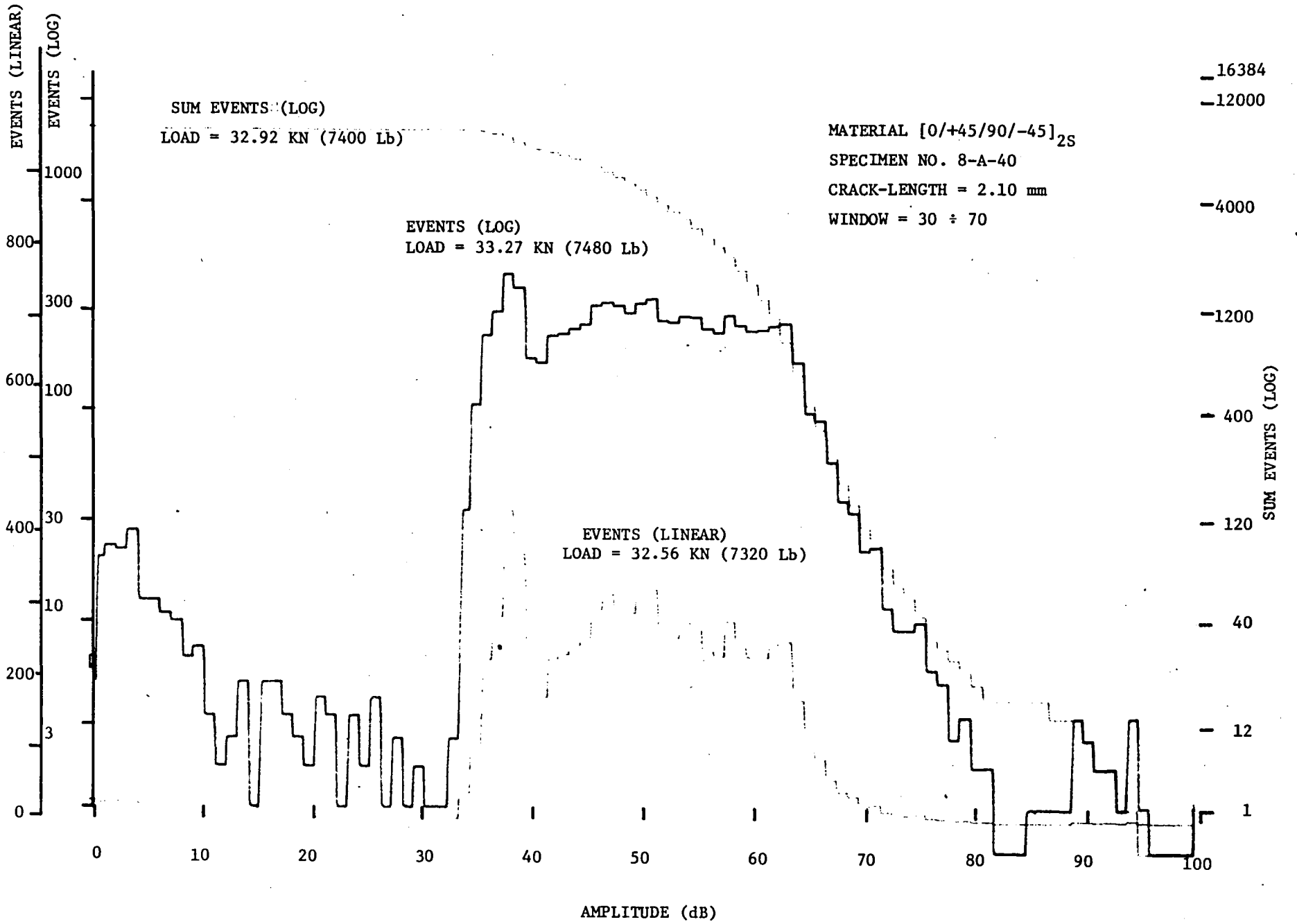

Figure 30. Amplitude distribution histogram (in linear and logarithmic scales) and Cumulative Event Amplitude Distribution for notched Gr/PI $[0/+45/90/-45]_{2s}$ laminate (crack length = 2.10 mm).

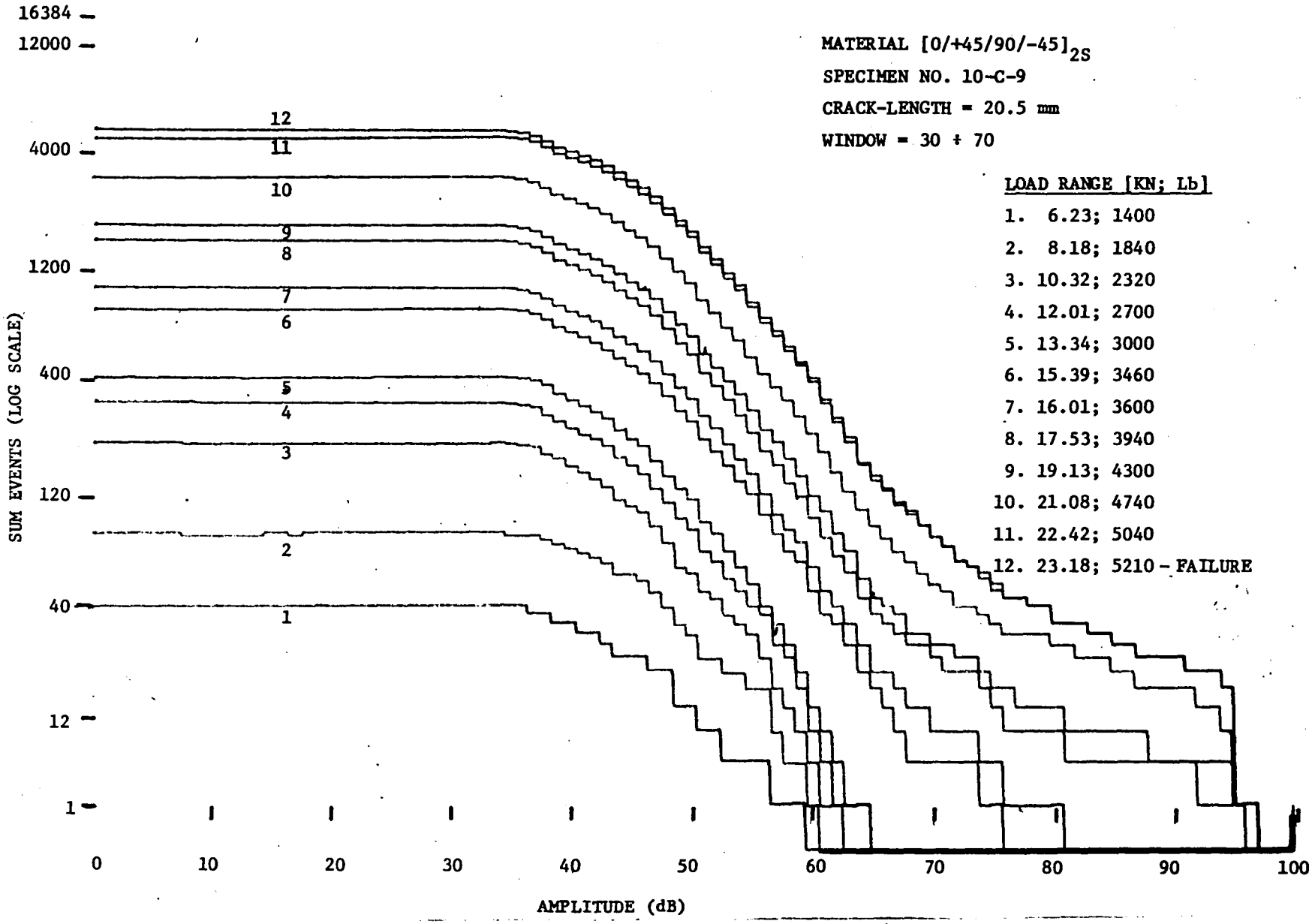

Figure 31. Cumulative Event Amplitude Distribution for notched Gr/PI $[0/+45/90/-45]_{2s}$ laminate at various load levels (crack length = 20.5 mm).

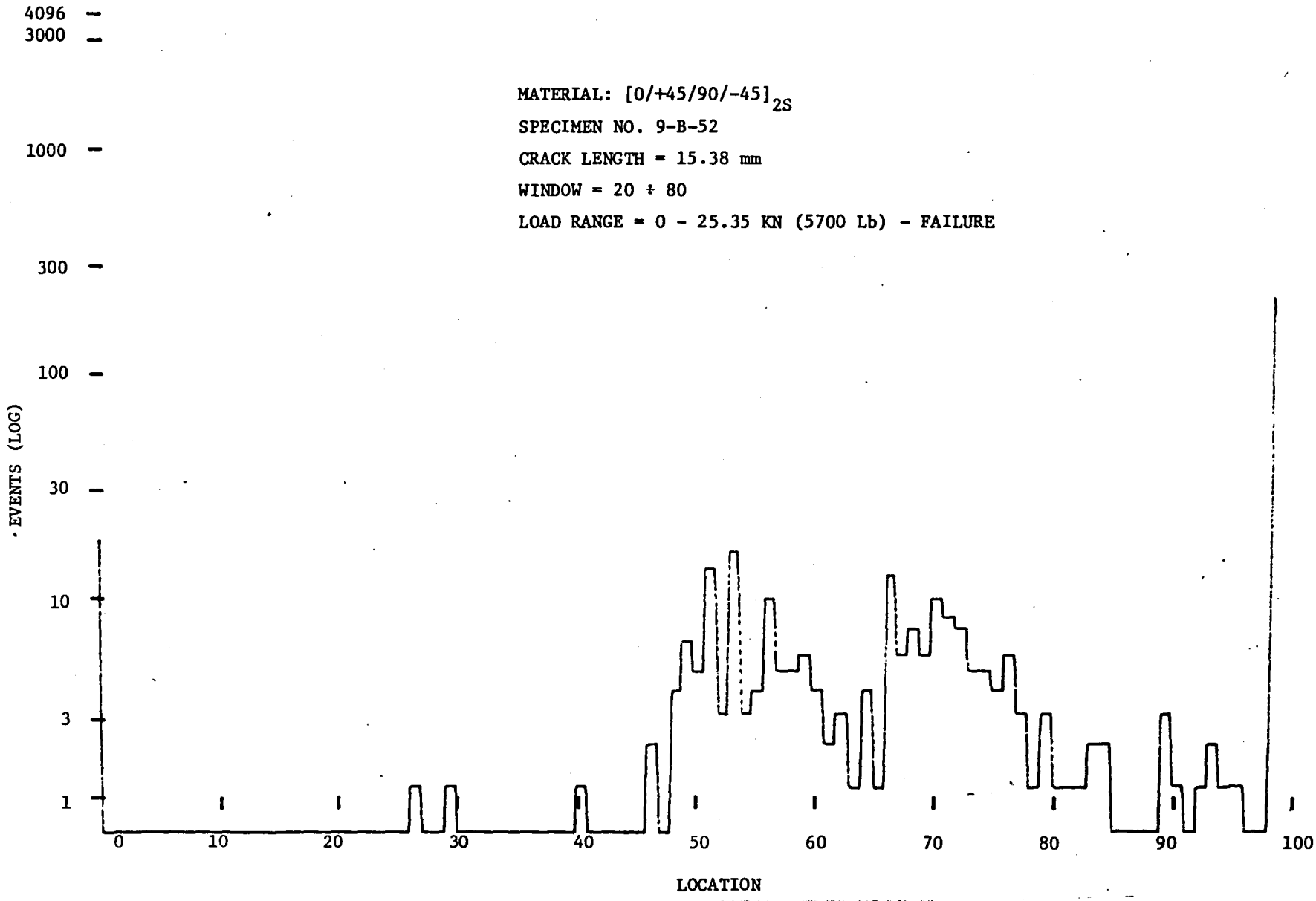

Figure 32. Location distribution histogram for notched Gr/PI $[0/+45/90/-45]_{2s}$ laminate at 450°F (crack length = 15.38 mm).

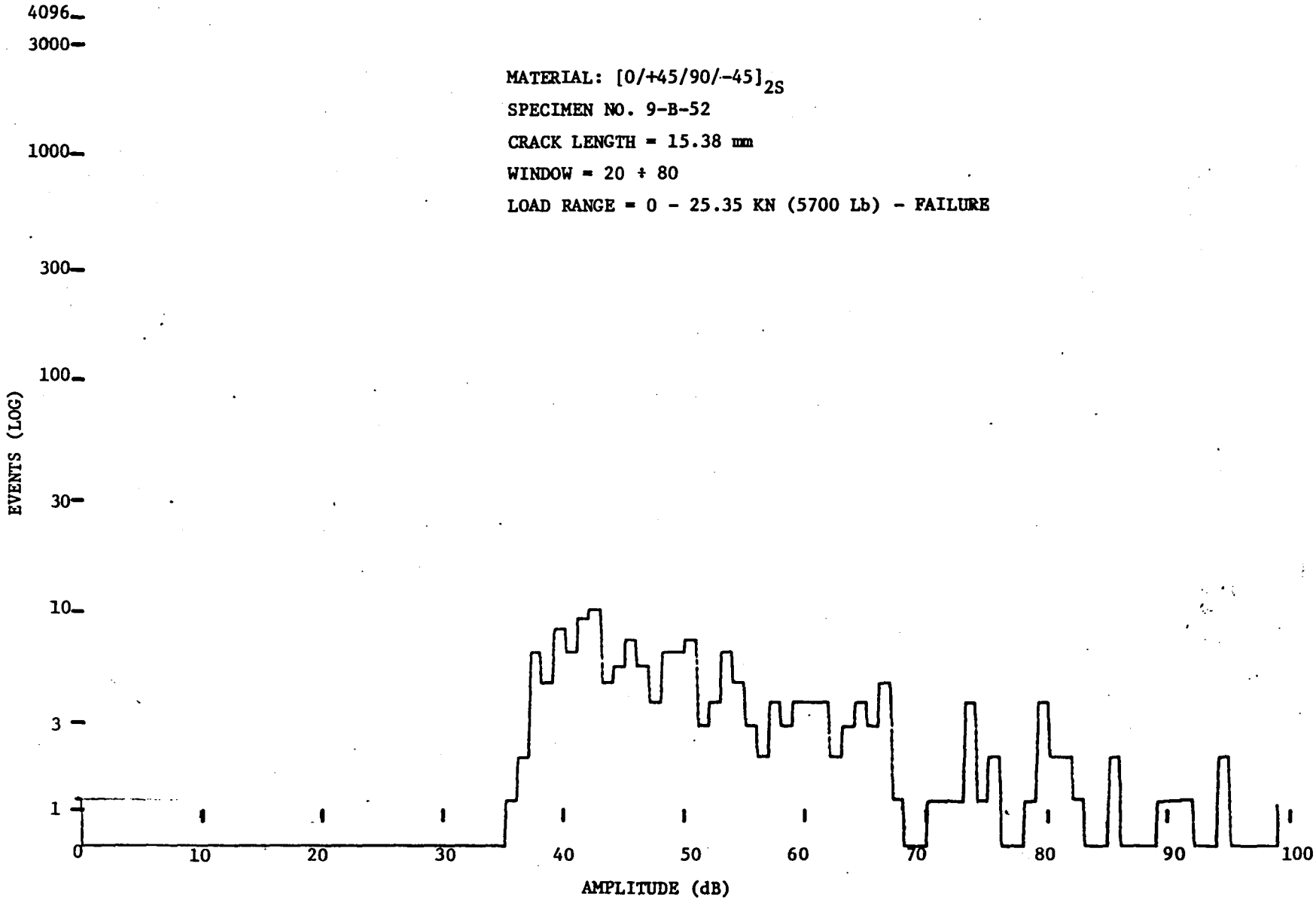

Figure 33. Amplitude distribution histogram for notched Gr/PI $[0/+45/90/-45]_{2s}$ laminate at 450°F (crack length = 15.38 mm).

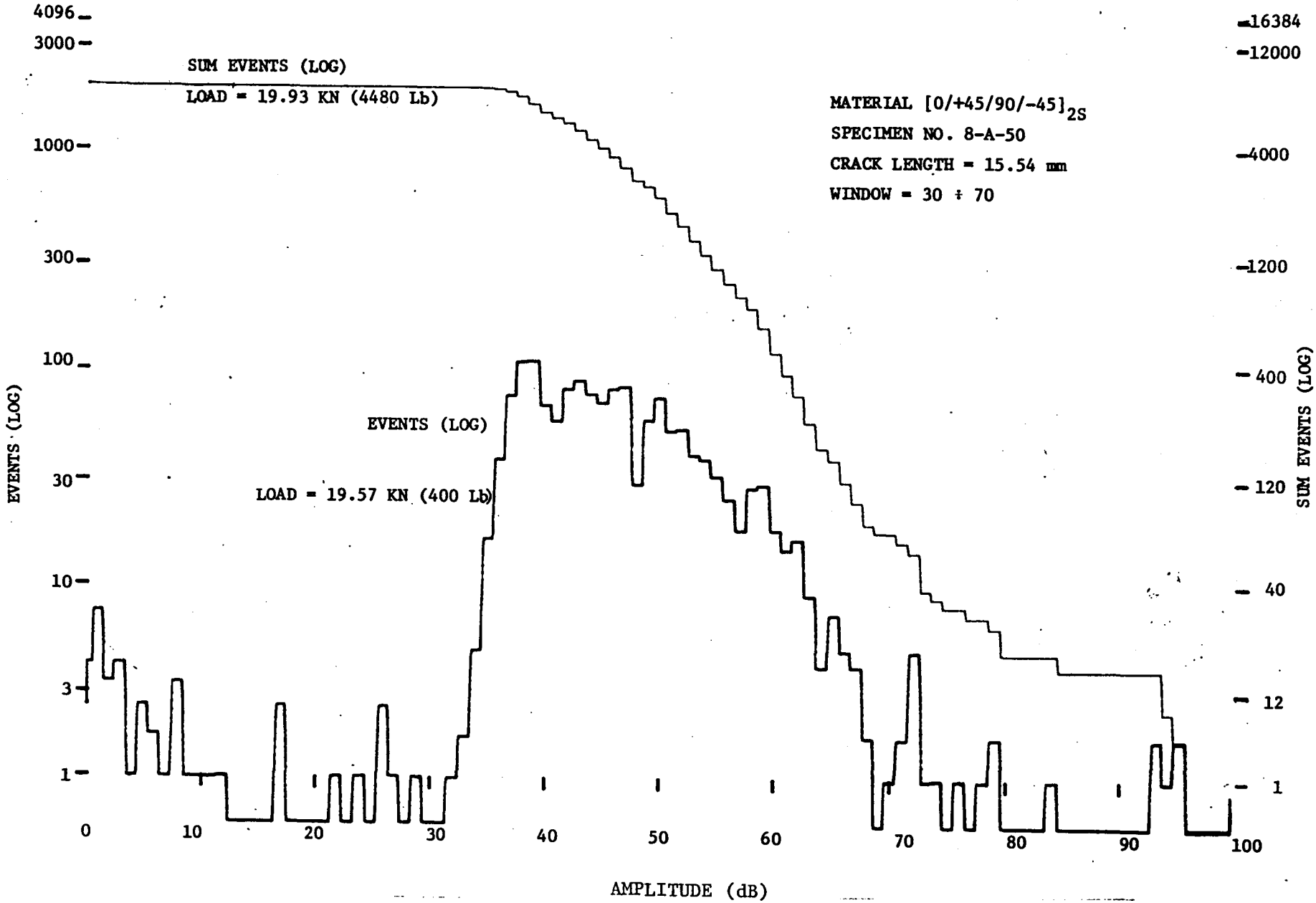

Figure 34. Amplitude distribution histogram and Cumulative Event Amplitude Distribution for notched Gr/PI $[0/+45/90/-45]_{2s}$ laminate (crack length = 15.54 mm).

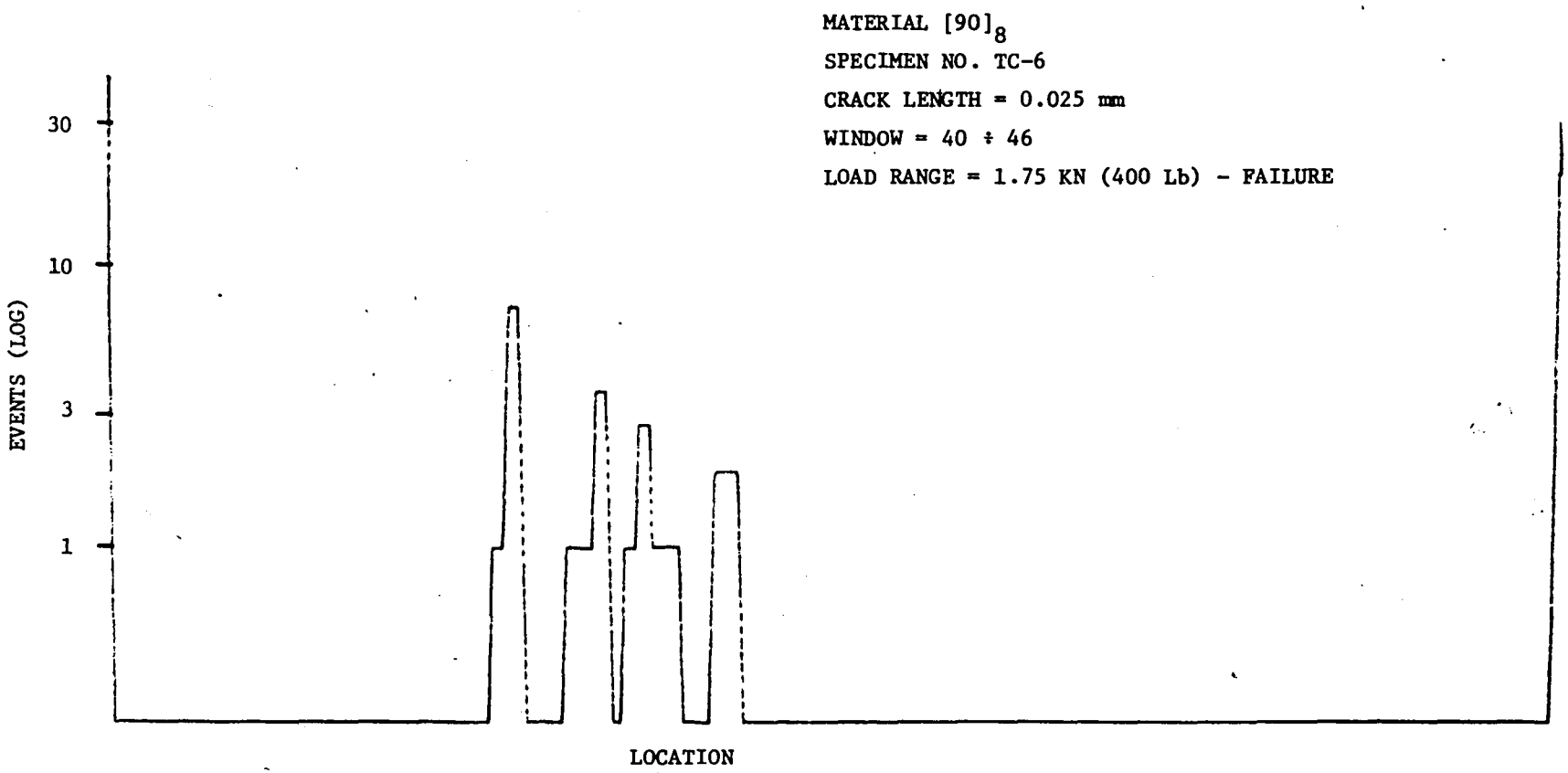

Figure 35. Location distribution histogram for edge notched Gr/PI $[90]_8$ specimen (crack length = 0.025 mm).

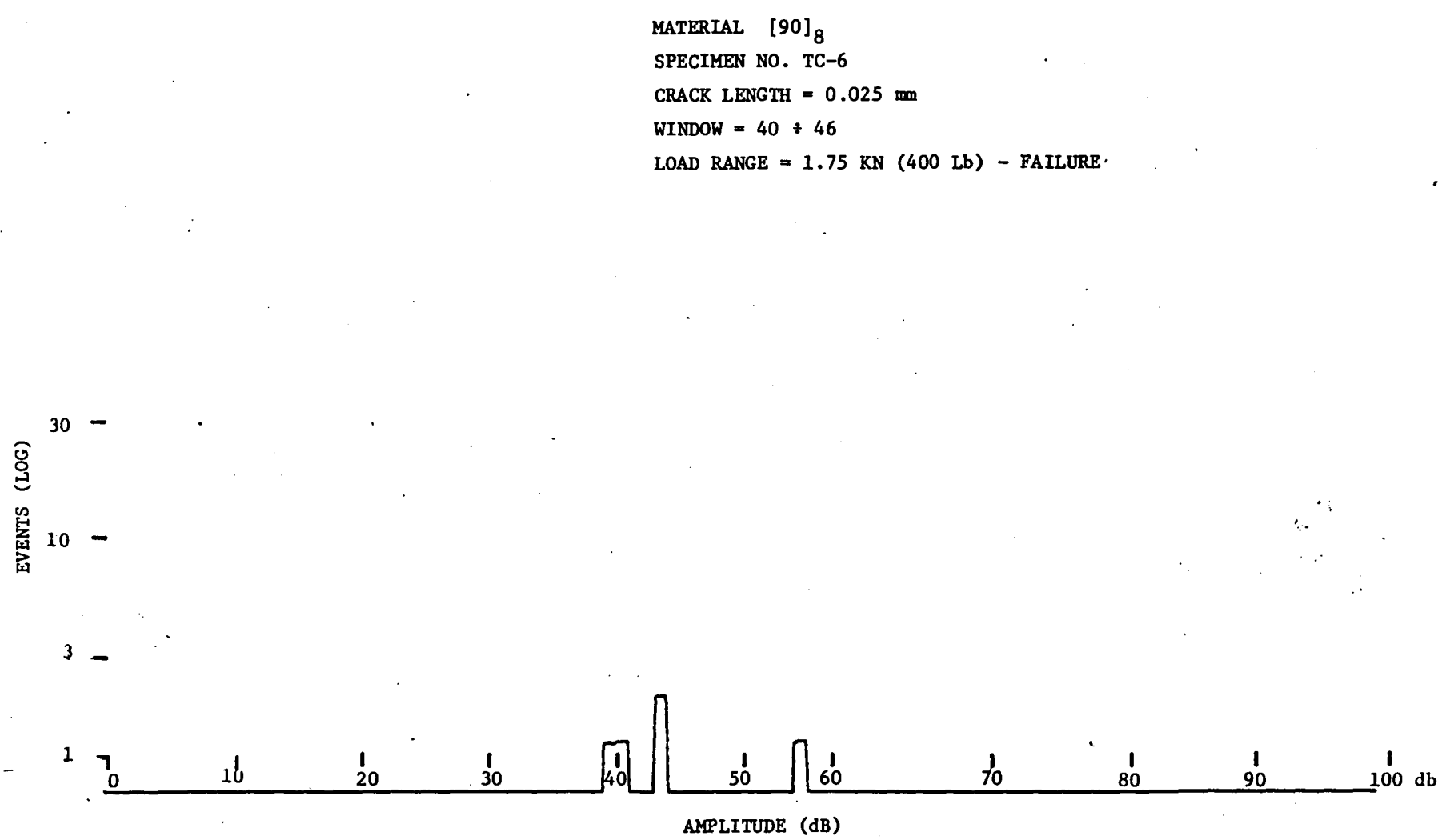

Figure 36. Amplitude distribution histogram for edge notched Gr/PI $[90]_8$ specimen (crack length = 0.025 mm).

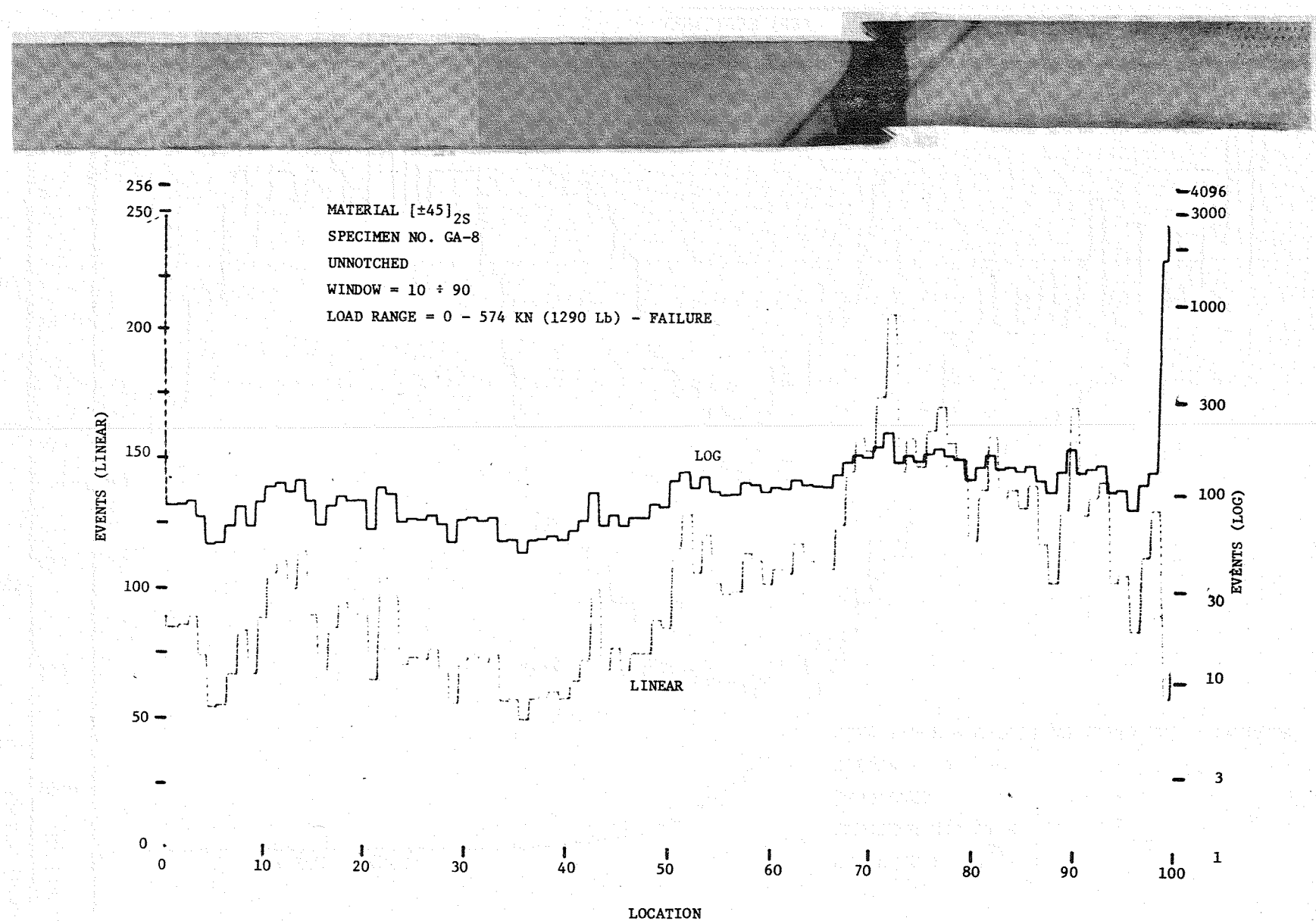

Figure 37. Location distribution histogram (in linear and logarithmic scales) for Gr/PI $[\pm 45]_{2s}$ laminate together with the specimen's radiograph.

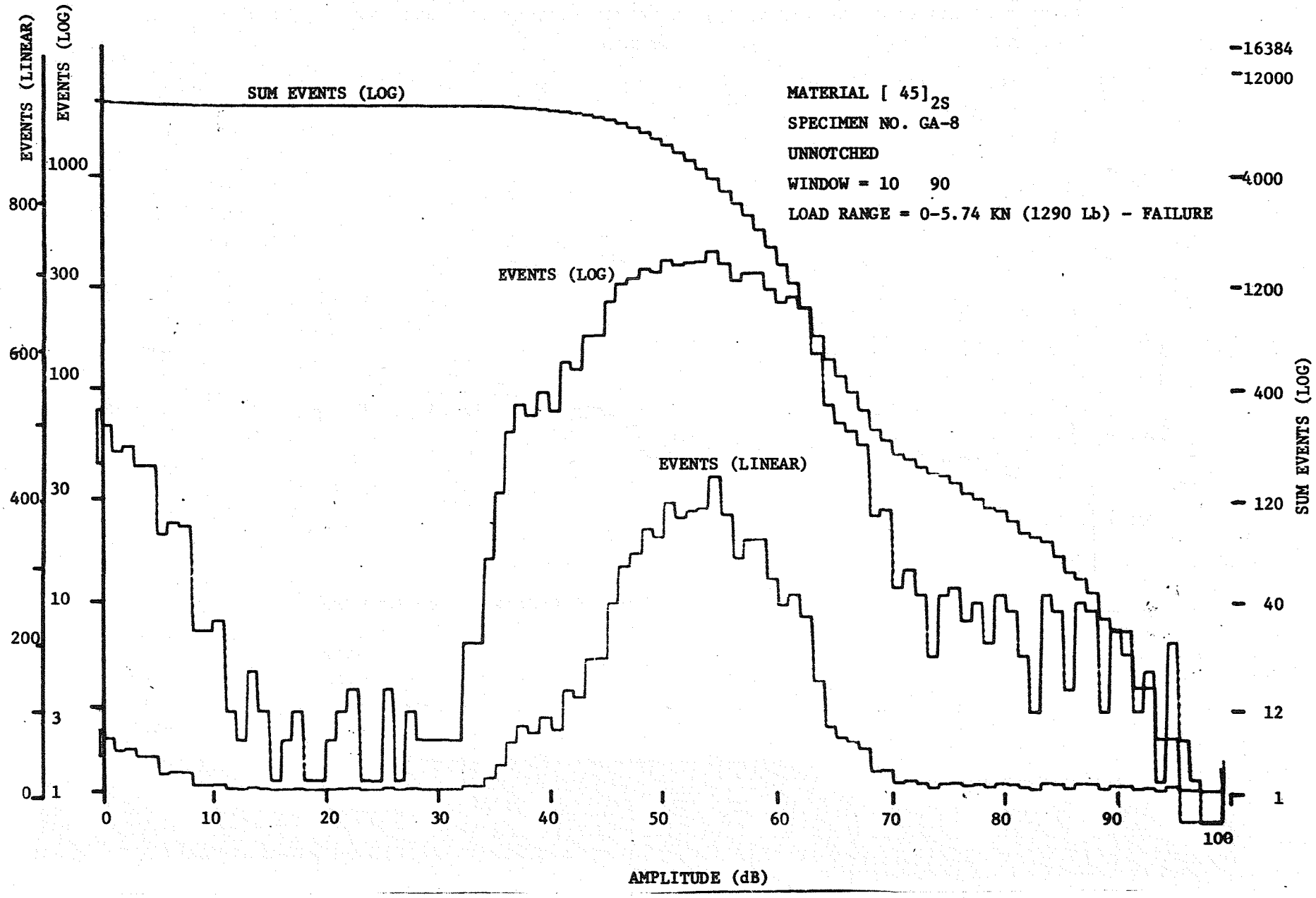

Figure 38. Amplitude distribution histogram (in linear and logarithmic scales) and Cumulative Event Amplitude Distribution for Gr/PI $[\pm 45]_{2s}$ laminate.

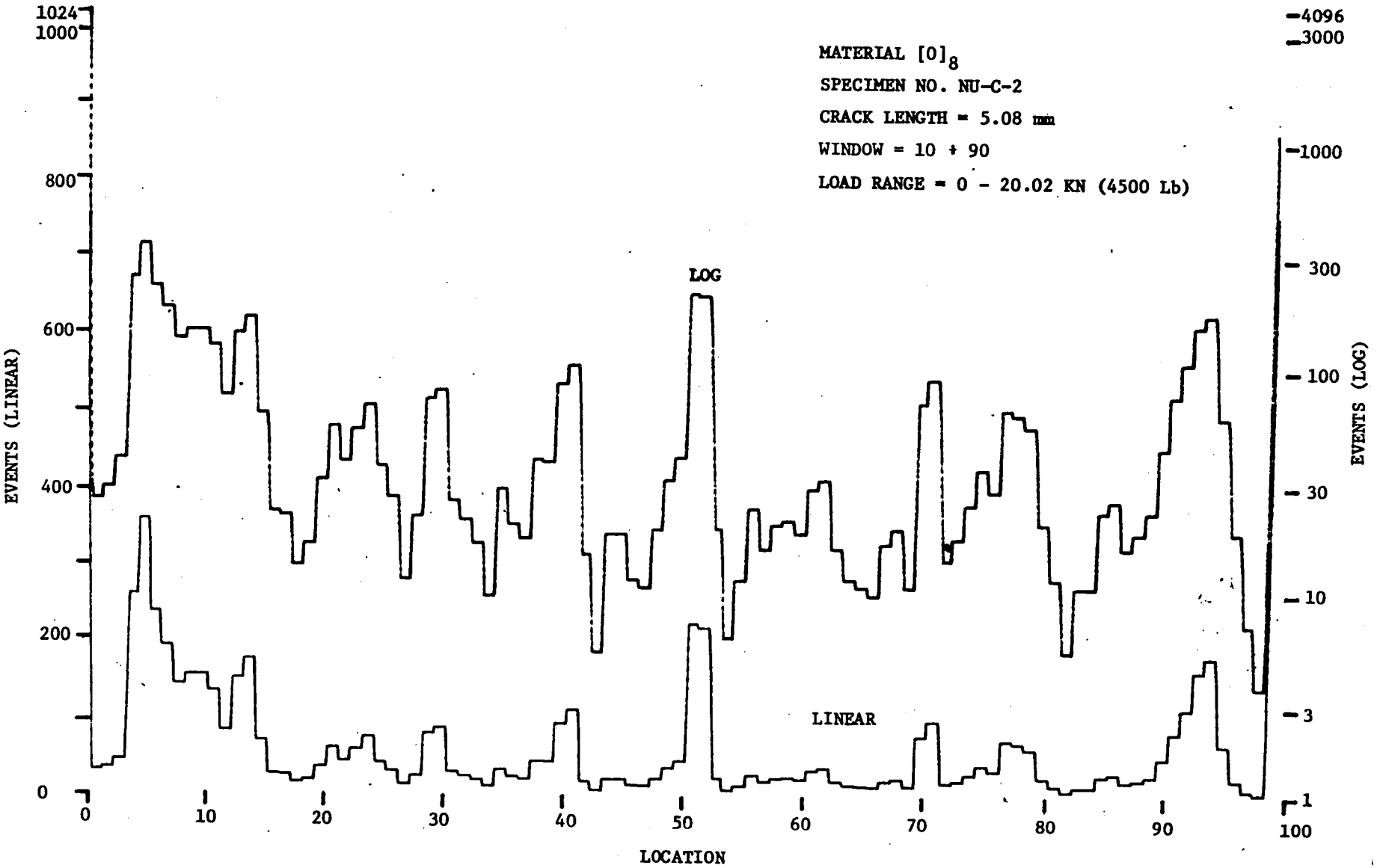

Figure 39. Location distribution histogram (in linear and logarithmic scales) for notched Gr/PI $[0]_8$ specimen (crack length = 5.08 mm) after loading to 20.2 KN (4500 lb).

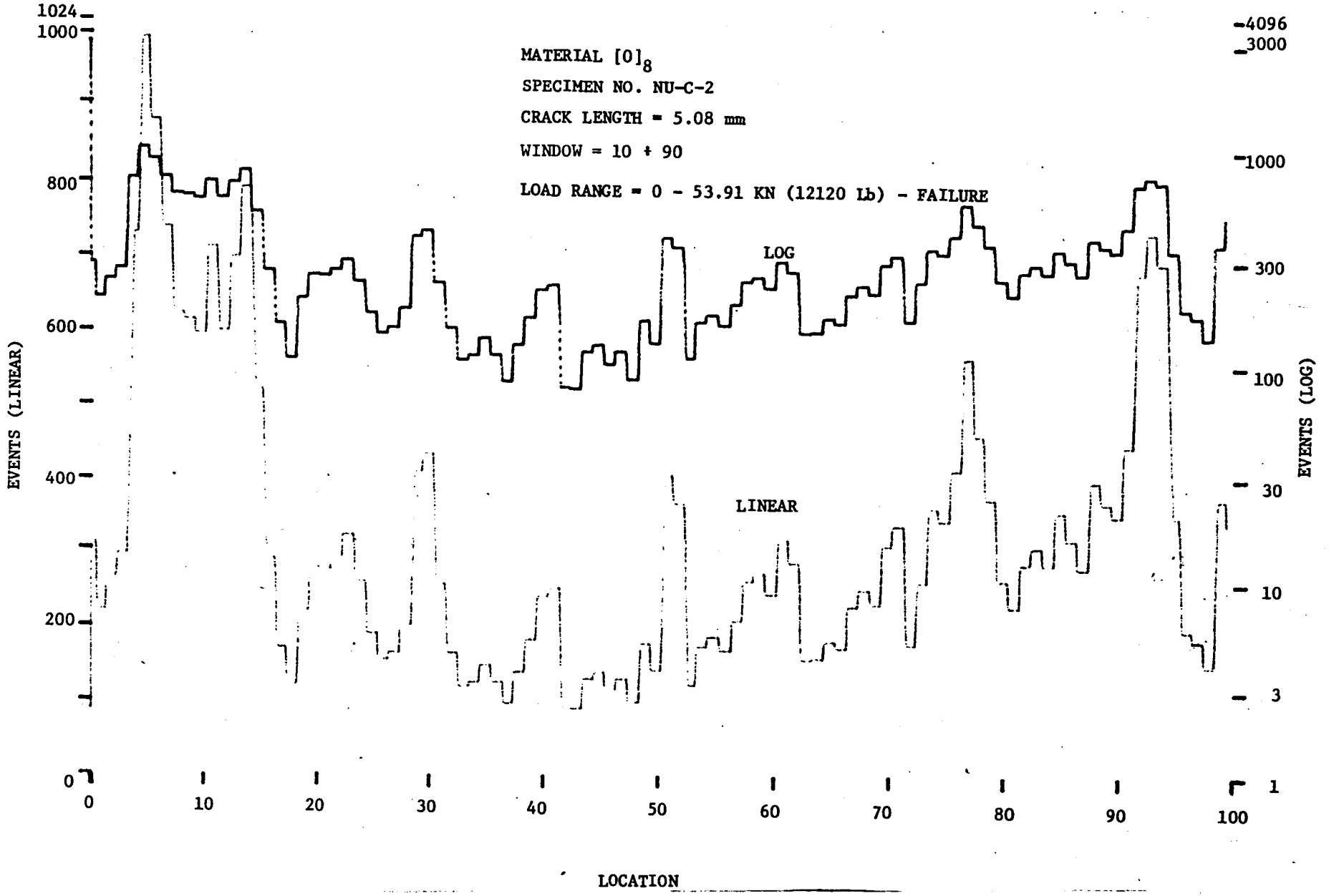

Figure 40. Location distribution histogram (in linear and logarithmic scales) for notched Gr/PI $[0]_8$ specimen (crack length = 5.08 mm) after failure (53.91 KN, 12120 lb).

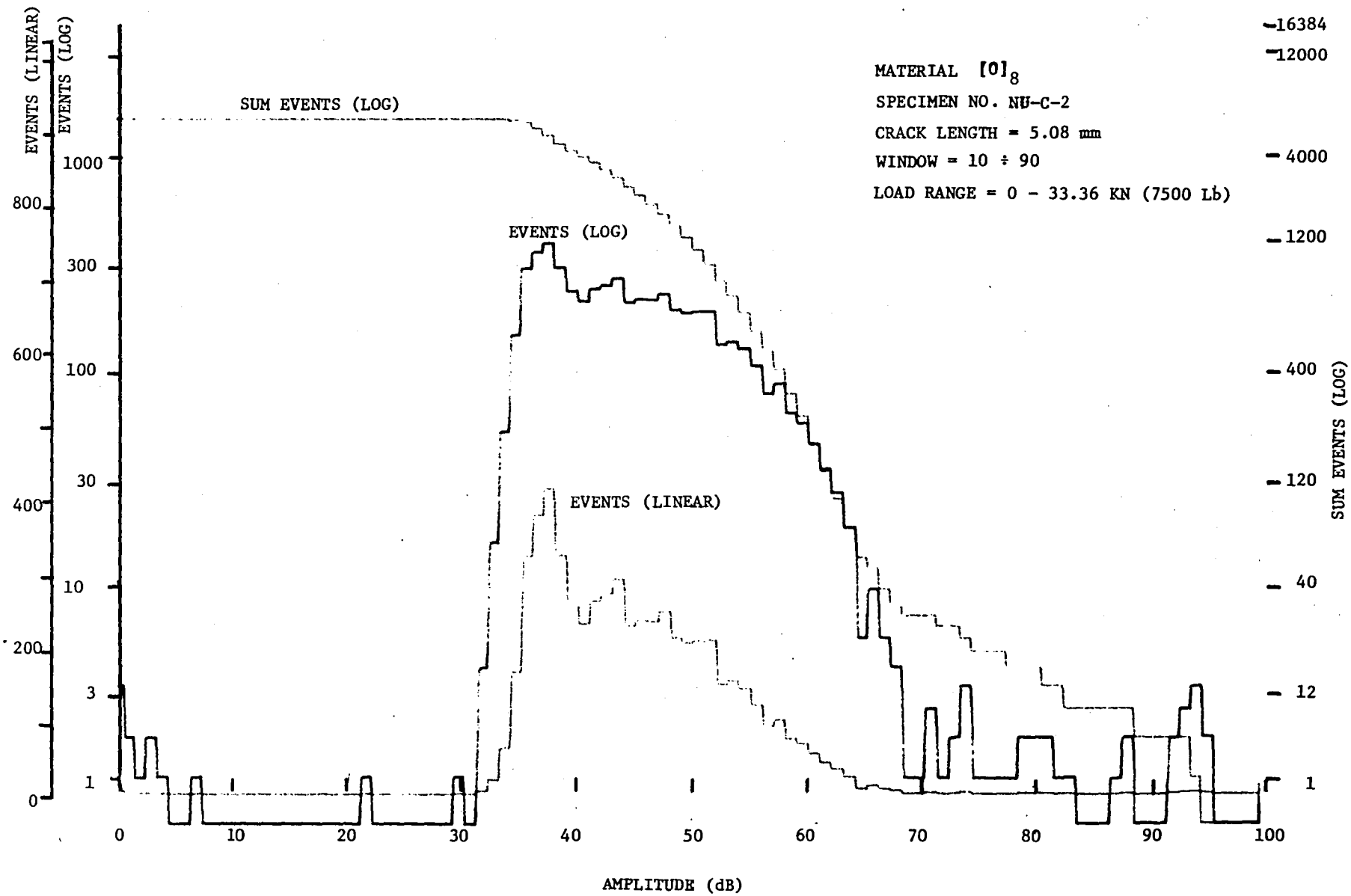

Figure 41. Amplitude distribution histogram (in linear and logarithmic scales) and Cumulative Event Amplitude Distribution for notched Gr/PI $[0]_8$ specimen (crack length = 5.08 mm) after loading to 33.36 KN (7500 lb).

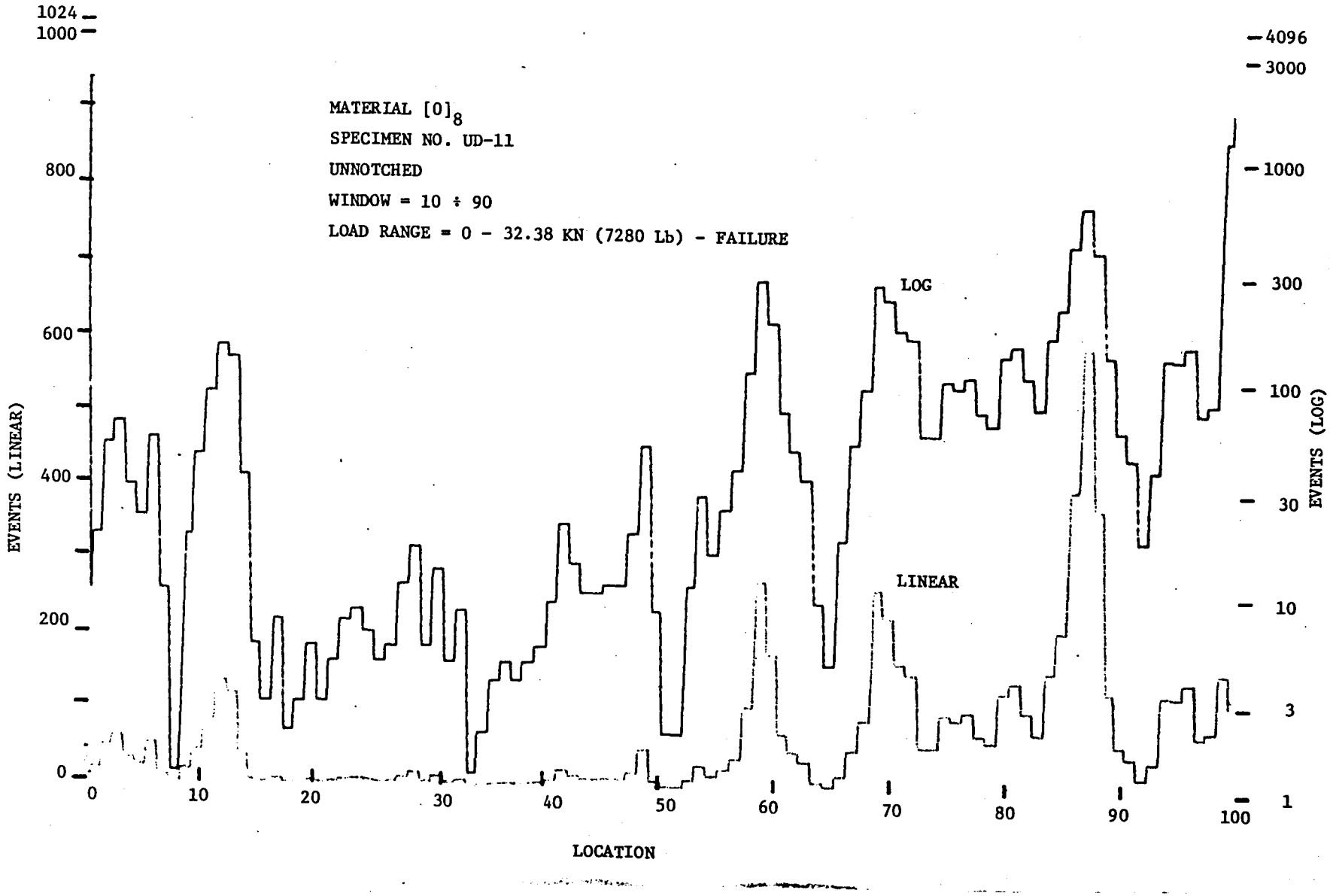

Figure 42. Location distribution histogram (in linear and logarithmic scales) for Gr/PI $[0]_8$ specimen.

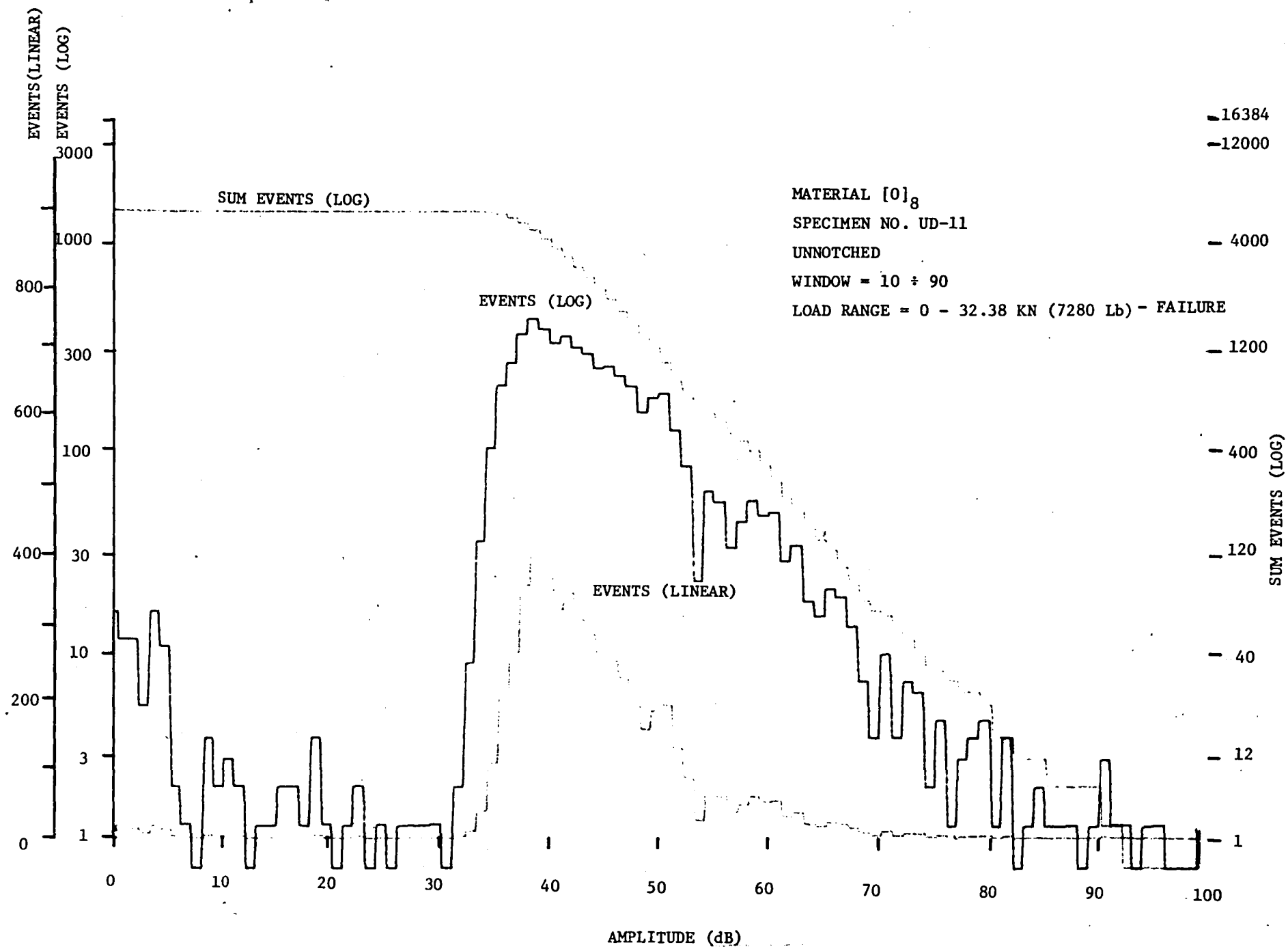

Figure 43. Amplitude distribution histogram (in linear and logarithmic scales) and Cumulative Event Amplitude Distribution for Gr/PI $[0]_8$ specimen.

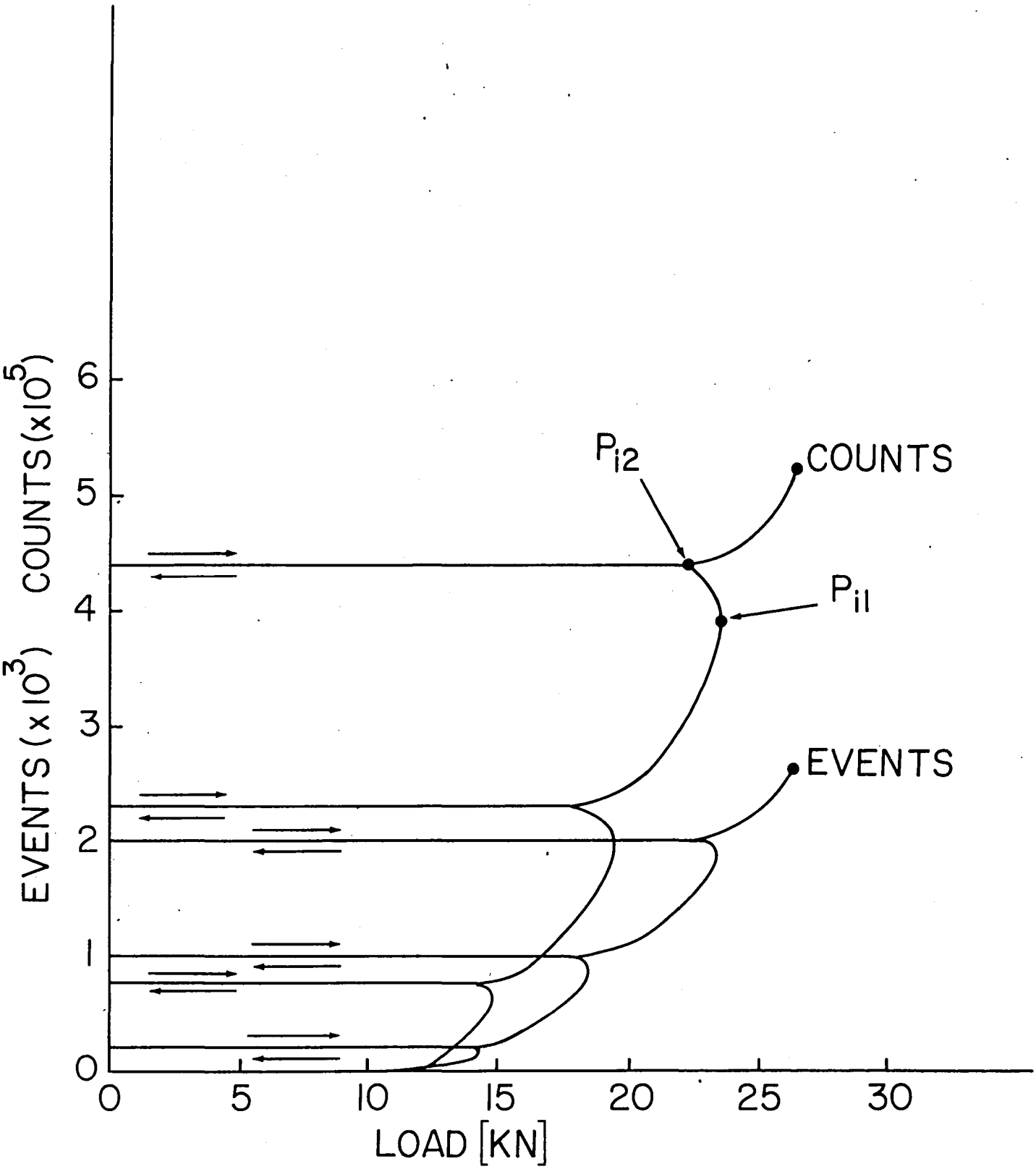

Figure 44. Accumulative counts and events as a function of load during loading/unloading cycles for Gr/PI $[0/+45/90/-45]_{2s}$ laminate.

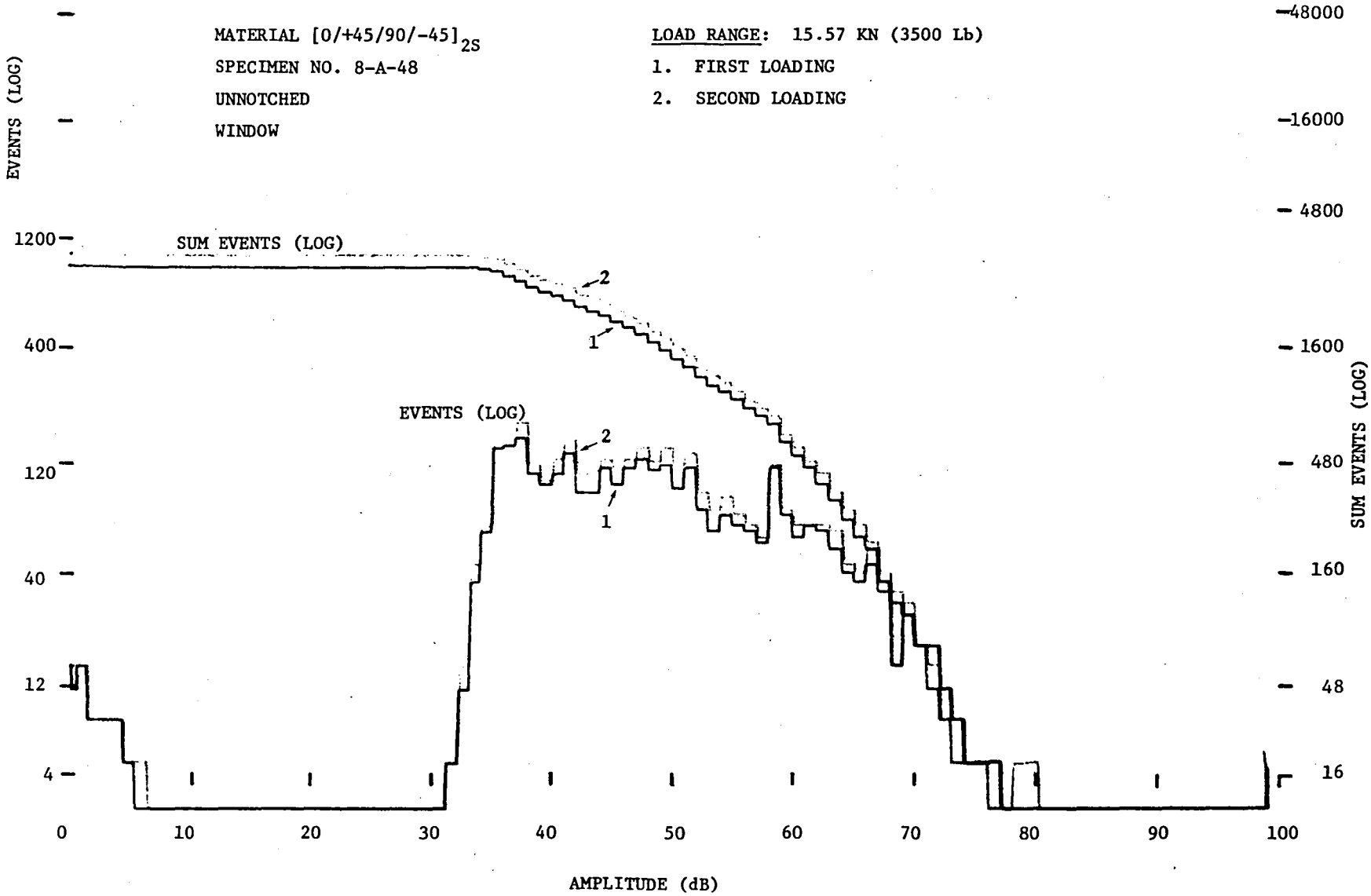

Figure 45. Amplitude distribution histogram (in logarithmic scale) and Cumulative Event Amplitude Distribution at two different load cycles.

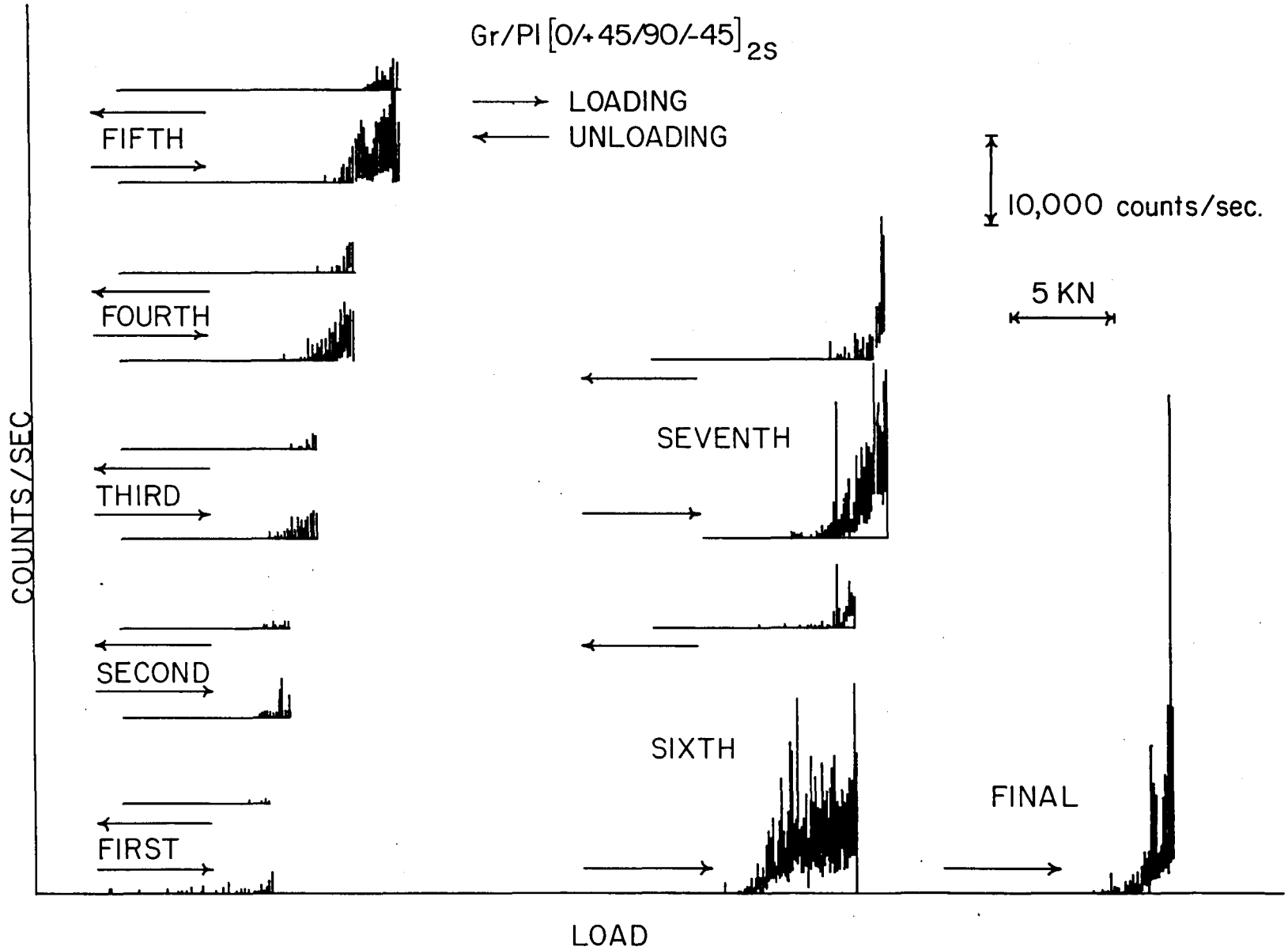

Figure 46. Count rate as a function of load during loading/unloading cycles for Gr/PI $[0/+45/90/-45]_{2s}$ laminate.

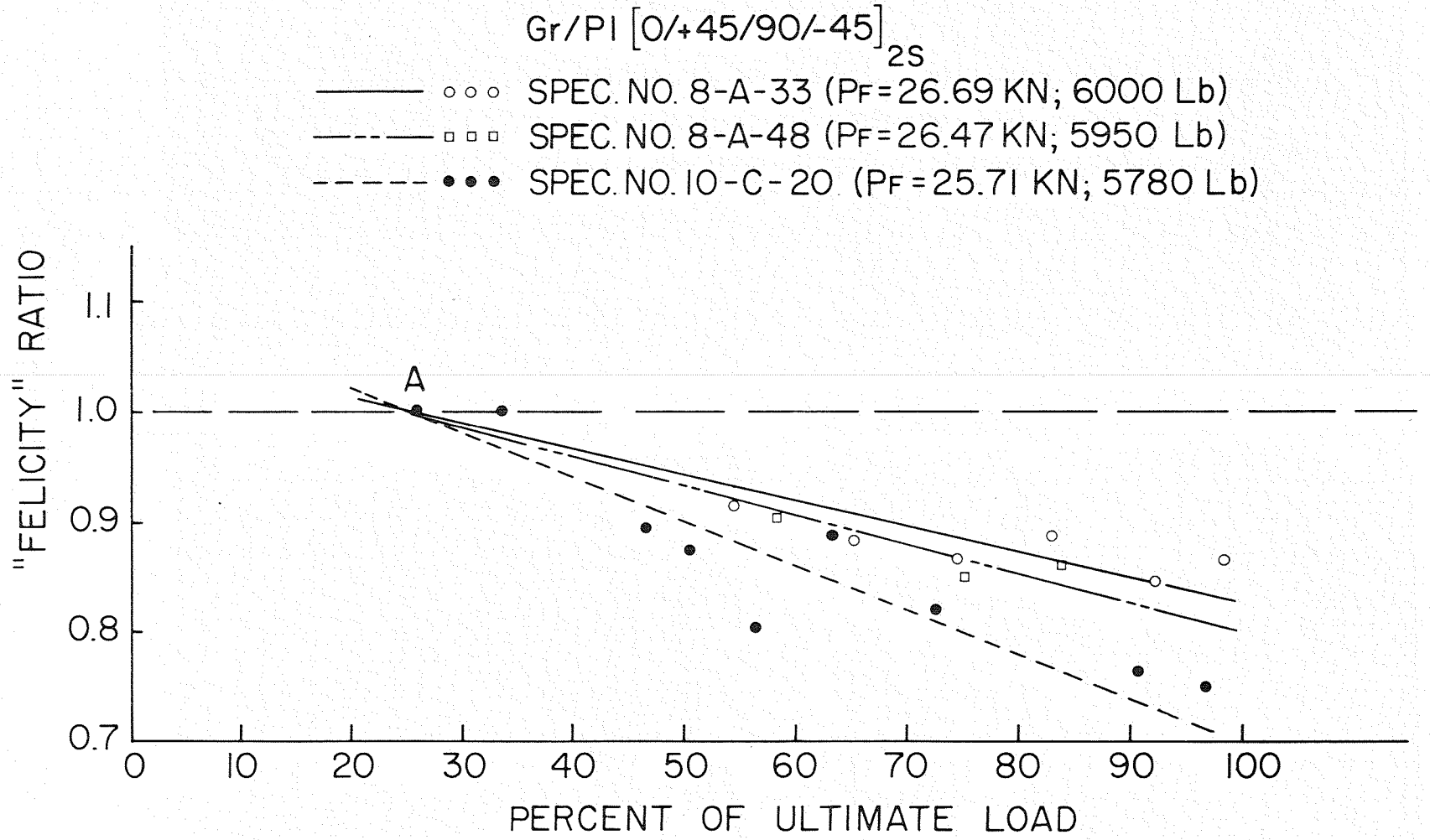

Figure 47. The Felicity ratio as a function of percent of ultimate load for various Gr/PI $[0/+45/90/-45]_{2s}$ specimens.

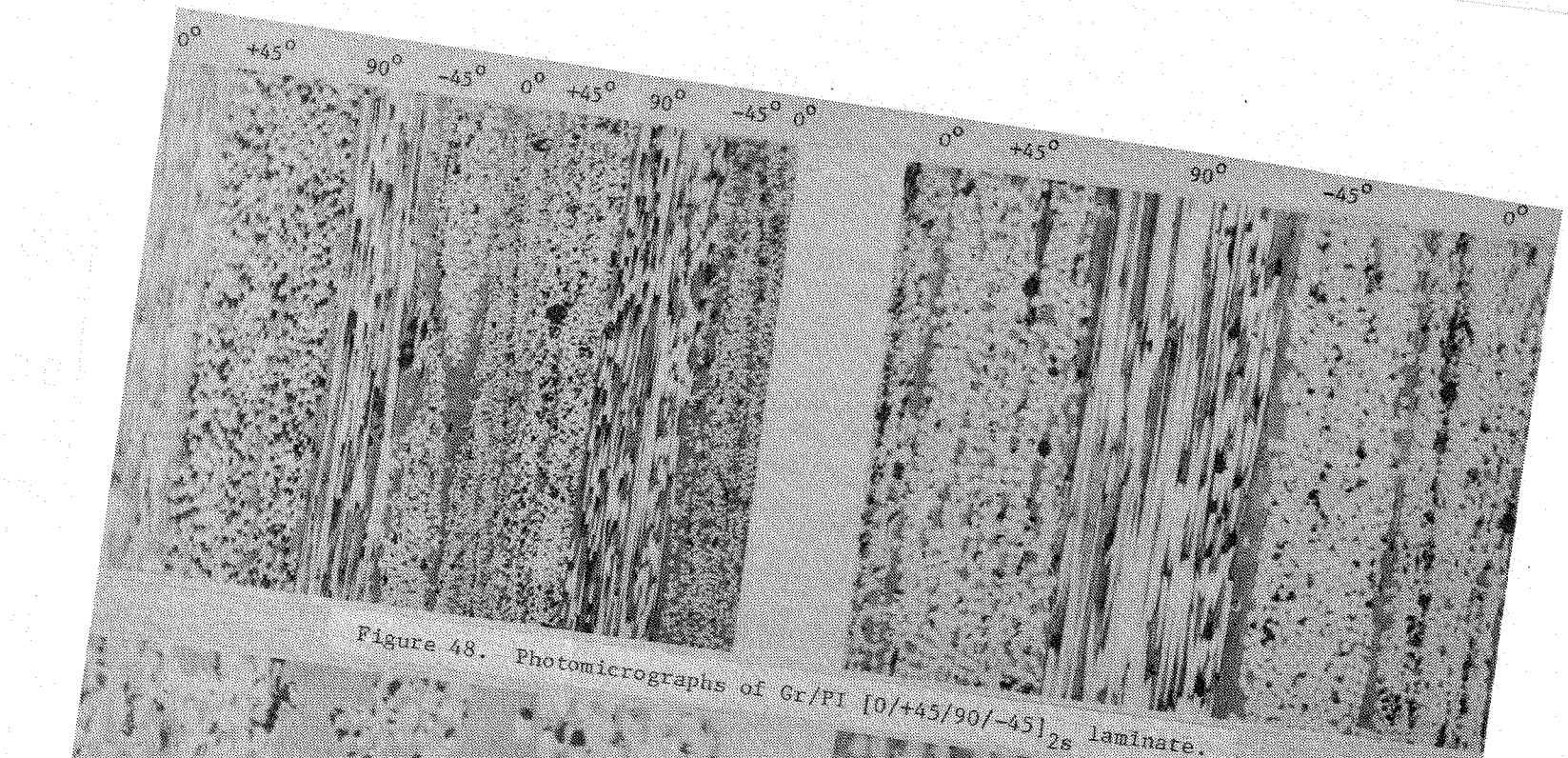

Figure 48. Photomicrographs of Gr/PI $[0/+45/90/-45]_{2s}$ laminate.

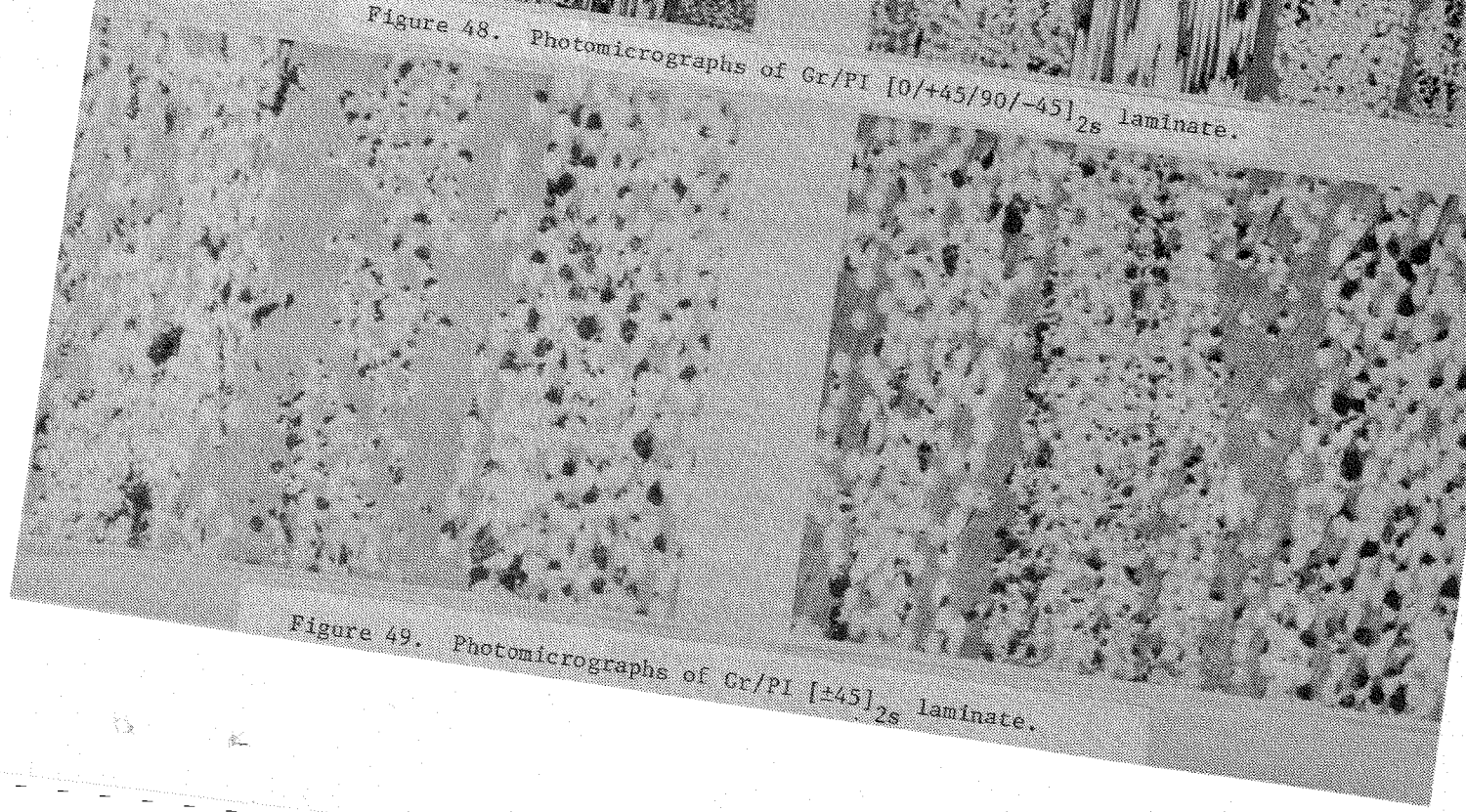

Figure 49. Photomicrographs of Gr/PI $[\pm 45]_{2s}$ laminate.

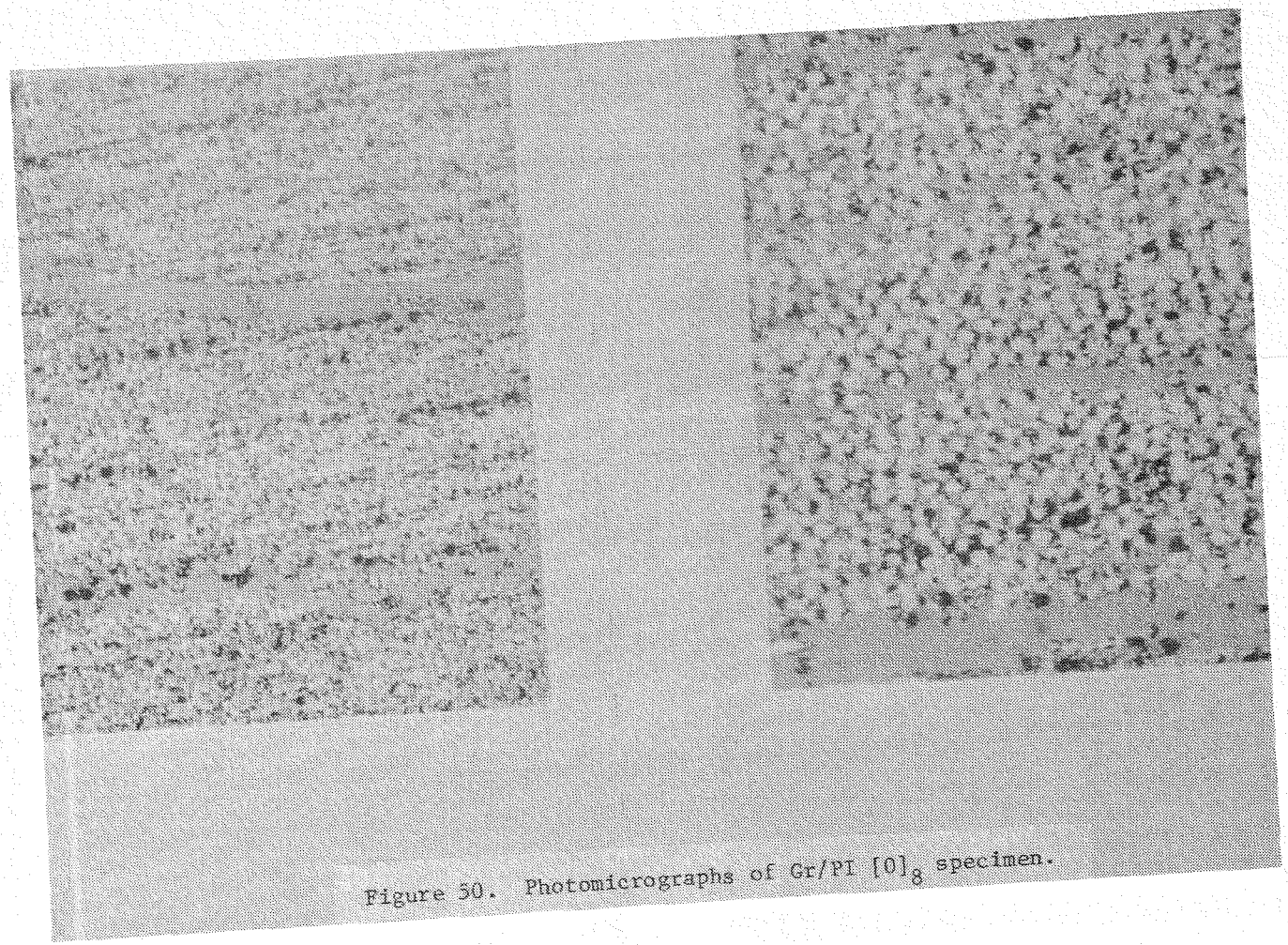

Figure 50. Photomicrographs of Gr/PI $[0]_8$ specimen.

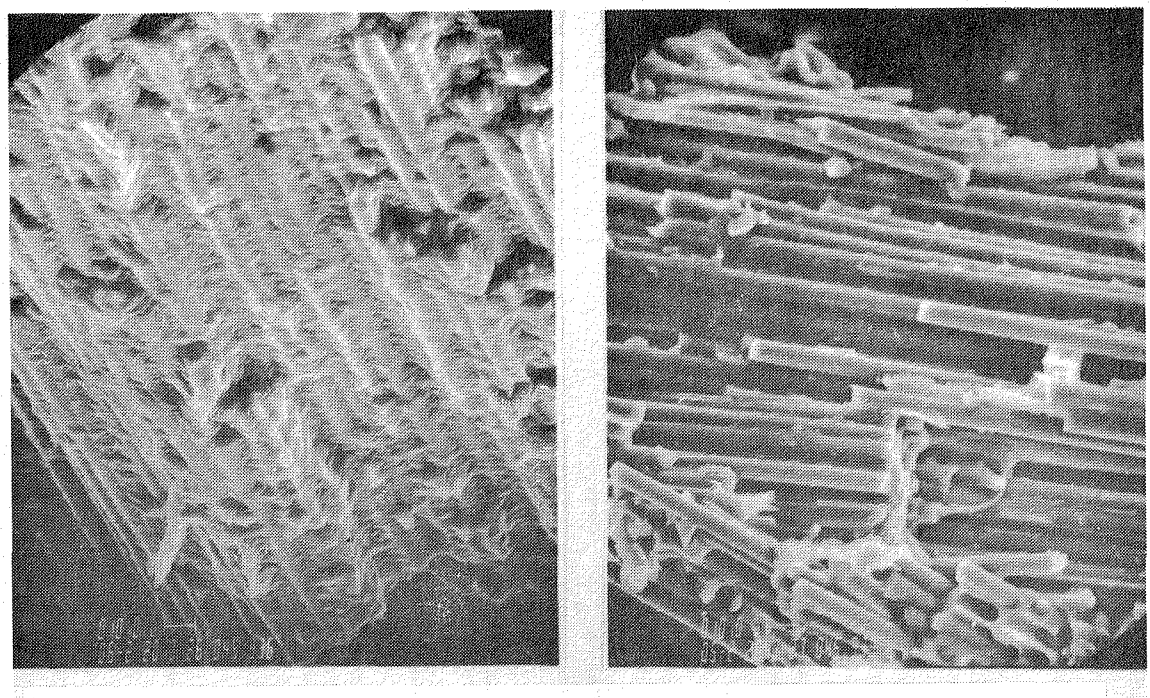

Figure 51. SEM photographs of Gr/PI $[0/+45/90/-45]_{2s}$ laminate.

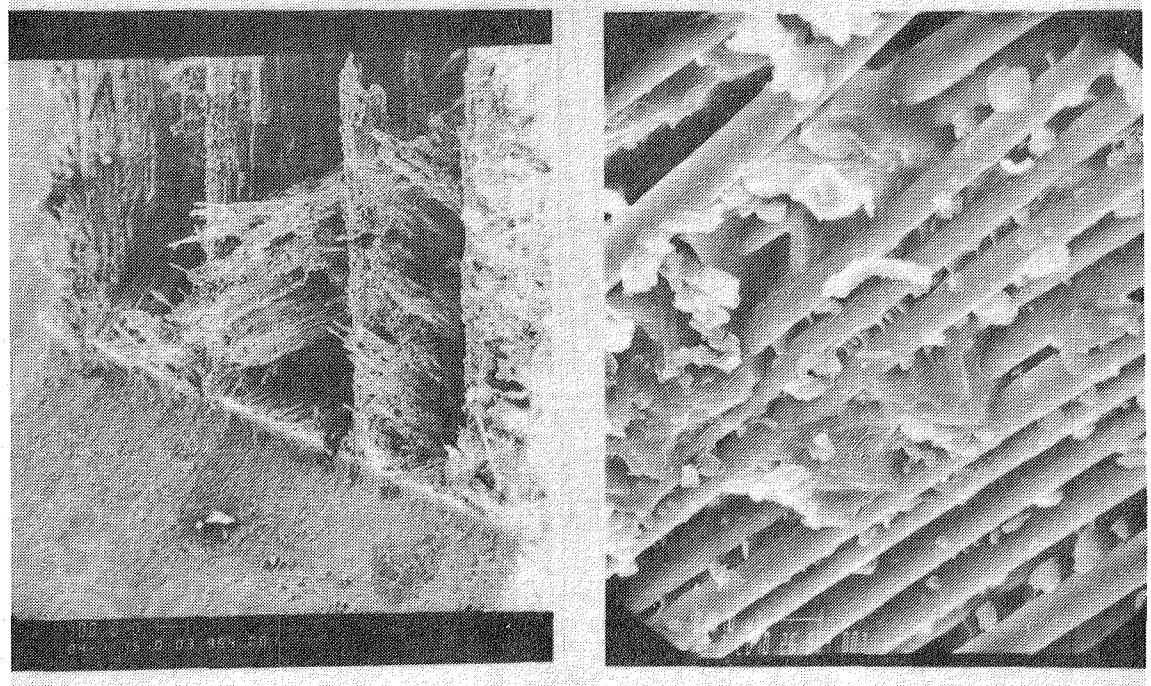

Figure 52. SEM photographs of notched Gr/PI $[0/+45/90/-45]_{2s}$ laminate (crack length = 20.47 mm).

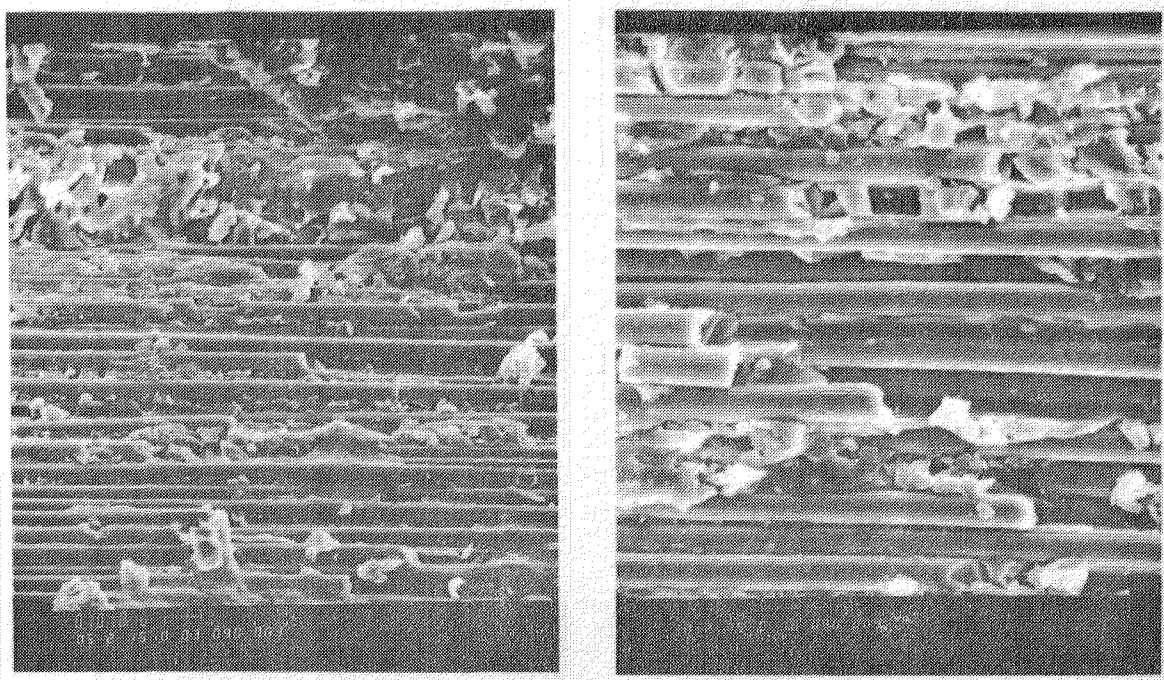

Figure 53. SEM photographs of edge notched Gr/PI $[90]_8$ specimen (crack length = 0.025 mm).

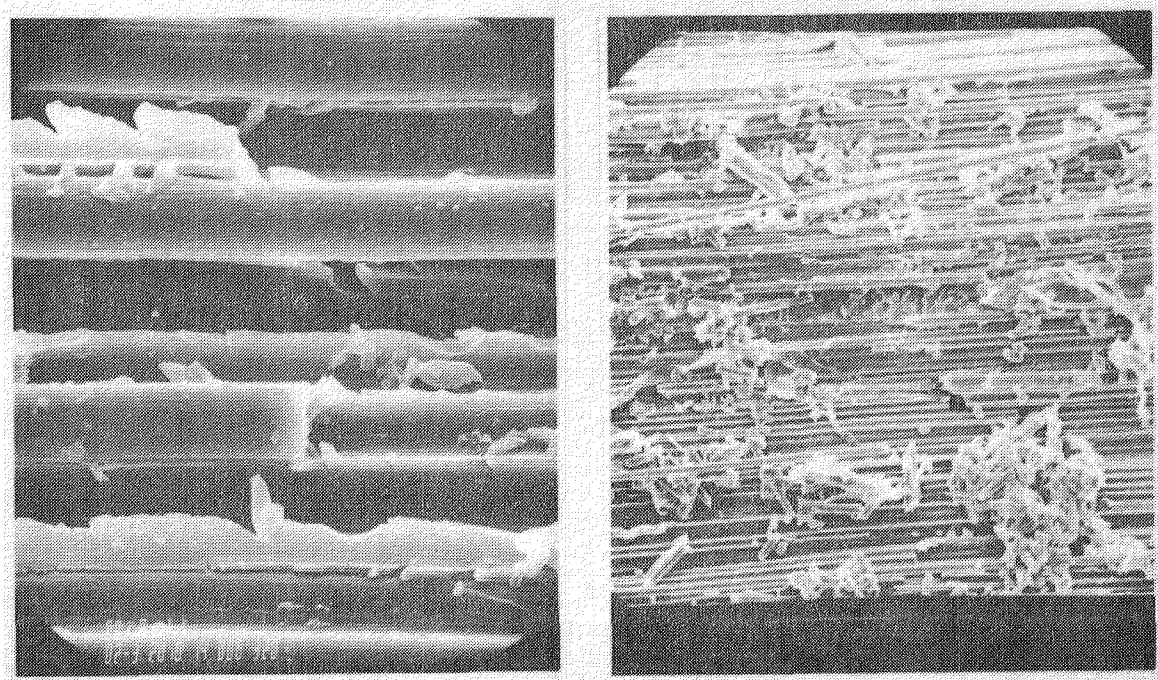

Figure 54. SEM photographs of the split area (at the crack tip) for notched Gr/PI $[0]_8$ specimen (crack length = 15.37 mm).

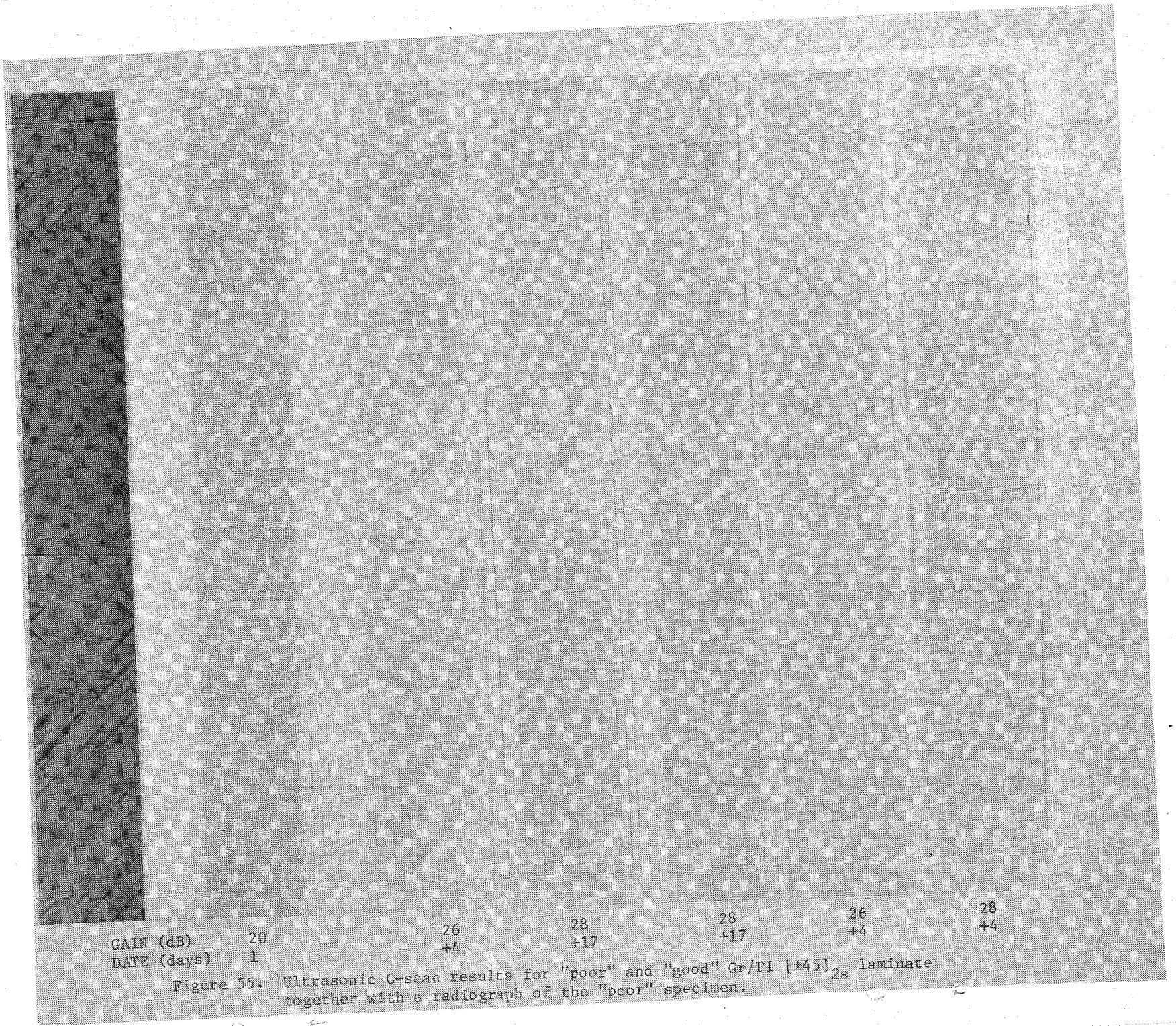

Figure 55. Ultrasonic C-scan results for "poor" and "good" Gr/PI $[\pm 45]_{2s}$ laminate together with a radiograph of the "poor" specimen.

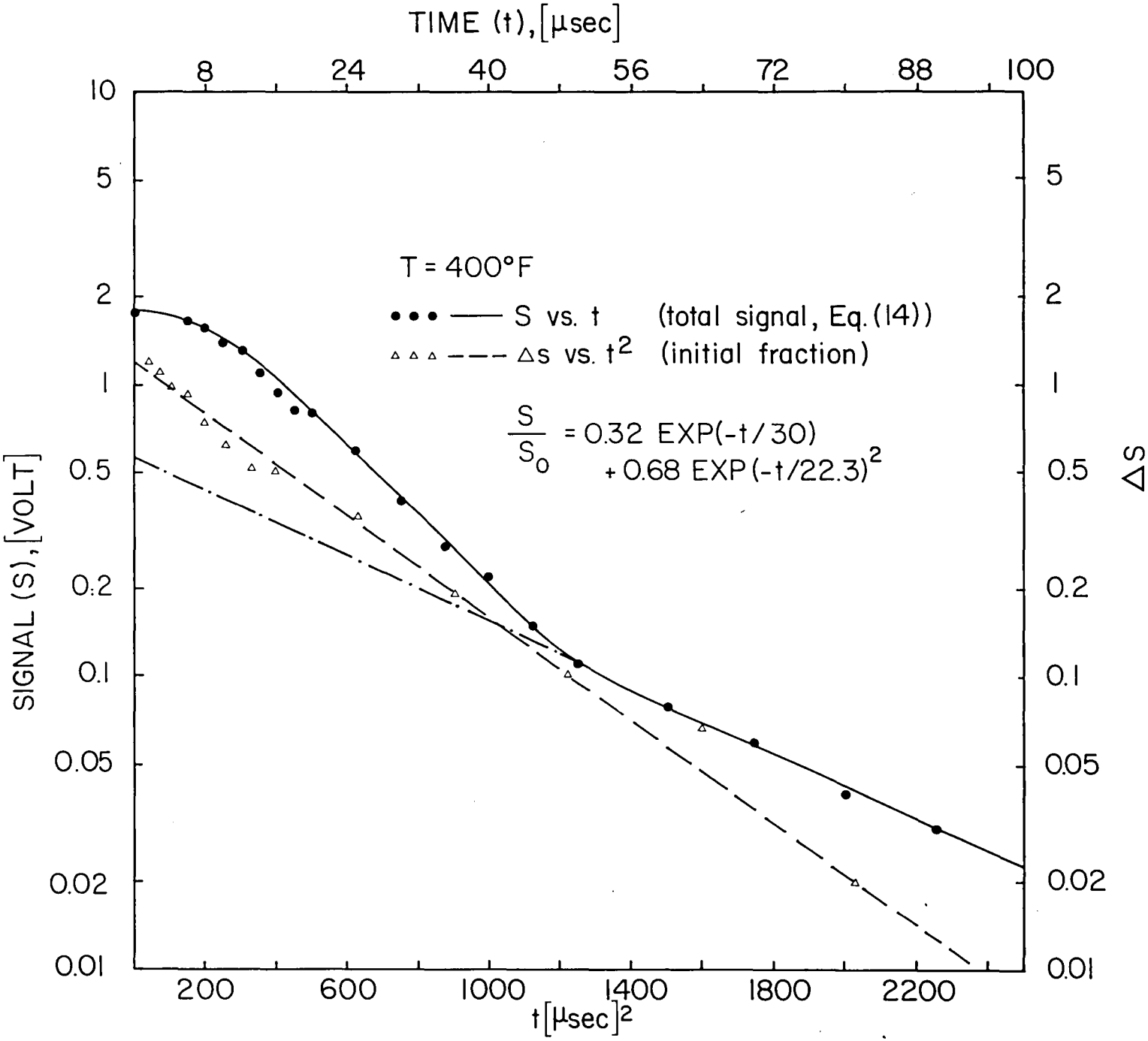

Figure 56. Signal relaxation spectrum following a 90° pulse.

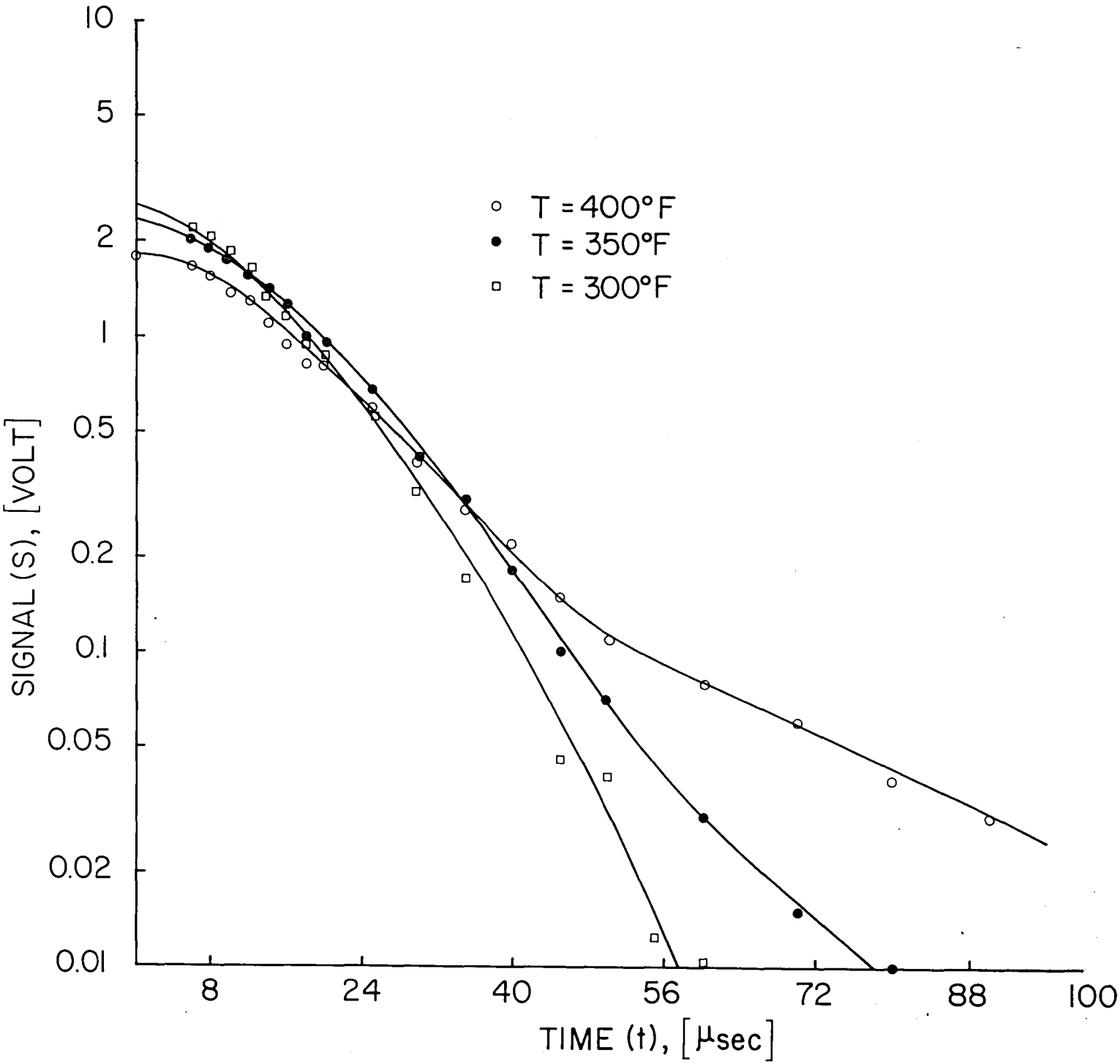

Figure 57. Signal relaxation spectrum following a 90° pulse for unfilled Polyimide at different temperatures.

End of Document